RADIATION RESPONSE IN MOS DEVICES WITH HIGH-K GATE OXIDES AND METAL GATES

By

Aritra Dasgupta

Dissertation

Submitted to the Faculty of the

Graduate School of Vanderbilt University

in partial fulfillment of the requirements

for the degree of

DOCTOR OF PHILOSOPHY

in

Electrical Engineering

August, 2011

Nashville, Tennessee

Approved:

Professor Daniel M. Fleetwood

Professor Robert A. Reed

Professor Robert A. Weller

Professor Marcus H. Mendenhall

Professor Sokrates T. Pantelides

ACKNOWLEDGEMENTS

First and foremost, my heartfelt thanks to Prof. Daniel M. Fleetwood, my advisor and the chair of my Ph.D. committee. He gave me the opportunity to work in his group and this thesis would have never seen the light of day without his mentoring and technical expertise. Apart from his able technical guidance, he has also taught me to be aware of my strengths and work hard on my weaknesses, the qualities essential to be an independent researcher.

I am also grateful to the other members of my committee Professors Robert Reed, Robert Weller, Marcus Mendenhall and Sokrates Pantelides for their time and useful scientific and career guidance. Professors Weller, Reed & Mendenhall gave me access to MRED without which this research would not have been possible. They also helped me with their technical support and guidance whenever I landed in problems from time to time. They were always there whenever I needed their technical or non-technical help and support. I would also like to thank Prof. Ron Schrimpf, Prof. Fleetwood, Prof. Weller, Prof. Reed and Prof. Pantelides for everything they taught me about semiconductor devices & electrical engineering through their courses and research. Their time and contribution helped me and my research in numerous ways, difficult to list in the limited space here.

I would like to especially thank the former and present RER group members who have been nice colleagues and friends during all these years. They have supported me and made my stay at Vanderbilt a pleasant experience. I would like to especially thank Mike King, Mike Clemens, Nathaniel Dodds, Elizabeth Auden & Brian Siewrawski for their help with the MRED simulations & issues from time to time. I would also like to thank Sarah Francis Ashley, Xing Zhou and others who have worked with me and helped me with the experiments in the lab and Enxia Zhang and Cher Zhang for technical discussions during all these years. I learnt a lot from all of them.

Tania, Sandeepan, Gaurav, Srikanth and a lot of my friends here at Vanderbilt & Nashville have made my life so far from home and family enjoyable and less lonely. They were the ones who cheered me up when things did not work out, a not-so-uncommon occasion in a graduate student's life.

I would also like to take this opportunity to express my thanks for the supportive administrative staff of the school of Electrical Engineering and Computer Science, the Graduate School, and also the Science and Engineering Library. Their generosity and always cheerful faces every time I asked for help was always very encouraging.

I also thank my funding agency for their support, practically none of this work would have been possible without them.

Finally, I thank my family and friends in India and here, for being with me through all my sunny and gloomy days. I am blessed with a supportive family, who were always there for me – even when separated by huge distances and time. Their love, belief in me and prayers always kept me on track and served as my greatest inspiration.

TABLE OF CONTENTS

Page

ACKNOWLEDGEMENTS ... ii

LIST OF FIGURES ... vi

1. INTRODUCTION ... 1

1.1 Motivation ... 1
1.2 Device Response in MOS Capacitors ... 4
1.3 Charge Particle Transport and Deposited Dose ... 7
1.4 Simulation programs for Transport ... 9
1.5 Dose Enhancement Problem ... 10
1.6 Interaction of Photons with Matter ... 15
1.7 Total Ionizing Dose ... 17
References ... 21

2. HIGH-K GATE OXIDES IN MODERN CMOS DEVICES ... 29

2.1 Hafnium Oxide (HfO_2) ... 30
2.2 Alternate gate dielectrics for modern CMOS technologies ... 32
2.3 Choice of Gate Electrode ... 34
2.4 Reliability & Charge trapping issues in high-κ MOS devices ... 36
References ... 39

3. SIMULATION CODES ... 41

3.1 Introduction ... 41
3.2 CEPXS/ONETRAN ... 41
3.3 ITS TIGERP Transport Codes ... 44
3.4 MRED Simulation tool ... 48
3.5 MRED Architecture ... 50
References ... 51

4. ENHANCEMENT IN DEPOSITED ENERGY/DOSE IN SiO_2 BASED MOS AND REDUCTION IN HIGH-K MOS DEVICES…..……………………………………..53

4.1 Introduction..53
4.2 MRED Simulation Details 54
4.3 SiO_2 MOS Capacitors: 10 keV X-rays..57
4.4 HfO_2 MOS Capacitors: 10 keV X-rays..64
4.5 Medium Energy X-rays..69
4.6 Summary 75
References 76

5. EFFECTS OF METAL GATES AND BEOL MATERIALS ON X-RAY DOSE IN HfO_2 GATE OXIDE…………..……………………………………………………....79

5.1 Introduction..79
5.2 Simulation Details...82
5.3 MRED Simulations 83
5.4 High-κ Metal Gate MOS Capacitors: 10 keV x-rays...84
5.5 Effect of Back-End-Of-Line Layers 89
5.6 High-κ Metal Gate MOS Capacitors: Medium energy x-rays...............................97
5.7 Effect of Gate Metal Layer Thickness 102
5.8 Summary 104
References 106

6. CONCLUSIONS..109

LIST OF FIGURES

Figure **Page**

1.1. Sensitive Regions for Total Dose Damage in MOS devices 3

1.2. ΔV_{ot} as a function of dose for 10-keV x-ray and Co-60 irradiations of TaSi/Al gate MOS capacitors...6

1.3. (a) Charge particle equilibrium and (b) the concept of equilibrium thickness ……..11

1.4. Relative deposited dose at silicon-gold interface: (top) neglecting dose enhancement and (bottom) taking dose enhancement effects into account 12

1.5. Dose profiles at silicon-gold interfaces with x-rays traveling from gold (high-Z side) to silicon (low-Z) side 13

1.6. Probability of the photoelectric effect, Compton scattering and pair production occurring for different Z of the target material and the incoming photon energy 16

1.7. Schematic energy band diagram for a MOS structure, indicating major physical processes underlying radiation response..18

2.1. Energy diagrams of threshold voltages for nMOS and pMOS devices using (a) TiN (midgap) metal gates and (b) Pt (dual) metal gates 35

2.2. (a) I_d –V_g characteristic of 4.5 nm HfO_2 NFET 36
(b) C–V_g characteristic of 4.5 nm HfO_2 NFET...36

3.1. Dose and kerma profiles calculated by the CEPXS/ONETRAN simulator for the LiF/Pb case. The fluence is one photon/cm^2...44

3.2. Pulse height spectrum with a germanium detector. Results show an improvement and better match with experiments for the improved ITS version 3.0 codes over the previous ITS version 2.1 47

4.1. Device geometries for Al-gate, $TaSi_2$-down, and $TaSi_2$-up MOS capacitors (after [1]). Secondary electrons emitted from the $TaSi_2$-up layer are attenuated more by the thicker Al layer than are the electrons emitted from the $TaSi_2$-down layer, which is 470 nm closer to the gate oxide. For the HfO_2 calculations performed, the SiO_2 layer (dark grey) was simply replaced by HfO_2 55

4.2. Simulated 10-keV x-ray energy deposition profile for 98 nm SiO_2 Al-gate, $TaSi_2$-down, and $TaSi_2$-up MOS capacitors. The energy deposition profile is shown for

comparison for a pure SiO_2 layer of the same physical thickness as the multilayer capacitor structures of Figure 23..........57

4.3. Enhanced dose due to 10-keV x-rays for the MOS capacitor structures of Figure 23 as a function of SiO_2 dielectric layer thickness..........58

4.4. Comparison of MRED calculations with TIGERP, TEP, CEPXS/ONETRAN simulators (results from [3]) for the Al-gate SiO_2 MOS capacitors of Fig. 23. The DEFs were computed for 10-keV x-rays..........59

4.5. Comparison of MRED calculations with TIGERP, TEP, CEPXS/ONETRAN simulators (results from [3]) for the TaSi-Up gate SiO_2 MOS capacitors of Figure 23. The DEFs were computed for 10-keV x-rays..........60

4.6. Comparison of MRED calculations with TIGERP, TEP, CEPXS/ONETRAN simulators (results from [3]) for the TaSi-Down gate SiO_2 MOS capacitors of Figure 23. The DEFs were computed for 10-keV x-rays..........61

4.7. MRED calculations of the ratios of the DEFs due to 10-keV x-rays for capacitors with 35 nm oxides to the DEFs of capacitors with 1060 nm oxides. These are compared with the experimentally measured ratios of hole trapping reported in [3] for capacitors with oxides of these two thicknesses..........64

4.8. Deposited energy due to 10-keV x-rays in the gate dielectric for MOS capacitors with HfO_2 and SiO_2 gate insulators as a function of physical gate oxide thickness, for the Al gate structures..........65

4.9. Dose (in krad(HfO_2) and krad(SiO_2)) due to 10-keV x-rays in the gate oxides of MOS capacitors with HfO_2 and SiO_2 gate insulators as a function of physical gate oxide thickness, for the Al gate structures of Figures 23..........66

4.10. Excess dose deposited in HfO_2 MOS capacitor structures compared to the equilibrium deposited dose in a pure SiO_2 structure due to 10-keV x-rays. The dose reduction in the gate dielectric observed for thin HfO_2 layers is significantly greater when the dielectric is surrounded by lower-Z materials than when surrounded by higher-Z materials..........67

4.11. Ratios of (μ_{en}/ρ) values for HfO_2 (Z_{eff} ~ 67) and SiO_2 (Z_{eff} ~11) as a function of photon energy. For 10-keV x-rays, the ratio is ~ 4..........69

4.12. 400-keV endpoint-energy bremsstrahlung x-ray spectrum (average energy 105 keV) from the Sandia Pelletron, as simulated by MRED..........71

4.13. Deposited energy in the gate dielectric for HfO_2 and SiO_2 Al-gate MOS capacitors as a function of gate oxide physical thickness for the 400-keV endpoint-energy bremsstrahlung x-ray spectrum..........72

4.14. Dose (in rad(SiO_2) and rad(HfO_2)) as a function of physical oxide thickness for HfO_2 and SiO_2 gate dielectric layers for the MOS capacitor structures of Figure 4.1, for the 400-keV endpoint-energy bremsstrahlung x-ray spectrum..73

5.1. Mobility as a function of effective electric field E_{eff} for a HfO_2 based MOS device with a Poly-silicon gate...80

5.2. Mobility as a function of effective electric field E_{eff} for a HfO_2 based MOS device with a TiN metal gate...81

5.3. Simulated device geometries for high-κ metal gate MOS capacitors.........................83

5.4. Deposited energy by 10 keV x-rays in the gate dielectric for HfO_2/ Metal gate MOS devices and SiO_2 /Polysilicon-gate MOS capacitors as a function of gate oxide physical thickness..85

5.5. Deposited dose (in krad(HfO_2) and krad(SiO_2)) in the gate dielectric for MOS capacitors with HfO_2 with metal gates and SiO_2 gate insulators with Polysilicon gates as a function of physical gate oxide thickness, for the gate structures.. 86

5.6. Excess 10 keV x-ray dose deposited in HfO_2/metal gate MOS capacitor structures compared to the "equilibrium" deposited dose in a pure SiO_2 structure. 87

5.7. Device geometry with a single layer of back-end-of-line (BEOL) materials..............90

5.8. Excess 10-keV x-ray dose deposited in HfO_2/metal gate MOS capacitor structures compared to the equilibrium deposited dose in a pure SiO_2 for the BEOL layers 91

5.9. Deposited dose versus HfO_2 oxide thickness for TiN, TaN and Polysilicon gated high-k MOS capacitor structure with 1 layer of Cu metallization and other BEOL layers…..92

5.10. Device geometries with more realistic gate stack: (a) High-k/ Metal gated device with 4 layers of Cu interconnects (300 nm) and W vias (0.5 μm cube) and passivation layers. (b) High-k/ Metal gated device with 6 layers of Cu interconnects (300 nm), W vias. SiO_2 and Si_3N_4 passivation layers have been added to the multilevel Cu interconnect structures…………………………………………………………………………93

5.11. Excess 10-keV x-ray dose deposited in HfO_2/TiN gate MOS capacitor structures compared to the equilibrium deposited dose in a pure SiO_2 structure ………………………………………………...94

5.12. Deposited dose versus HfO_2 oxide thickness for TiN gated high-k MOS capacitor structure with 1, 4 and 6 layers of Cu metallization and other BEOL layers.. ....…95

5.13. Excess 10 keV x-ray dose deposited in HfO_2/TiN gate MOS capacitor structures compared to the “equilibrium” deposited dose in a pure SiO_2 structure for structures with 1,4 and 6 layers of Cu metallization and other BEOL layers 96

5.14. Deposited dose versus HfO_2 oxide thickness for TaN gated high-k MOS capacitor structure with 1, 4 and 6 layers of Cu metallization and other BEOL layers 97

5.15. Deposited energy in the gate dielectric for HfO_2 MOS capacitors with TiN, TaN and poly-silicon gates as a function of gate oxide physical thickness for the medium-energy x-ray spectrum...98

5.16. Dose (in rad(HfO_2)) as a function of physical oxide thickness for HfO_2 gate dielectric layers for the MOS capacitor structures with TiN, TaN mid-gap metal gates and poly-silicon gates.. 99

5.17. Excess dose deposited due to medium energy x-rays in HfO_2/TiN gate MOS capacitor structures, compared to the equilibrium deposited dose in a pure SiO_2 structure.. ……………………………………………………………………………………..100

5.18. Excess dose deposited due to medium energy x-rays in HfO_2/TaN gate MOS capacitor structures compared to the equilibrium deposited dose in a pure SiO_2 structure ……………………………………………………………………………………... 101

5.19. Excess dose deposited due to medium energy x-rays in HfO_2/poly-silicon gate MOS capacitor structures compared to the equilibrium deposited dose in a pure SiO_2 structur…………………………………... …………………………………………102

5.20. Dose enhancement factor for 10 keV x-rays in the high-k HfO_2 gate oxide for different gate metals like TiN, TaN and Poly-silicon as a function of gate metal thickness.……………………………………………………………………………… 103

CHAPTER I

INTRODUCTION

1.1 MOTIVATION

In semiconductor devices, high atomic number materials occur in the gate metallization [1]. They can also occur in the device packaging. In the case of MOSFET, the performance of the FET is affected by the deposited dose in the gate dielectric region of the chip. Due to the chip thickness being large, the chip is not affected by total dose effects at the back side of the chip. There are two primary regions of a chip where high atomic number materials can be present which may cause significant enhancement in deposited energy and dose: the metallization of the gate and the device package lid.

Among the various forms of chip metallization, the three of significance are:

a) Gate metallization

b) Schottky metallization

c) Au metallization

Materials like - Al_2O_3, BeO etc. are used as material in device metal lids. Also materials like Cr, Ni plates, Fe-Ni alloys are used in lid metallization. Au is also used as lids.

In Au – lidded devices, enhancement is uniform over the entire area of the chip. In contrast, in Al_2O_3 and BeO based packages, more enhancements are found to occur adjacent to the high atomic number metal present.

The ever shrinking geometries of CMOS technology and the very high transistor density of modern ICs have resulted in the number of metal layers used as well as the thickness of these interconnect metal layers to increase in modern technologies. The presence of these layers is important to be studied. It is also important to characterize the effects of replacing Al with Cu as the interconnect material.

Dose Enhancement Factor (DEF) is an important metric that is used to characterize the effects of dose enhancement in electron devices. We obtain the average dose being received by the sensitive volume by multiplying the dose deposited in the same material under equilibrium conditions with the enhancement factor. The Dose Enhancement Factor (DEF) is thus defined as the ratio of the net dose in the sensitive volume of interest of the device to the dose in equilibrium.

Total ionizing dose (TID) damage and photo-current generation are the two main ways by which MOS devices are affected by dose enhancement. The most vulnerable or sensitive region is the gate insulator layer (SiO_2/ HfO_2) located near the active region of the device as far as TID damage is concerned. In case of the transient effects, the photo-current collection occurs over a sensitive volume and is the most critical part of the

device. The regions sensitive to total dose damage affecting device response are shown below in Figure 1.1 [1].

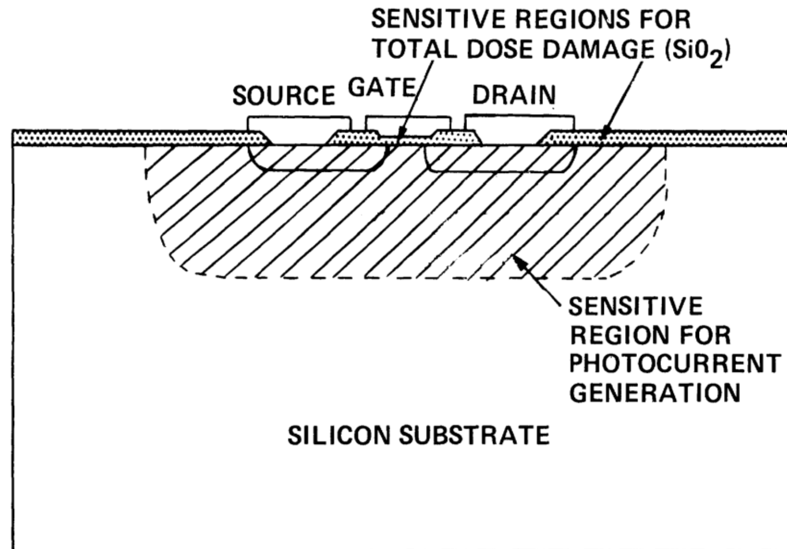

Figure 1.1: Sensitive regions for total dose damage in MOS devices [1].

The primary effect of TID in MOS devices is to cause a shift in threshold voltage (V_T) and increased leakage due to radiation induced-charge buildup (both oxide trapped charge and interface traps) in the gate oxides and the overlying field oxide regions. Higher leakage currents are observed due to the silicon underlying the field oxide getting inverted and also due to the higher recombinational velocity at depleted surfaces with p-doped Si. The total number of electron-hole pairs generated is a function of the total deposited dose in the oxide. The interface traps are caused by a charge transport mechanism of holes in the dielectric and hence is also a strong function to TID.

In the case of BJTs, the total dose affects the current gain, h_{FE}, the emitter base leakage current, I_{BE} and the collector base leakage current, I_{CB}. This can be attributed to interface traps which increase the recombination velocity. The average dose in the oxide affects the charge build-up in these devices. The dose enhancement factor can be calculated by a weighting method based on the details of transistor used.

Gate oxide scaling has made CMOS very hardened with respect to TID induced degradation of device. In modern CMOS technologies, the edge-related issues are very important [3] to be considered. Shallow-Trench Isolation (STI) is used in modern CMOS geometries in order to accomplish device isolation in order to increase both the packing density and speed. The active area pitch is also improved [3]. Oxide charge trapping in the STI results in the parasitic lateral transistors to turn on. Hence it can cause leakage problems. The small-width MOSFETs are affected by this. The STI is thus quite vulnerable due to TID damage.

1.2 DEVICE RESPONSE IN MOS CAPACITORS:

Fleetwood et al. [4] studied the device effects of MOS capacitors to 10 keV and medium-energy bremsstrahlung x-rays for different gate metallization, gate dielectric thickness, and electric field on the device. The detailed schematic diagrams and structures of these MOS capacitor devices are discussed in the next chapter in this work. The SiO_2 thickness was varied from 35 nm to 1.06 μm which is typical of field oxides. The devices were

fabricated using a steam environment. The 35 and 98 nm oxides were grown at 850 °C, and the 356 and 1060 nm oxides at 1100 °C respectively. All oxides were subjected to an annealing in N_2 at 1100 °C. The gate metal layers were deposited using a radio-frequency (RF) source. In the case of the TaSi-Down structures, 0.2-μm of Aluminum is evaporated on the SiO_2. This protects sputtering-induced damage. The tantalum silicide layer was formed at room temperature using a DC-sputtering machine. The tantalum silicide layer has a density of 8 g/cm^3. Photolithography was used for patterning.

Relative enhanced response has been defined as a metric to measure the device behavior to low energy x-rays and a comparison was made to the radiation using Co-60 gamma rays. The quantity ΔV_{ot} was measured and reported because it depends on dose directly. Also, it is significant to device electrical degradation. It was also observed that interface-trap production was very low in these MOS devices.

Figure 1.2 below shows ΔV_{ot} versus dose for 10-keV x-ray and Co-60 gamma rays of TaSi-Down MOS capacitors. The gate oxide thickness is 98 nm, and the electric field is 1 MV/cm.

Fleetwood et al. [5] further studied dose enhancement effects in CMOS transistors using a sub threshold current-voltage technique to separate the contributions of oxide trapped charge and interface trap build-up to the net threshold voltage shifts in these transistors. Their results of annealing of holes trapped in the oxide and recombination of electrons

and holes, were used to study and hence compare the effects on transistors that were irradiated with low energy x-rays and gamma rays.

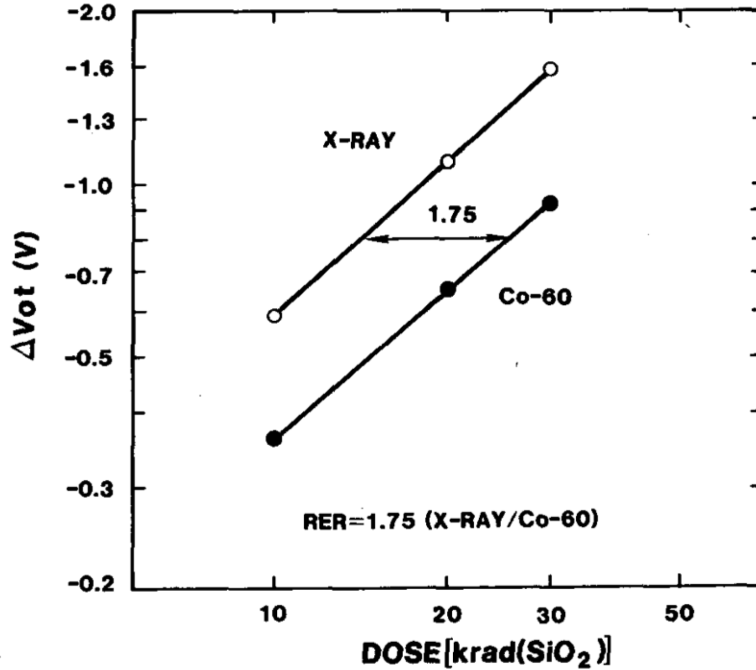

Figure 1.2: ΔV_{ot} as a function of dose for 10-keV x-ray and Co-60 irradiations of TaSi-Down and Al gate MOS capacitors [4].

It was observed that in the x-ray irradiation case [4],[6], lower total dose in (rad SiO_2) results in the same value of ΔV_{ot} than with Co-60 gamma rays. The researchers reported a value for relative enhanced response to be approximately ~ 1.75. Further experimental and simulation results on these devices will be discussed both qualitatively and quantitatively in a later chapter.

1.3 CHARGE PARTICLE TRANSPORT AND DEPOSITED DOSE

An excellent review of various aspects of radiation dosimetry including dosimetry at various facilities can be found in [7]. We know that the concept of charge transport in materials is an important concept for understanding energy and dose deposition in complex materials. In order to understand dosimeters and to design simulators for simulating radiation effects, an understanding of the physics of electron and photon transport is required. A lot of researchers have developed models based on theory and cross-checked their results with actual experiments. This knowledge can be applied to electron devices and other applications.

1.3.1 Transport of Photons and Electrons in Solids

It is critical to study the physical interactions, the slowing down of electrons as they travel through matter by using transport related simulations and experiments [7]. The transport of charged particles like electrons and photons may be treated as different problems. However, with increase in energy of incident radiation, electrons are produced by photons and photons are in turn produced by electrons more frequently. As a result, the problem becomes that of transport of *coupled* photons and electrons which must now be taken into consideration.

1.3.2 Interactions of electrons with materials

Photons and electrons traveling through materials are absorbed. Some of them are scattered along different directions. Energy is lost as a result of all these processes. The probability of scattering is a function of the cross section for a particular process in the given material. Elastic and inelastic scattering by electrons may occur. The parameters for these various interactions have been theoretically computed. They can then serve as input to discrete ordinates and Monte Carlo codes. Studies have been done to calculate mean free path of electrons [8]–[13], their range [14], and other process probabilities [15]. Straggling [16]–[18] and scattering [19] of electrons have also been studied by researchers working in this field.

A review has been done [20] on the experimental and theoretical advances about the physics of electrons as they slow down while traveling through materials. Electrons were bombarded into materials of interest and the energy distribution of electrons emitted by the materials was measured. These experiments demonstrated that the energy spectrum of the electrons as they travel through these materials is crucial. Integrating the relevant cross sections and multiplying them with the flux of electrons gives us useful information about each of these events [21], [22].

1.4 SIMULATION PROGRAMS FOR TRANSPORT

Transport was studied using a finite-difference solution of the Spencer–Lewis transport equation [21],[22]. A discrete ordinates solution of this equation in two dimensions was also proposed [23]. The Boltzmann transport equation was solved at very low electron energies using eigen-values [24], [25]. Researchers developed an analytic model to the transport equation [26]–[28]. A polynomial expansion method was also used [29], [30] to compute x-ray photon emission angular distribution functions [31]. A lot of studies have focused on developing computer codes for calculating phenomena such as deposition of charge, bremsstrahlung spectrum, etc. Monte Carlo codes such as TIGER [33], [34], and the Integrated Tiger Series (ITS) [35] and discrete ordinate codes CEPXS/ONETRAN [36], [37] and CEPXS/ONELD [38] were built for simulation purposes by several research groups [39], [40]. We will discuss some of these simulators in greater details in Chapter III.

It is very important to validate simulations with experiments and hence make comparisons between computed values and experimental results. The Monte Carlo based simulator SANDYL [41] was used to calculate the energy deposition spectra due to gamma-rays in silicon [42]. Monte-Carlo codes have also been used to validate the bremsstrahlung spectrum generated from various sources [43]–[50]. Dose enhancement effects are different for different gamma sources and the differences in dose profiles can be understood by comparing the experimental results with the code generated numbers

that can be computed for these various sources. Similar work has been reported [51], [52].

The spectrum of photons using test cells is evaluated using discrete ordinate CEPXS/ONELD transport simulations [53]–[55]. It was used to compute photon transport through different materials of interest [56], [57]. Electron beams of different energies cause different dose profiles. This has been studied in details by researchers [58]–[61].

Experiments [62]–[64] were also designed in order to cross-check dose profiles calculated by the ITS codes. Measurements were made to study transmission of electron beams [65], [66] and the response of germanium dosimeters to incident x-rays [67] were reported.

1.5 DOSE ENHANCEMENT PROBLEM

An important concept in dose enhancement problem is the concept of *charged-particle equilibrium*. Charged particle equilibrium (CPE) occurs when the energy carried by electrons out of a given sensitive volume are replenished by an equal number of electrons [68] of equivalent energy entering into the same sensitive volume. This is shown in Figure 1.3(a) below. The elemental volume located near the frontal region of the slab has

more electrons scattered out of it than are scattered into the volume. As a result, there is a net loss of energy carried by electrons and CPE is not maintained under this condition.

However for sensitive volumes located deeper down into the material slab, at a certain distance, charge particle equilibrium is achieved. The minimum thickness of material when charge particle equilibrium is attained is called the "equilibrium thickness". This is shown in Figure 1.3(b) below.

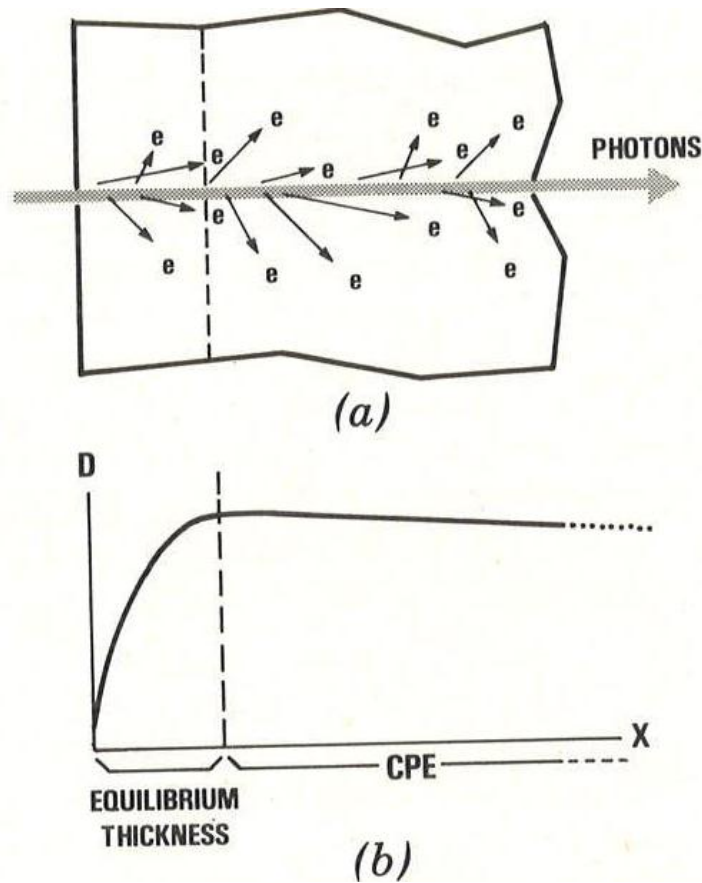

Figure 1.3: (a) Charge particle equilibrium and (b) the concept of equilibrium thickness [68].

The equilibrium thickness depends on the nature of the material. Further, it depends on the energy spectrum of the incident radiation. When equilibrium thickness is reached, the dose can be calculated as the product of the photon flux times the photon mass-energy absorption coefficient. Charged particle equilibrium does not hold at the interface of high atomic number and low atomic number material. The theoretical dose values in Au and Si are shown by solid lines in Figure 1.4 (top). The actual dose in Si and Au near the Au and Si interface after taking into account dose enhancement is shown and the below in Figure 1.4 (bottom).

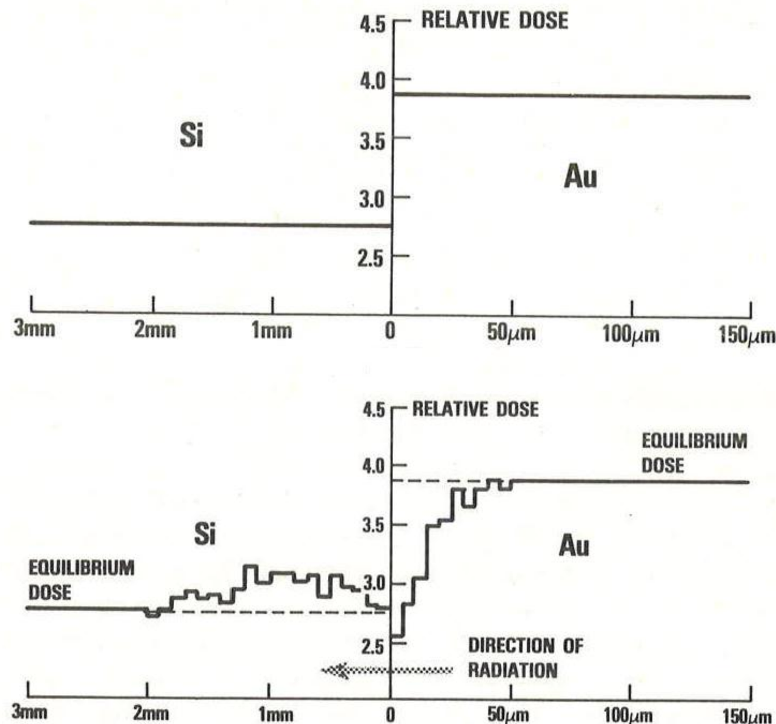

Figure 1.4: Relative deposited dose at silicon-gold interface: (top) neglecting dose enhancement and (bottom) taking dose enhancement effects into account [68].

1.5.1 Review of literature:

Researchers have reported [69] that a thick block of a high-atomic number material is placed near a thick block of a low-atomic number material when subjected to Co-60 irradiation, the dose deposited at the interface is twice the equilibrium dose. The actual dose deposition profile near the high atomic number material and low atomic number material interface is a strong function of the direction of the incident gamma rays. This dose deposition for gamma rays approaching from high-Z side is shown in Figure 1.5 below.

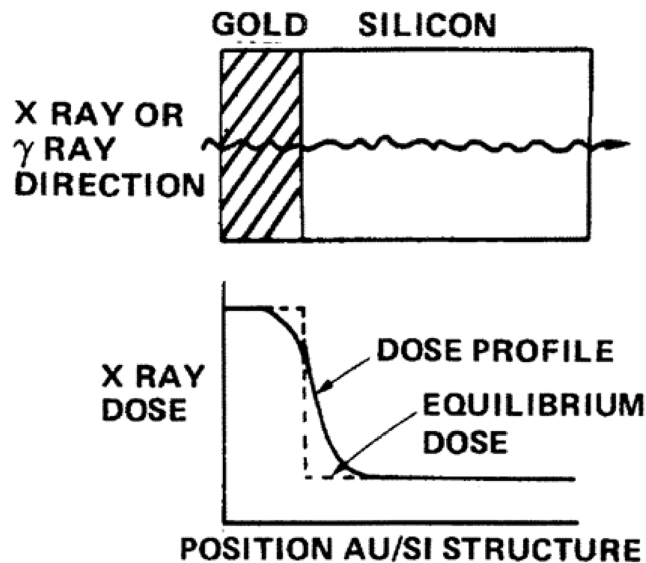

Figure 1.5. Dose profiles at silicon-gold interfaces with x-rays traveling from gold (high-Z side) to silicon (low-Z) side [1].

Experiments were conducted by other groups [70],[71] with chambers for secondary electron production. They also found nearly twice dose enhancement. Researchers also studied charge deposition at the interface of high-Z and low-Z materials [71]. Measurements show the current due to electron flow to diverge. This can be interpreted , using the continuity equation as a divergence of cumulative energy or charge deposition in the regions near high-Z and low-Z interface. Some research groups [72] demonstrated the interesting observation that adding a low atomic number material in the beam line leads to an even higher enhancement with gamma-rays due to increase in low energy photons.

1.5.2 Modeling and Simulation

Monte Carlo simulators [73] like the POEM [74] codes were performed for silicon and gold interface. The dose profiles in the low atomic number materials were computed for a wide energy range - low to very high (0.01 - 2 MeV) for direction of gamma rays coming from both high-Z and low-Z sides. Good analytic representations of the dose were obtained by fitting the curves to the actual current profiles. Another model [75] was developed using exponential functions for the dose deposition profiles. The functional constants were calculated in terms of the absorption coefficients, the range and backscatter coefficients for the electrons. Good agreement was observed with the fit coefficients [76]. The exponential nature of the model [77], however, could not generate the actual shape of the dose profiles farther away from the high-Z/low-Z interface [78]. The model was extended [79] to the case at higher energies using exponential solutions.

Another 1-D model was proposed [80], [81] which have been used to calculate enhancement, in irregular geometries composed of many layers of materials.

1.6 INTERACTION OF PHOTONS WITH MATTER

Ionizing radiation creates electron-hole pairs in semiconductor materials. The performance of MOSFETs gets affected due to charge build-up as a result of electron hole pairs generated in the gate and field oxides. We discuss the physical phenomena that lead to charge generation in the gate dielectrics. The atomic number, density of the target material, incident energy, and the mass of the projectile play a crucial role in determining the charge yield [83].

For dose enhancement studies, we focus on interactions of photons with matter. Photons interact with matter in three different ways depending on the initial photon energies; these include the photoelectric effect, the Compton effect, and pair production [84]. During photoelectric effect, the incident photon is absorbed and loses its energy by knocking off the electron from the inner shell of the atom. This ejected photoelectron has energy equal to the energy of the incoming photon minus the binding energy of the electron to the atom. The photoelectron travels through the material of interest (gate oxide in our case) to create more electron and hole pairs. For medium and high energy photons, Compton scattering occurs where both the photon and the atom get scattered and more electrons and holes are created by the scattered photon. Pair production occurs at

very high energies (~1.02 MeV). The incoming photon creates an electron and a positron pair and the annihilation of photon occurs. Figure 1.6 shows the probability of each of these three processes to occur as a function of the photon energy and the atomic number of the target atom [85].

Electrons hole pairs created by ionizing radiation in the gate and field oxides are lost due to recombination or are trapped in defect sites present in the oxides. The number of electron hole pairs that escape recombination is a function of the applied electric field [84]-[86]. Charge trapping in the oxide affects the electrical performance of the device. This trapping is a strong function of the conditions [87] that the device goes through during CMOS process flow.

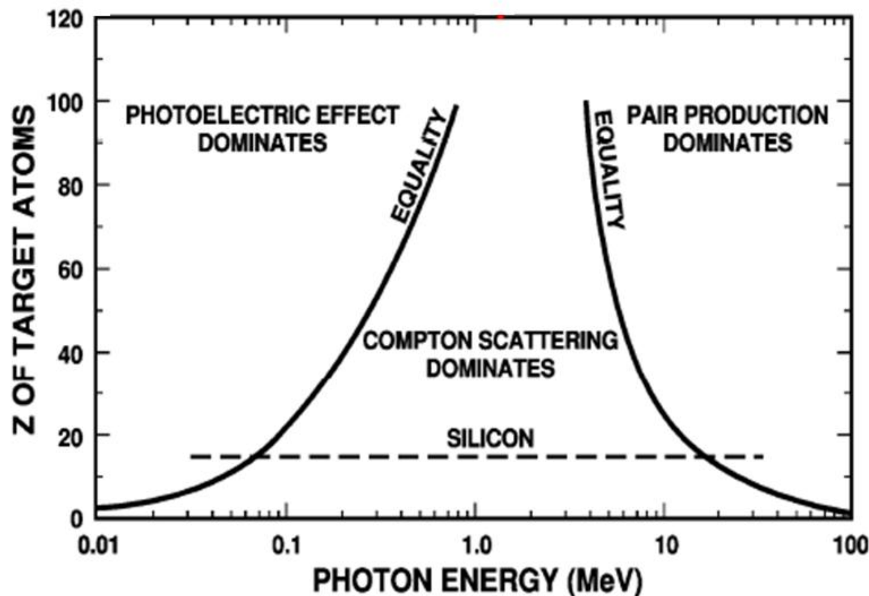

Figure 1.6. Probability of the photoelectric effect, Compton scattering and pair production occurring for different Z of the target material and the incoming photon energy [83].

Single event effects (SEE) is another radiation effect and reliability concern for CMOS technologies. Current transients are generated along the path of incoming ion. They are classified as soft errors and hard errors. Single event upsets (SEU) occur when bit flip occurs in the circuit [88]. Hard errors cause permanent damage due to significant amount of energy deposited in a small volume of the gate oxide. This is known as single event gate rupture (SEGR). High currents arising from massive projectiles and heavy ions may also lead to single event latch-ups (SEL). These effects, while important, will not be discussed further in this thesis.

1.7 TOTAL IONIZING DOSE

MOS transistors are at the heart of circuits used in spacecraft that are exposed to high ionizing radiation environments in space. Radiation affects the current-voltage characteristics of the MOS transistors. Figure 1.7 [89],[90] shows a schematic energy band diagram of a MOS structure, where positive bias is applied to the gate, so that electrons accumulate at the silicon/silicon dioxide interface under the gate, forming an inversion layer, and the region of the substrate near the interface is depleted of holes. There are four major physical processes that contribute to the total-ionizing-dose radiation response of a MOS device [90]:

(1) Electron/hole pairs generated by ionizing radiation.

(2) Hopping transport of holes through localized states in the SiO_2 bulk.

(3) Deep hole trapping near the Si/SiO_2 interface.

(4) Formation of radiation-induced interface traps within the Si band gap.

The most sensitive parts of a system to the long-term effects of ionizing radiation are the oxide insulators. When radiation (e.g., 10 keV x-rays from an ARACOR source) passes through a gate oxide, electron/hole pairs are created by the deposited energy. In SiO_2, the electrons are much more mobile than the holes, and swept out of the oxide typically in picoseconds for large positive biases at room temperature. Some fraction of the electrons and holes will recombine depending on the energy and type of the incident particle [90].

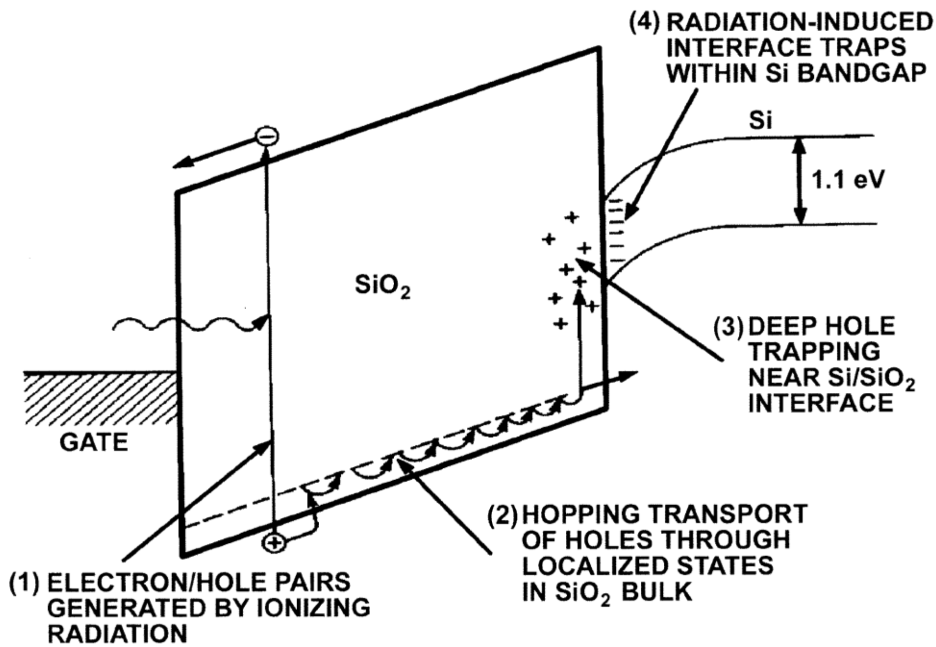

Figure 1.7. Schematic energy band diagram for a MOS structure, indicating major physical processes underlying radiation response [90].

The second process in Figure 1.7 is the transport of the holes to the Si/SiO_2 interface. This process is dispersive, meaning that it takes place over many decades in time [90]. The third process in Figure 1.7 is that, when the holes reach the Si interface, some fall

into relatively deep trap states with long characteristic emission times [90]. The fourth major component of MOS radiation response is the buildup of interface traps at the Si/SiO_2 interface [90]. These traps are localized states with energy levels in the Si band gap.

Oxide Traps (ΔN_{ot}):

A primary oxide defect in SiO_2, which leads to hole trapping, is known as an *E'* center, which is associated with an oxygen vacancy. It is identified as a trivalent silicon atom with an unpaired electron, back-bonded to three other oxygen atoms [91],[92]. These positively charged defects cause the threshold voltage to shift negatively. This causes nMOS devices to be turned on at lower voltages, while increasing the magnitude of voltage necessary to turn on pMOS devices.

Interface Traps (ΔN_{it}):

Interface trap formation was described as a two-stage process by McLean. He proposed that during the first stage, the radiation-generated holes free hydrogen ions in the SiO_2 bulk. In the second stage, these protons undergo dispersive hopping transport to the interface. When they reach the interface, they react, and break the SiH bonds already there, forming H_2 and a trivalent Si defect. In most MOS devices, interface traps above the midgap energy of Si are acceptor-like, while those in the lower half of the band gap are donor-like. Including both the donor-like and acceptor-like traps, the interface traps are charge neutral when the surface potential is at midgap [93].

Border Traps:

The term "border traps" was first introduced by D. M. Fleetwood in 1992 [94]. They are described as near-interfacial oxide traps that are able to exchange charge with the underlying silicon on the time scale of the measurements [95]. The location of these traps is very close to the interface and their response to the electrical sweep can make them look like slow interface traps [96].

REFERENCES:

[1] D. M. Long, D. G. Millward, and J. Wallace, “Dose enhancement effects in semiconductor devices,” *IEEE Trans. Nucl. Sci.*, vol. NS-29, pp. 1980–1984, 1982.

[2] F. Faccio and G. Cervelli, “Radiation-induced edge effects in deep sub-micron CMOS transistors,” *IEEE Trans. Nucl. Sci*., vol. 52, no. 6, pp. 2413-2420 (2005).

[3] L. Peters, “Choices and challenges for STI,” Semicond. Int., pp. 69-76, Apr. 1999.

[4] D. M. Fleetwood, D. E. Beutler, L. J. Lorence, Jr., D. B. Brown, B. L. Draper, L. C. Riewe, H. B. Rosenstock, and D. P. Knott, “Comparison of enhanced device response and predicted x-ray dose enhancement effects in MOS oxides,” *IEEE Trans. Nucl. Sci.*, vol. 35, no. 6, pp. 1265–1271, Dec. 1988.

[5] D. M. Fleetwood, P. S. Winokur, R. W. Beegle, P. V. Dressendorfer, and B. L. Draper, “Accounting for dose-enhancement effects with CMOS transistors,” *IEEE Trans. Nucl. Sci.*, vol. 32, no. 6, pp. 4369–4375, Dec. 1985.

[6] D. M. Fleetwood, P. S. Winokur, L. J. Lorence Jr., W. Beezhold, P. V. Dressendorfer and J. R. Schwank, “The response of MOS devices to dose-enhanced low-energy radiation,” *IEEE Trans. Nucl. Sci.*, vol. 33, no. 6, pp. 1245–1251, Dec. 1986.

[7] W. Beezhold, D. E. Beutler, J.C. Garth and P. J. Griffin, “A review of the 40-year history of the NSREC’s dosimetry and facilities session,” *IEEE Trans. Nucl. Sci.*, vol. 50, no. 3, pp. 635–652, Jun. 2003.

[8] J. C. Ashley, C. J. Tung, R. H. Ritchie, and V. E. Anderson, “Calculations of mean free paths and stopping powers of low energy electrons (10 keV) in solids using a statistical model,” *IEEE Trans. Nucl. Sci.*, vol. NS-23, pp. 1833–1837, 1976.

[9] J. C. Ashley, “Inelastic interactions of low-energy electrons with organic solids: Simple formulae for mean free paths and stopping powers,” *IEEE Trans. Nucl. Sci.*, vol. NS-27, pp. 1454–1458, 1980.

[10] J. C. Ashley, C. J. Tung, and R. H. Ritchie, “Electron interaction cross section in Al and Al2O3,” *IEEE Trans. Nucl. Sci.*, vol. NS-22, pp. 2533–2536, 1975.

[11] J.C. Ashley and V.E. Anderson, “Inelastic interactions of electrons with polystyrene: Calculations of mean free paths, stopping powers and CSDA ranges,” *IEEE Trans. Nucl. Sci.*, vol. NS-25, pp. 1566–1570, 1978.

[12] J. C. Ashley and V. E. Anderson, “Energy losses and mean free paths of electrons in silicon dioxide,” *IEEE Trans. Nucl. Sci.*, vol. NS-28, pp. 4131–4136, 1981.

[13] C. J. Tung, J. C. Ashley, and R. H. Ritchie, "Range of low-energy electrons in solids," *IEEE Trans. Nucl. Sci.*, vol. NS-26, pp. 4874–4878, 1979.

[14] S. M. Seltzer, "Electron electron-bremsstrahlung and proton depth-dose data for space-shielding applications," *IEEE Trans. Nucl. Sci.*, vol. NS-26, pp. 4896–4904, 1979.

[15] H. Bichsel and S. Yu, "Straggling of relativistic charged particles: Corrections to the Landau–Vavilov straggling functions in the hydrogenic wave-function approximation," *IEEE Trans. Nucl. Sci.*, vol. NS-19, pp. 172–174, 1972.

[16] C. M. Kwei, "Straggling of energy loss for electrons transmitted through aluminum," *IEEE Trans. Nucl. Sci.*, vol. NS-28, pp. 4172–4176, 1981.

[17] O. Chibani, "New algorithms for the Vavilov distribution calculation and the corresponding energy loss sampling," *IEEE Trans. Nucl. Sci.*, vol. 45, pp. 2288–2292, 1998.

[18] S. M. Seltzer and M. J. Berger, "Improved bremsstrahlung cross sections," *IEEE Trans. Nucl. Sci.*, vol. NS-30, pp. 4368–4370, 1983.

[19] C. J. Tung and C. P. Wang, "Multiple scattering of low energy electrons in aluminum," *IEEE Trans. Nucl. Sci.*, vol. NS-30, pp. 4409–4412, 1983.

[20] R. D. Birkhoff, "The electron flux spectra and radiation yields in solids irradiated by beta rays," *IEEE Trans. Nucl. Sci.*, vol. NS-16, pp. 233–241, 1969.

[21] R. E. Ritchie and V. E. Anderson, "Electron slowing-down-cascade spectra in solids," *IEEE Trans. Nucl. Sci.*, vol. NS-18, pp. 141–149, 1971.

[22] J. C. Garth and J. V. O'Brien, "Numerical solution of the Spencer–Lewis equation for kilovolt electron transport in plane slabs," *IEEE Trans. Nucl. Sci.*, vol. NS-20, pp. 82–90, 1973.

[23] W. L. Filippone, S. Woolf, and J. C. Garth, "Two-dimensional transport equation calculations of dose profiles due to electron beam irradiation," *IEEE Trans. Nucl. Sci.*, vol. NS-34, pp. 1564–1568, 1987.

[24] D. J. Strickland, "Soft X-ray photoemission," *IEEE Trans. Nucl. Sci.*, vol. NS-24, pp. 2499–2504, 1977.

[25] D. J. Strickland and D. L. Lin, "The photoemission spectrum for an exploding wire radiator source incident on Al and Au," *IEEE Trans. Nucl. Sci.*, vol. NS-25, pp. 1571–1576, 1978.

[26] T. A. Dellin and C. J. MacCallum, "Analytical prediction of photo- Compton emission currents," *IEEE Trans. Nucl. Sci.*, vol. NS-20, pp. 91–96, 1973.

[27] T. A. Dellin, K. W. Dolan, and C. J. MacCallum, "Photo-Compton currents at material interfaces: Theory and experiment," *IEEE Trans. Nucl.Sci.*, vol. NS-21, pp. 227–234, 1974.

[28] T. A. Dellin, R. E. Huddleston, and C. J. MacCallum, "Second-generation analytical photo-Compton current methods," *IEEE Trans. Nucl.Sci.*, vol. NS-22, pp. 2549–2555, 1975.

[29] W. L. Chadsey, C. W. Wilson, and V. W. Pine, "X-ray photoemission calculations," *IEEE Trans. Nucl. Sci.*, vol. NS-22, pp. 2345–2350, 1975.

[30] B. L. Beers and V. W. Pine, "Functional expansion technique for Monte Carlo electron transport calculations," *IEEE Trans. Nucl. Sci.*, vol. NS-23, pp. 1850–1856, 1976.

[31] A. R. Frederickson, J. T. Bell, and E. A. Beidl, "Analytic approximation for charge current and deposition by 0.1 to 100 MeV electrons in thick slabs," *IEEE Trans. Nucl. Sci.*, vol. 42, pp. 1910–1921, 1995.

[32] W. L. Chadsey and I. Kohlberg, "The computation of photon radiation induced electron emission," *IEEE Trans. Nucl. Sci.*, vol. NS-18, pp. 150–161, 1971.

[33] J. A. Halbleib, Sr., "Electron transport in the presence of uniform magnetic fields," *IEEE Trans. Nucl. Sci.*, vol. NS-21, pp. 221–226, 1974.

[34] J. A. Halbleib, Sr. and W. H. Vandervender, "Coupled electron/photon transport in static external magnetic fields," *IEEE Trans. Nucl. Sci.*, vol. NS-22, pp. 2356–2361, 1975.

[35] J. A. Halbleib, R. P. Kensek, and G. D. Valdez, "ITS: The integrated TIGER series of electron photon transport codes: Version 3.0," *IEEE Trans. Nucl. Sci.*, vol. 39, pp. 1025–1030, 1992.

[36] L. J. Lorence, W. E. Nelson, and J. E. Morel, "Coupled electron-photon transport calculations using the method of discrete ordinates," *IEEE Trans. Nucl. Sci.*, vol. NS-32, pp. 4416–4420, 1985.

[37] L. J. Lorence, Jr., "Electron photoemission predictions with CEPXS/ONETRAN," *IEEE Trans. Nucl. Sci.*, vol. 35, pp. 1288–1293, 1988.

[38] L. J. Lorence, "CEPXS/ONELD version 2.0: A discrete ordinates code package for general one-dimensional coupled electron-photon transport," *IEEE Trans. Nucl. Sci.*, vol. 39, pp. 1031–1034, 1992.

[39] L. J. Lorence, R. P. Kensek, J. A. Halbleib, and J. E. Morel, “Adjoint electron-photon transport Monte Carlo calculations with ITS,” *IEEE Trans. Nucl. Sci.*, vol. 42, pp. 1895–1901, 1995.

[40] R. P. Kensek, L. J. Lorence, J. A. Halbleib, and J. E. Morel, “Space applications of the MITS electron-photon Monte Carlo transport code system,” *IEEE Trans. Nucl. Sci.*, vol. 43, pp. 2724–2730, 1996.

[41] H. M. Colbert, “SANDYL: A computer program for calculating combined photon-electron transport in complex systems,” Sandia Livermore Laboratories, Rep. SLL-74-0012, 1974.

[42] N. A. Lurie, D. K. Steinman, L. Harris, Jr., and J. P. Wondra, “Gamma-ray energy deposition in silicon detectors,” *IEEE Trans. Nucl. Sci.*, vol. NS-22, pp. 2582–2585, 1975.

[43] J. A. Halbleib, Sr., G. J. Lockwood, and G. H. Miller, “Optimization of bremsstrahlung energy deposition,” *IEEE Trans. Nucl. Sci.*, vol. NS-23, pp. 1881–1885, 1976.

[44] J. A. Halbleib, G. J. Lockwood, and L. D. Posey, “Theoretical and experimental studies of multiple foil bremsstrahlung sources,” *IEEE Trans. Nucl. Sci.*, vol. NS-28, pp. 4166–4171, 1981.

[45] T.W. L. Sanford, J. A. Halbleib, andW. Beezhold, “Experimental check of bremsstrahlung dosimetry predictions for 0.75 MeV electrons,” *IEEE Trans. Nucl. Sci.*, vol. NS-32, pp. 4410–4415, 1985.

[46] T.W. L. Sanford, J. A. Halbleib,W. Beezhold, and L. J. Lorence, “Experimental verification of nonequilibrated bremsstrahlung dosimetry predictions for 0.75 MeV electrons,” *IEEE Trans. Nucl. Sci.*, vol. NS-33, pp. 1261–1265, 1986.

[47] T. W. L. Sanford, D. E. Beutler, J. A. Halbleib, and D. P. Knott, “Experimental verification of bremsstrahlung production and dosimetry predictions for 15.5 MeV electrons,” *IEEE Trans. Nucl. Sci.*, vol. 38, pp. 1160–1170, 1991.

[48] T.W. L. Sanford, J. A. Halbleib, D. E. Beutler, and D. P. Knott, “Experimental verification of dosimetry predictions of bremsstrahlung attenuation as a function of material and electron energy,” *IEEE Trans. Nucl.Sci.*, vol. 40, pp. 1409–1417, 1993.

[49] D. E. Beutler, J. A. Halbleib, T.W. L. Sanford, and D. P. Knott, “Experimental verification of bremsstrahlung production and dosimetry predictions as a function of energy and angle,” *IEEE Trans. Nucl. Sci.*, vol. 41, pp. 2727–2736, 1994.

[50] T. W. L. Sanford, J. A. Halbleib, G. Cooperstein, and B. V. Weber, "Potential enhancement of warm X-ray dose from a reflexing bremsstrahlung diode," *IEEE Trans. Nucl. Sci.*, vol. 42, pp. 1902–1909, 1995.

[51] S. Woolf and A. R. Frederickson, "Photon spectra in Co-8 test cells," *IEEE Trans. Nucl. Sci.*, vol. NS-30, pp. 4371–4376, 1983.

[52] S. Woolf and E. A. Burke, "Monte Carlo calculations of irradiation test photon spectra," *IEEE Trans. Nucl. Sci.*, vol. NS-31, pp. 1089–1094, 1984.

[53] R. W. Tallon, D. C. Koller, R. M. Pelzl, R. D. Pugh, and R. D. Bellem, "5 to 160 keV continuous-wave X-ray spectral energy distribution and energy flux density measurements," *IEEE Trans. Nucl. Sci.*, vol. 41, pp. 2112–2117, 1994.

[54] R. D. Bellem, K. L. Critchfield, R. M. Pelzl, R. D. Pugh, and R. W. Tallon, "Analytical and experimental dosimetry techniques for calibrating a low energy X-ray radiation source," *IEEE Trans. Nucl. Sci.*, vol. 41, pp. 2139–2146, 1994.

[55] J. R. Turinetti, K. L. Critchfield, J. R. Chavez,W. T.Kemp, R. D. Bellem, and D. E. Beutler, "Determination of low energy (<160 keV) X-ray spectra and verification of transport calculations through silicon," *IEEE Trans. Nucl. Sci.*, vol. 44, pp. 2065–2070, 1997.

[56] J. C. Garth and J. R. Turinetti, "Gamma-ray transport through material layers," *IEEE Trans. Nucl. Sci.*, vol. 44, pp. 2058–2064, 1997.

[57] ASTM E666-91, "Standard practice for calculating absorbed dose for gamma or X-radiation," in *Annual Book of ASTM Standards* Coshohocken, PA, 1995, vol. 1202.

[58] D. R. Schallhorn and L. D. Buxton, "Predicted and measured depth dose profiles for pulsed electron spectra," *IEEE Trans. Nucl. Sci.*, vol. NS-16, pp. 242–249, 1969.

[59] S. E. Chappell and J. C. Humphreys, "Silicon detector measurements of energy deposition in aluminum by monoenergetic electrons," *IEEE Trans. Nucl. Sci.*, vol. NS-17, pp. 272–277, 1970.

[60] G. J. Lockwood, G. H. Miller, and J. A. Halbleib, "Absolute measurement of low energy electron deposition profiles in semi-infinite geometries," *IEEE Trans. Nucl. Sci.*, vol. NS-20, pp. 326–330, 1973.

[61] G. H. Miller,G. J. Lockwood, and J. A. Halbleib, "Improved calorimetric method for energy deposition measurement," *IEEE Trans. Nucl. Sci.*, vol. NS-21, pp. 359–365, 1974.

[62] G. J. Lockwood, G. H. Miller, and J. A. Halbleib, "Simultaneous integral measurement of electron energy and charge albedos," *IEEE Trans. Nucl. Sci.*, vol. NS-22, pp. 2537–2542, 1975.

[63] G. J. Lockwood, G. H. Miller, and J. A. Halbleib, "Electron energy deposition in multilayer geometries," *IEEE Trans. Nucl. Sci.*, vol. NS-23, pp. 1862–1866, 1976.

[64] G. J. Lockwood, J. A. Halbleib, and G. H. Miller, "Electron transport in reactor materials," *IEEE Trans. Nucl. Sci.*, vol. NS-25, pp. 1581–1585, 1978.

[65] A. Fleetwood, R. Fleetwood, K. Kerris, G. Merkel, and M. Smith, "Improved e-beam electron range measurements: Experiments and analysis," *IEEE Trans. Nucl. Sci.*, vol. 35, pp. 1294–1299, 1988.

[66] A. R. Frederickson and S.Woolf, "Electron beam current penetration in semi infinite slabs," *IEEE Trans. Nucl. Sci.*, vol. NS-28, pp. 4186–4193, 1981.

[67] G. A. Carlson, D. E. Beutler, K. D. Seager, and D. P. Knott, "Comparison of measured responses in two spectrally-sensitive X-ray detectors to predictions obtained using the ITS radiation transport code," *IEEE Trans. Nucl. Sci.*, vol. 35, pp. 1272–1277, 1988.

[68] T.P. Ma and P.V. Dressendorfer, "Ionizing radiation effects in MOS devices and circuits," *J. Wiley & Sons*, USA, 1989.

[69] J. A. Wall and E. A. Burke, "Gamma dose distributions at and near the interface of different materials," *IEEE Trans. Nucl. Sci.*, vol. NS-17, pp. 305–309, 1970.

[70] A. R. Frederickson and E. A. Burke, "Ionization, secondary emission and Compton currents at gamma irradiated interfaces," *IEEE Trans. Nucl. Sci.*, vol. NS-18, pp. 162–169, 1971.

[71] A. R. Frederickson, "Charge deposition profiles near irradiated material interfaces," *IEEE Trans. Nucl. Sci.*, vol. NS-23, pp. 1867–1874, 1976.

[72] L. F. Lowe, J. R. Cappelli, and E. A. Burke, "Dosimetry errors in Co-60 gamma cells due to transition zone phenomena," *IEEE Trans. Nucl. Sci.*, vol. NS-29, pp. 1992–1995, 1982.

[73] J. C. Garth, W. L. Chadsey, and R. L. Sheppard, Jr., "Monte Carlo analysis of dose profiles near photon irradiated material interfaces," *IEEE Trans. Nucl. Sci.*, vol. NS-22, pp. 2562–2567, 1975.

[74] W. L. Chadsey, "POEM: A fast Monte Carlo code for the calculation of X-ray photoemission and transition zone dose and current," AFCRL TR-75-0324, 1975.

[75] E. A. Burke and J. C. Garth, “An algorithm for energy deposition at interfaces,” *IEEE Trans. Nucl. Sci.*, vol. NS-23, pp. 1838–1843, 1976.

[76] W. L. Chadsey, “X-ray dose enhancement,” *IEEE Trans. Nucl. Sci.*, vol. NS-25, pp. 1591–1597, 1978.

[77] J. C. Garth, “Diffusion equation model for kilovolt electron transport at x-irradiated interfaces,” *IEEE Trans. Nucl. Sci.*, vol. NS-25, pp. 1598–1606, 1978.

[78] J. C. Garth, “High energy extension of the semi-empirical model for energy deposition at interfaces,” *IEEE Trans. Nucl. Sci.*, vol. NS-28, pp. 4145–4151, 1981.

[79] J. C. Garth, “An algorithm for calculating dose profiles in multilayered devices using a personal-computer,” *IEEE Trans. Nucl. Sci.*, vol. NS-33, pp. 1266 –1270, 1986.

[80] J. C. Garth, “Calculations of dose enhancement in device structures,” *Nucl. Instrum. Methods B*, vol. 40/41, pp. 1266–1270, 1989.

[81] J. A. Halbleib, “A new approach to the Monte Carlo prediction of interface phenomena,” *IEEE Trans. Nucl. Sci.*, vol. NS-33, pp. 1287–1291, 1986.

[82] J. C. Garth, K. L. Critchfield, J. R. Turinetti, and D. E. Beutler, “A comprehensive comparison of CEPXS/ONELD calculations of dose enhancement with the Co-60 data set of Wall and Burke,” *IEEE Trans. Nucl. Sci.*, vol. 43, pp. 2731–2741, 1996.

[83] J. R. Schwank, "Total dose effects in MOS devices," *IEEE NSREC Short Course*, p. III-1, 2002.

[84] F. B. McLean and T. R. Oldham, "Basic mechanisms of radiation effects in electronic materials and devices," *Harry Diamond Laboratories Technical Report*, vol. no. HDL-TR-2129, 1987.

[85] R. D. Evans, *The Atomic Nucleus*. New York: McGraw-Hill, 1955.

[86] M. R. Shaneyfelt, D. M. Fleetwood, J. R. Schwank, and K. L. Hughes, "Charge yield for 10-keV X-ray and Cobalt-60 irradiation of MOS devices," *IEEE Trans. Nucl. Sci.*, vol. 38, p. 1187, 1991.

[87] R. C. Hughes, "Charge carrier transport phenomena in amorphous SiO2 direct measurement of the drift mobility and lifetime," *Phys. Rev. Lett.*, vol. 30, p. 1333, 1973.

[88] L. W. Massengill, "SEU modeling and prediction techniques," *IEEE NSREC Short Course*, p. 1, 1993.

[89] T. Weatherford, "Total dose effects in MOS devices," *IEEE NSREC Short Course*, p. IV-1, 2002.

[90] T. R. Oldham and F. B. McLean, “Total ionizing dose effects in MOS oxides and devices,” *IEEE Trans. Nucl. Sci.*, vol. 50, no. 3, pp. 483-499, Jun. 2003.

[91] P. M. Lenahan and P. V. Dressendorfer, “Radiation induced paramagnetic defects in MOS structures,” *IEEE Trans. Nucl. Sci.*, vol. 29, no. 6, pp. 1459-1461, Dec. 1982.

[92] P. M. Lenahan and P. V. Dressendorfer, “Hole traps and trivalent silicon centers in metal/oxide/silicon devices,” *J. Appl. Phys.*, vol. 55, no. 10, pp. 3495-3499, May 1984.

[93] W. L. Warren, E. H. Poindexter, M. Offenberg, and W. Muller-Warmuth, “Paramagnetic point defects in amorphous silicon dioxide and amorphous silicon nitride thin films,” *J. Electrochem. Soc.*, vol. 139, no. 3, pp. 872-880, Mar. 1992.

[94] D. M. Fleetwood, “Border traps in MOS devices,” *IEEE Trans. Nucl. Sci.*, vol. 39, no. 2, pp. 269-271, Apr. 1992.

[95] D. M. Fleetwood and J. H. Scofield, “Evidence that similar point defects cause *1/f* noise and radiation-induced-hole trapping in MOS transistors,” *Phys. Rev. Lett.*, vol. 64, no. 5, pp. 579-582, Jan. 1990.

[96] J. J. Simonne, G. Blasquez, and G. Barbottin, *1/f Noise in MOSFETs*, vol. 2. Amsterdam: Elsevier, 1989, pp. 639-657.

CHAPTER II

HIGH-K GATE OXIDES IN MODERN CMOS DEVICES

In high-κ based devices, SiO_2 gate insulators are being replaced by films that have a higher absolute permittivity κ compared to SiO_2. A lot of research is being done in order to study the material properties and the reliability of these new material films. Factors such as stability of the as-grown high-κ films on silicon, nature of the interface etc. are being actively researched in order to ensure the proper functionality and reliability of the CMOS device involving these high-κ films. It is also very important to characterize the energy and dose deposited in such high-κ films in order to understand the radiation response of devices containing such high-κ films that are employed in space missions. Many high-κ films that are being actively researched like hafnium oxide; tantalum oxides also have a high atomic number, and hence x-rays may lead to dose enhancement effects in such films. We will discuss these results in details in later chapters but here in this chapter, we consider the various advantages, issues and material properties of high-κ films like HfO_2.

2.1 HAFNIUM OXIDE (HFO_2) – THE MATERIAL FOR MODERN DEEP SUBMICRON CMOS TECHNOLOGIES

Technology scaling according to Moore's law has resulted in rapid progress in CMOS integrated circuit (IC) technology. The key features are speed, low static off-state power, and a range of output voltages. This has been possible by scaling the dimensions of the field effect transistor MOSFET [1]–[3]. This has led to a tremendous progress in the area of microprocessors as well as wireless devices [4]. The scaling of the Si-based MOSFET is based on the material and electrical properties of the gate oxide which is silicon dioxide in Si-based MOS devices. Thermally grown SiO_2 has thermodynamical and electrical stability, high-quality interface and very good electrical isolation. In modern CMOS based devices, defect densities are ~ $10^{10}/cm^2$, mid-gap interface state densities of ~ $10^{10}/(cm^2.eV)$ have been reported [5], [7]. These remarkable electrical properties make SiO_2 an ideal material and very hard to replace by alternate gate dielectric materials in modern high-κ technologies.

The density of transistors on a wafer has increased owing to the large demands on chip's performance [4]. This fast shrinking of the transistor feature size has led to reduced channel lengths and thinner oxides.

The drive current in the non-saturation region can be written as

$$I_D = \mu C_{ox} \frac{W}{L} (V_G - V_T - \frac{V_D}{2}) V_D$$

where W is the width of the transistor channel, L is the channel length, μ is the channel carrier mobility assumed constant here, C_{ox} is the capacitance per unit area of the gate dielectric, V_G and V_D are the gate and drain voltages, and V_T is the threshold voltage.

In order to increase the gate capacitance, let us consider a capacitor

$$C_{ox} = \kappa \varepsilon_0 \frac{A}{t}$$

where κ is the dielectric constant, A is the area of the capacitor, and t is the gate oxide thickness. Thus, C of a capacitor can be expressed in terms of t_{eq} - equivalent oxide thickness and for κ ~3.9, dielectric constant of SiO_2.

For technology nodes beyond 90 nm, a number of issues have to be addressed to continue to support scaling. Direct tunneling of electrons through the oxide increases the off-state leakage current in these MOS devices [6], [7].

The physical thickness of an alternative dielectric employed to achieve the equivalent capacitance density of t_{eq} can be obtained from the expression [8], [9].

$$t_{high-\kappa} = \kappa_{high-\kappa} \frac{t_{eq}}{\kappa_{ox}}$$

2.2 ALTERNATE GATE DIELECTRICS MATERIAL FOR MODERN CMOS TECHNOLOGIES:

The material properties that the gate dielectrics must meet in order to be successfully integrated as a gate dielectric material in CMOS technology are as listed below:

Permittivity and barrier height:

The gate dielectric material must have a higher permittivity than that of SiO_2. In addition to permittivity, the barrier height for the tunneling process must be considered. In case of electrons traveling from the silicon towards the gate electrode, the conduction band offset, $\Delta E_c = q[X - (\Phi_M - \Phi_B)]$ must be considered. Again, for electrons traveling from the gate electrode to the silicon, Φ_B must be considered. Leakage current increases exponentially with decreasing barrier height and thickness of films for direct tunneling of electrons [11],[12].

Researchers [13] have reported that Ta_2O_5 and $SrTiO_3$ have ΔE_c ~ 0.5 eV on silicon. They further reported that ΔE_c ~ 2.3 eV for Al_2O_3, and ΔE_c ~1.5 eV for ZrO_2 and $ZrSiO_4$. These results shed light and are very crucial in getting an estimate of the barrier height for several alternate dielectric materials. HfO_2 and ZrO_2 stand out as the best possible alternatives for SiO_2 in the MOS configuration. Other binary oxides such as Al_2O_3, Y_2O_3, Ta_2O_5 are also materials that have been or are being considered.

Thermal stability of films:

Good thermal stability in contact with Si is an important aspect of thin films. It plays an important role in determining the electrical performance of the device. There are many high-κ metal oxide systems that form unstable films with Si. These films react with the silicon substrate under growth conditions to form an unwanted interfacial layer. The thermodynamics of these systems is critical in determining the overall device performance. Hence the interface engineering with Si is an important aspect to control the stable growth of these films.

Quality of the interface:

The promising potential alternate high-k gate oxide must be able to form an interface of supreme quality with the silicon. The interface quality must be as good as to that of SiO_2 interface with silicon. The interface must have a low density of intrinsic defects at the interface of Si with the gate oxide and also in the bulk of the material. The charge carriers must have a high mobility in the channel and also a high gate dielectric lifetime. SiO_2 forms the best interface with silicon. SiO_2 gate dielectrics have a mid-gap interface trap density $D_{it} \sim 10^{10}$ traps/cm^2. High-k materials have $D_{it} \sim 10^{11}$–10^{12} traps/cm^2.

Film quality:

The potential advanced gate dielectrics studied are polycrystalline or single crystalline films. The material should remain in an amorphous state throughout the CMOS process flow steps. The grain boundaries in the polycrystalline gate dielectrics serve as high-

leakage paths. Thus an amorphous interfacial layer is required to decrease leakage current.

Compatibility with process flow:

The method of dielectric deposition during the CMOS process flow step is important in determining the film quality and its material properties. The growth process must be compatible with CMOS process flow steps. It must also be economical to manufacture. Also, as all the growth techniques typically occur under non-equilibrium conditions, one might observe material properties different from film growth under equilibrium conditions.

2.3 CHOICE OF GATE ELECTRODE

In order to integrate alternate gate dielectric into CMOS process flow, compatibility with Si-based gates is essential. This is because it is possible to get the desired threshold voltage V_T *for* both *n*MOS and *p*MOS devices using dopant implantation. The recipes for poly-silicon gate integration are very well formulated in industry. However, the alternate gate dielectric based devices require metal gates.

In a dual-work-function gate, in order to effectively control V_T , ~4.9 eV for PMOS and ~4.4 eV for NMOS is required. In a CMOS process flow step, the metal gate is formed before the source and drain formation and annealing treatments. Thermal stability during

the 1000 °C, 10 sec anneal is used as an important parameter. Only few metal gates are able to satisfy these criteria. TaN and TaSiN [16] are being explored for integration in NMOS [17], [18]. Noble metals (Pt) are good candidates in PMOS devices [19]. TiN is a good candidate for a metal gate. The work function is strongly dependent on the composition of the film, deposition process itself and the history of the thin film.

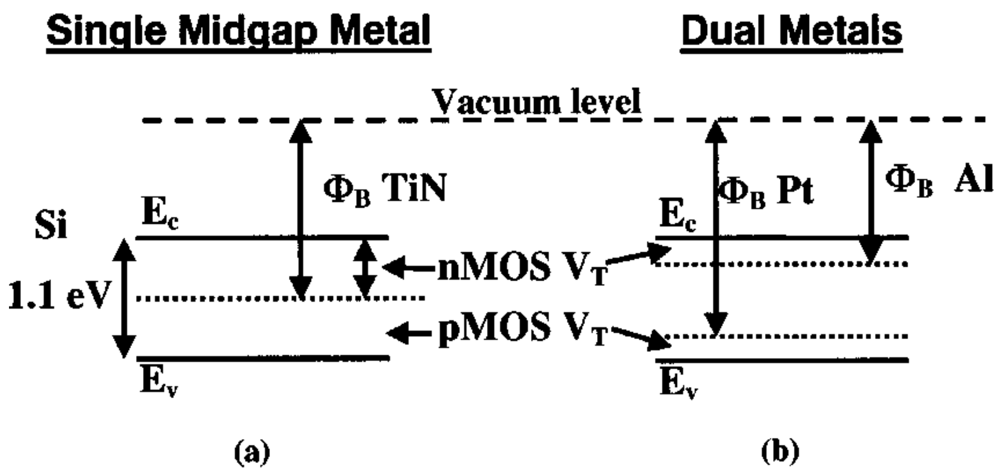

Figure 2.1. Energy diagrams of threshold voltages for nMOS and pMOS devices using (a) TiN (midgap) metal gates and (b) Pt (dual) metal gates [7].

2.4 RELIABILITY & CHARGE TRAPPING ISSUES IN HIGH-κ MOS DEVICES

Large magnitudes of leakage currents with decreasing SiO_2 gate oxide thickness are the main drivers for high-κ gate materials research. However, the flatband and threshold voltages shift occur during operation for high-κ devices. The hysteresis in V_{th} is due to charge trapping in the pre-existing traps. Charge trapping can be characterized by DC

measurements on MOS devices. This is shown in the I_d-V_g and C-V_g curves below in Figure 2.2(a) and 2.2(b) [20].

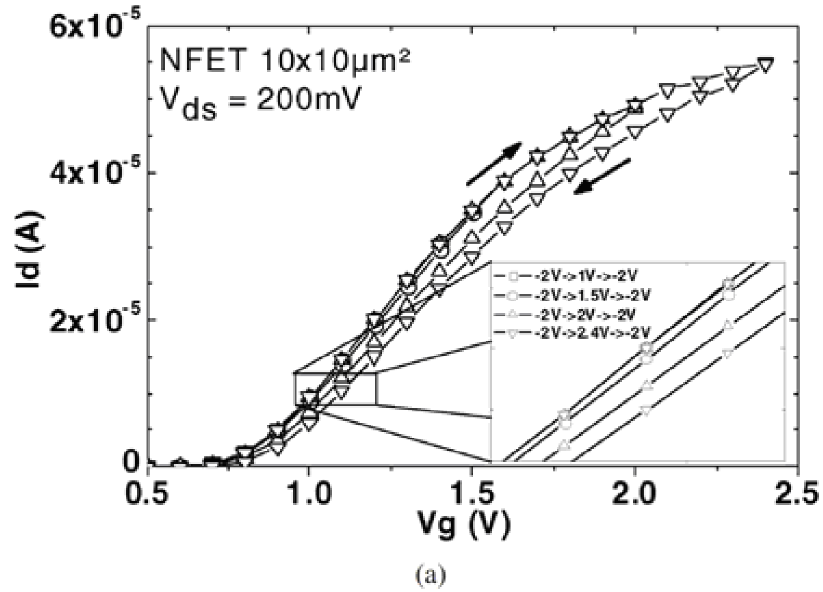

(a)

Figure 2.1 (a) I_d –V_g characteristic of 4.5 nm HfO_2 NFET [20].

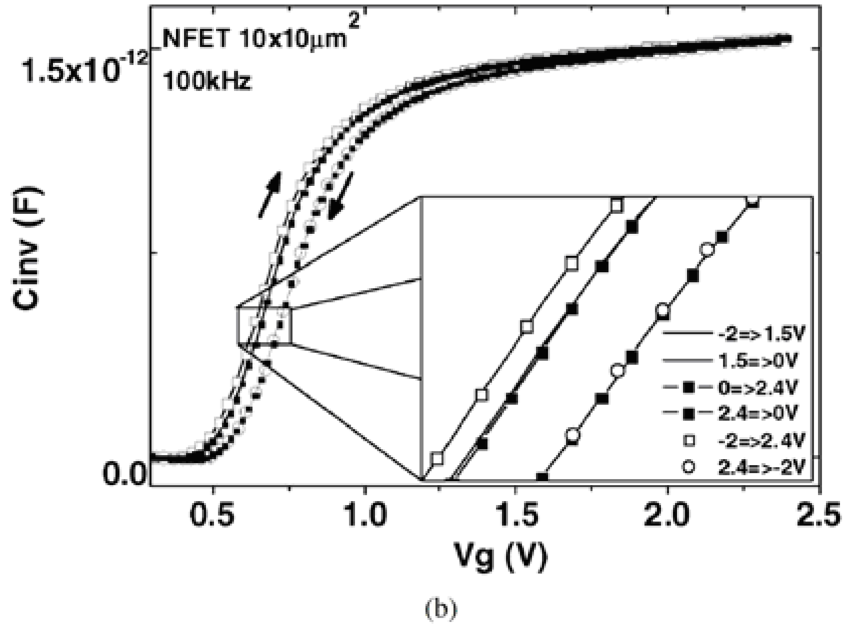

(b)

Figure 2.2 (b) C–V_g characteristic of 4.5 nm HfO_2 NFET [20].

In order to characterize fast transient component of the charge trapping observed in HfO_2, fast measurement techniques, single-pulsed [21] and the multiple pulsed [22] techniques, can also be used. Also, charge-pumping technique can be used to assess the interface trap density (D_{it}) of high-κ MOS devices from the substrate current. The charge pumping technique is novel in that the base level of the pulse is fixed and a variable amplitude signal is applied to the gate [20].

At positive bias, electron trapping in the high-κ layer is the primary mechanism for charge trapping. Depending on the interfacial layer thickness and the theory of oxide traps, two types of trapping mechanisms are considered: a capture and subsequent trapping of HfO_2 conduction band electrons or an electron direct tunneling from silicon substrate to defect. A simple model was proposed with a defect energy level in HfO_2 thin film situated between the silicon and hafnia conduction band energies [20]. However, based on mobility degradation in high-κ MOS devices, it is also proposed [20] that the defects are located in the HfSiO and SiO_2 interface. Applying a negative gate voltages, trapped charge can be fully recovered [21]. However, at positive voltages, it has been observed that a partial recovery of charge occurs. The partial detrapping can be explained on the basis of back-tunneling of electron from traps to the silicon, and secondly, from a Poole-Frenkel mechanism of conduction of electrons from traps to the gate.

The nature of the electron traps in the HfO_2 is to be determined and research is ongoing. The presence of lattice defects affects the functionality of high-k gate dielectrics. Oxygen vacancies play a crucial role in the V_{th} instability. These defects can trap electrons from

not only the hafnia conduction band but also from silicon substrate. These results show consistency with electron spin resonance (ESR) measurements. These experiments predict the presence of O_2^- species, a negatively charged defect which can be attributed to the trapping of electrons in HfO_2 film [23].

REFERENCES:

[1] R. H. Dennard, F. H. Gaensslen, H.-N. Yu, V. L. Rideout, E. Bassous, and A. R. LeBlanc, "Design of Ion Implanted MOSFET's with Very Small Physical Dimensions," J. IEEE SC–9, 256, 1974.

[2] G. Baccarani, M. R. Wordeman, and R. H. Dennard, "Generalized Scaling theory of MOSFET design", IEEE Trans. Elec tron Devices 31, 452 (1984).

[3] P. A. Packan, "Pushing the Limits", Science 285, 2079, 1999.

[4] The International Technology Roadmap for Semiconductors, Semiconductor Industry Association.

[5] M. Bohr, "Intel's 90 nm technology: Moore's Law and more," *Intel Developer Forum*, Fall 2002.

[6] S.K. Dixit, "Radiation induced charge trapping studies of advanced Si and SiC based MOS devices," *PhD thesis*, 2008.

[7] G. D. Wilk, R. M. Wallace, and J. M. Anthony, "High-k dielectrics: Current status and materials properties considerations," *J. Appl. Phys.*, vol. 89, p. 5243, 2001.

[8] R. S. Muller and T. I. Kamins, Device Electronics for Integrated Circuits. New York: Wiley, 1986.

[9] S. M. Sze, *Physics of semiconductor devices*. New York: John Wiley & Sons, 1981.

[10] D. A. Muller, T. Sorsch, S. Moccio, F. H. Baumann, K. E-. Lutterodt, and G. Timp, "The electronic structure at the atomic scale of ultrathin gate oxides," *Nature*, vol. 399, p. 758, 1999.

[11] R. D. Shannon, " Dielectric polarizabilities of ions in oxides and fluorides," J. Appl. Phys. 73, 348, 1993.

[12] E. H. Nicollian and J. R. Brews, *MOS (Metal Oxide Semiconductor) Physics and Technology,* Wiley, New York, 1982.

[13] J. Robertson and C. W. Chen, "Schottky barrier heights of tantalum oxide, barium strontium titanate, lead titanate, and strontium bismuth tantalite," Appl. Phys. Lett. 74, 1168, 1999.

[14] J. Robertson, "Band offsets of wide-band-gap oxides and implications for future electronic devices, " J. Vac. Sci. Technol. B 18, 1785, 2000.

[15] R. Beyers, "Phase equilibria in thin film metallizations," J. Appl. Phys. 56, 147, 1984.

[16] K. J. Hubbard and D. G. Schlom, "Thermodynamic stability of binary oxides in contact With silicon," J. Mater. Res. 11, 2757, 1996.

[17] V. Misra, M. Kulkarni, G. Heuss, H. Zhong and H. Lazar, "Thermodynamics of binary oxides," Electrochem. Soc. Symp. PV 9, 291-298, 2009.

[18] S.B. Samavedam, "Poly-gate replacement through contact hole method," IEDM 17, 2002.

[19] H. Zhong, S.N. Hong, Y.S. Suh, H. Lazar, G. Heuss and V. Misra, " Properties of Ru-Ta Alloys as Gate Electrodes For NMOS and PMOS Silicon Devices," IEDM 467-470.

[20] G. Ribes et al. "Review on High-k Dielectric Reliability issues," *IEEE Trans.Dev. and Mat. Reliability*., vol. 5, no. 1, pp. 5-19 2005.

[21] A. Kerber et al., "Characterization of VT instability in SiO2/HfO2 gate dielectrics," Proceedings of IRPS, 2003.

[22] C. Leroux et al. "Characterization and modeling of hysteresis phenomena in high-k dielectrics," IEDM Tech. Digest., 2004.

[23] A.Y. Kang and P.M. Lenahan, "Electron Spin resonance observation of trapped electron centers in hafnium oxide on silicon," Appl. Phys. Lett., pp. 8316, 2003.

CHAPTER III

SIMULATION CODES

3.1 INTRODUCTION

In this chapter, we will briefly discuss the various simulators and codes that have been used to study the dose enhancement effects on MOS devices. We will compare the results from these various simulators in the subsequent chapters. We have made comparisons with the dose enhancements factors (DEFs) as predicted by these simulators wherever data from these simulators were available. These simulators include the Monte Carlo simulator TIGERP [1] and discrete ordinate codes CEPXS/ONETRAN [2], [3]. We have found generally good agreement between the numbers predicted by these simulators and our work using MRED 9.0.0 simulator [4], [5], [6].

3.2 CEPXS/ONETRAN:

The CEPXS/ONETRAN is a discrete ordinate simulator [7] that is used for solving one dimensional coupled electron-photon transport problems at various energies. It has been used in the past for solving problems involving ionizing radiation such as SGEMP, the problem of dose enhancement, space shielding calculations, the response of cables to x-rays etc. It has also been used to evaluate the dose and charge deposition at the interface

of complex high-Z/low-Z materials. The discrete ordinates codes are intended to provide the same degree of accuracy as the Monte Carlo codes but are faster than the Monte Carlo simulators.

Discrete ordinate simulators use a finite differences method in order to solve the transport problem. This method has been used both for studying neutral particle transport [8] and as well as electron transport [9],[10],[11].

The CEPXS/ONETRAN package contains four codes [2]; CEPXS is a cross-section code. PRE1D is a pre processor code. ONETRAN/ONELD is transport code. POST1D is a post processor code. PRE1D generates the input and POST1D integrates the output for the code based on the user demands.

The primary advantage of a discrete ordinate simulator like CEPXS/ONETRAN over Monte-Carlo codes is that it is possible to get accurate solutions using much less CPU time. In the latest version of the code (Version 2.0), the code automatically selects the finite difference methods depending on the problem and hence a user not knowledgeable on discrete ordinates techniques can also use the program.

The CEPXS/ONETRAN codes can predict energy and dose deposited in the sensitive structures with a high degree of accuracy. The factors which determine accuracy will depend on the assumptions used in the finite difference methods. The accurate solution of the transport equation is achieved by the improving upon the spatial, energy and angular

variable descriptions. The spatial domain is divided by meshing whereas the energy domain is divided into sub-groups. The angular domain is characterized by choosing a few discrete direction cosines depending on the problem at hand.

Higher number of mesh points, more energy groups and more discrete directions are used to get convergent solution to the problem. However, increasing the number of mesh points, energy groups and discrete directions increases the CPU time. This is similar to the effect of increasing the number of histories of particles in the Monte Carlo codes. However, the optimal solution can be obtained depending on the requirements of the problem.

Monte Carlo codes and discrete ordinate simulators have very different requirements for computation. The Monte Carlo codes require more processing time to execute than CEPXS/ONETRAN. On the other hand, CEPXS/ONETRAN needs much more computer memory.

The CEPXS/ONETRAN code can calculate both the kerma and the dose profiles. Figure 3.1 below shows the dose and kerma profiles calculated by the CEPXS/ONETRAN simulator for a particular case. The fluence is 1 photon/cm^2. In order to calculate kerma, the assumption made is that the secondary electrons deposit the energy locally. The energy lost during the radiative interactions fully escapes the sensitive volume.

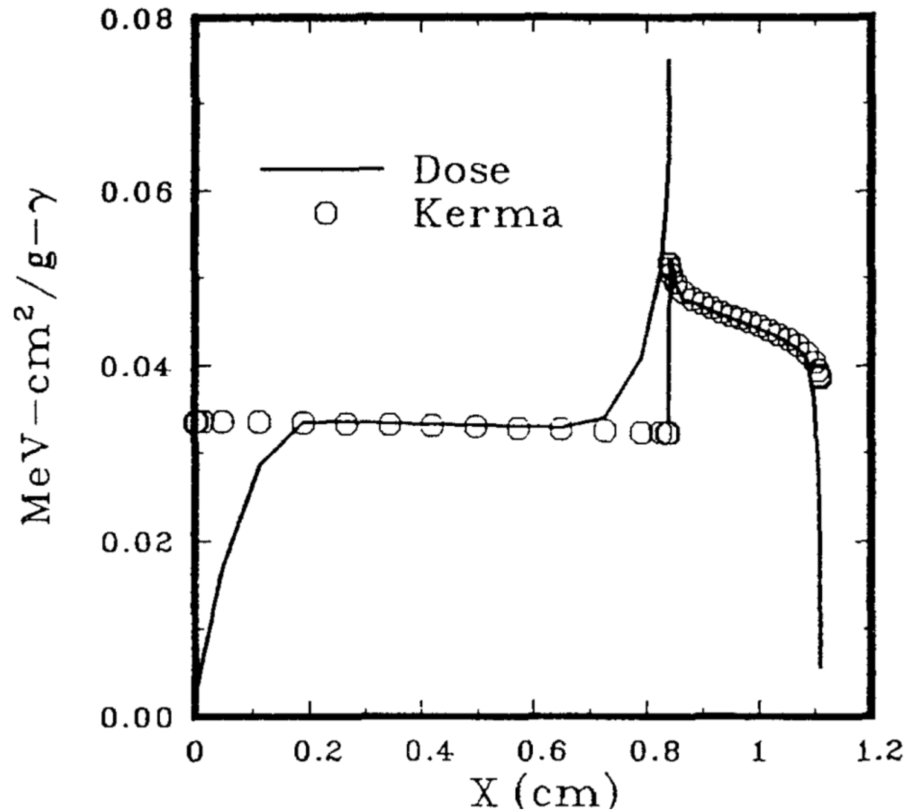

Figure 3.1. Dose and kerma profiles calculated by the CEPXS/ONETRAN simulator for the LiF/Pb case. The fluence is 1 photon/cm^2 [2].

3.3 INTEGRATED TIGER SERIES OF ELECTRON/PHOTON TRANSPORT CODES (TIGERP):

The ITS package helps in getting the Monte-Carlo solution of coupled electron-photon transport problems. The codes provide a time-independent and multi-dimensional solution to the problem. These codes used contain transport as a result of collisions as well as transport under the influence of electric and magnetic fields. The energy ranges from 1 keV ~1 GeV [1]. In version 3.0 of the ITS series, the new process that is taken

into consideration is the coherent scattering of photons. This is in addition to the already existing processes of Compton effect with the production of scattered electrons, pair production, photoelectric absorption and the generation of photoelectrons, Auger and fluorescence photons. Among the different member codes, TIGER is a 1-D code, CYLTRAN is a 2-D code whereas ACCEPT is a 3-D code. The P codes (TIGERP, CYLTRANP etc.) include a very sophisticated model for ionization and processes. The latest version 3.0 has improved models. Also, efforts have been made in order to make the Monte Carlo simulations more efficient. The I/O capability has been improved and also the package has been made more accessible to users.

3.3.1 Modeling based on Physics

There were two primary improvements in as far as the physical model associated with electron energy loss. The Landau straggling distribution was made consistent with the stopping power. Landau's universal function has been extended to higher value of the variable. The cut-off value of this variable is chosen such that the mean energy loss is in accordance with the stopping power. Also, in order improve the simulation of electron transport at low energies and in high-Z materials, the Blunck-Leisegang modification [13] has been added to the Landau distribution.

The Bethe-Heitler-Born approximations of the bremsstrahlung cross sections were replaced [12] by more updated models. These are computed using numerical phase-shift calculations for the screened Coulomb potential below an energy of 2.0 MeV [13] ,[14].

The physical models for photon transport have also been updated. The phenomena of coherent scattering and binding effects have been added in the latest version. Binding effects have also been taken into account for incoherent scattering of photons. This gives a modified energy-angle distribution for the scattered photons.

3.3.2 Variance Reduction Techniques

In order to improve the Monte-Carlo simulations run time, electron histories have been properly and quickly terminated in the TIGERP codes. These modifications have been made based on experience. This has helped to mitigate the problem of over-biasing and also up to 40 % reduction in simulation times have been achieved. Since electron transport is much more efficient than photon transport, there is also an option to fully ignore electron transport for problems where the radiation effects due to electrons are known to be negligible.

Figure 3.2 below shows the pulse height spectrum with a Ge detector. Results show an improvement and better match with experiments for the improved ITS version 3.0 codes over the previous ITS version 2.1 as a result of the improvement in physical models as described in this section.

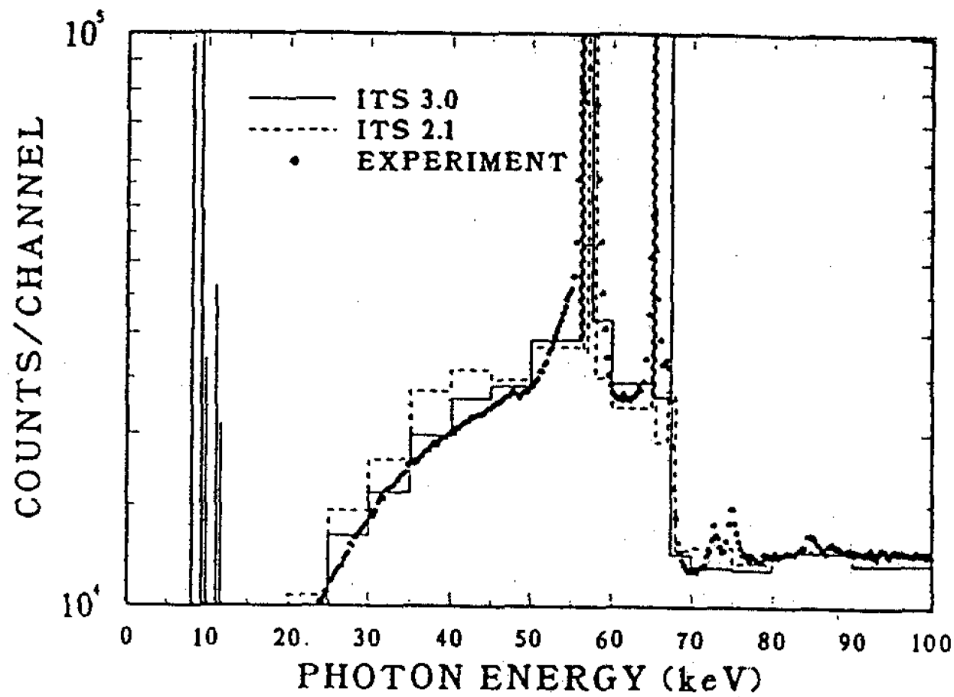

Figure 3.2. Pulse height spectrum with a germanium detector. Results show an improvement and better match with experiments for the improved ITS version 3.0 codes over the previous ITS version 2.1 [1].

3.3.3 I/O improvement:

Improvements have been made to the codes in order to catch an error as soon as possible and hence terminate its propagation thus saving time involving debugging that takes prolonged times. Not only that, a note is made also of the history and batch number of an erroneous Monte-Carlo run. This helps in debugging as only the erroneous history can be re-run instead of the full run to be repeated.

3.4 MRED SIMULATION TOOL

In this section, we describe briefly the physics and engineering concepts behind the simulator used in this work: Monte-Carlo Radiative Energy Deposition tool (MRED) [4-6]. We will also describe the architecture and various components of this simulator and the various Geant4 based physics models that can be used in order to study energy and charge deposition in critical device regions. An extensive discussion of this MRED simulator and its applicability to solving a wide range of science and engineering problems has been reported by Weller et al., in [4], [5], [6].

MRED has been primarily used in the past to study Single Event Effects (SEE) in electronic circuits. In the MRED simulator, it is possible to describe the radiation environment one is interested in studying – photons, heavy ions, neutron spectrum etc. The energy spectrum of the incident ions, their flux and angular distribution can also be described. The various physics models aid in simulating the transport of charge carriers through sensitive device regions such as electronics packaging, chip metallization. We can then study the energy and dose deposition in sensitive volumes of interest in the device. It is also possible to study the collected charge at sensitive nodes by the impinging ions which can cause single event upset (SEU) and hence bit flip in transistor circuits.

3.4.1 Physics Models:

Due to the probabilistic nature of charge particle transport in semiconductor device regions, Monte Carlo based simulations form the basis of the MRED simulator. Depending on the physics of the problem one is concerned with, MRED provides access through its physics lists to physics models from the Geant4 C++ class libraries [15], [16]. It includes models to study a wide range of physics problems – from nuclear effects in ICs due to impinging heavy ions and their fragments to low energy electromagnetic processes such as due to low and medium energy photons. In this work, we have studied the physics of low energy electromagnetic processes due to low energy and medium energy x-ray photons. We have primarily used the physics models – the LowEnergyEM Livermore model from the Geant4 C++ library [15] in this work. MRED 9.0.0 also provides access to the Fortran PENELOPE2008 code [17]. This code is not a part of the Geant4 toolkit. PENELOPE2008 is the current "gold standard" for studying such low energy electromagnetic processes in solids and it tracks secondary electrons down to ~ 50 eV. This is a significant improvement over the earlier simulators we have described before like the ITS TIGERP code [1] and the discrete ordinate CEPXS/ONETRAN codes [2] we have described earlier which gave energy resolution down to ~ 1 keV.

3.5 MRED ARCHITECTURE:

MRED provides a platform for studying single event and other radiation effects in semiconductors. The interaction of radiation with matter and charge particle transport is a built in Monte-Carlo code. This is based on the Geant4 core. The physics models are the same as the Geant4 C++ physics libraries [15], [16]. The incident particles can be launched using a Geant4 ParticleGun class. The particle tracking is done up to a point where the particle is annihilated by reacting with other entities like atoms, ions etc. or until they leave the world. Python is the computer language used in MRED for these interactions.

MRED also provides access to some high-level programs for its functionality such as the tools required to generate histograms and for the data analysis. These are based on AIDA [18]. Also, there is a 2-D plotter XMGRACE [19] and a viewer OPENDX [20]. It is possible to invoke the TCAD device simulator SYNOPSYS [21] and the circuit simulator SPICE in order to study the device response and other circuit effects due to the energy deposition and charge transport at critical nodes.

REFERENCES:

[1] J. A. Halbleib, R. P. Kensek, and G. D. Valdez, “ITS – the integrated TIGER series of electron-photon transport codes – version 3.0,” *IEEE Trans. Nucl. Sci.*, vol. 39, no. 3, pp. 1025-1030, Aug. 1992.

[2] L. J. Lorence, Jr., “CEPXS/ONELD version 2.0: A discrete ordinates code package for general one-dimensional coupled electron-photon transport,” *IEEE Trans. Nucl. Sci.*, vol. 39, no. 3, pp. 1031-1034, Aug. 1992.

[3] L. J. Lorence, Jr. and D. E. Beutler, “Radiation transport phenomena and modeling,” *1997 IEEE NSREC Short Course*, Snowmass, CO.

[4] R. A. Weller, R. A. Reed, K. M. Warren, M. H. Mendenhall, B. D. Sierawski, R. D. Schrimpf, and L. W. Massengill, “Monte-Carlo simulation of single event effects,” *IEEE Trans. Nucl. Sci.*, vol. 57, no. 4, pp. 1726-1745, Aug. 2010.

[5] R. A. Weller, R. A. Reed, K. M. Warren, M. H. Mendenhall, B. D. Sierawski, R. D. Schrimpf, and L. W. Massengill, “General framework for single event effects rate prediction in microelectronics,” *IEEE Trans. Nucl. Sci.*, vol. 56, no. 6, pp. 3098-3108, Dec. 2009.

[6] R. A. Weller, R. A. Reed, K. M. Warren, M. H. Mendenhall, B. D. Sierawski, R. D. Schrimpf, and L. W. Massengill, “Monte-Carlo simulation of single event effects,” *RADECS Short Course*, Aug. 2010.

[7] J. J. Duderstadt and W. R. Martin, Transport Theory, Wiley-Interscience, New York, 1979.

[8] G. I. Bell and S. G. Glasstone, Nuclear Reactor Theory, Van Nostrand Reinhold, New York, 1970.

[9] L. J. Lorence, Jr. W. E. Nelson, and J. E. Morel, IEEE Trans. on Nucl. Sci., 32, 4416, 1985.

[10] W. L. Fillipone, S. Woolf, and J. C. Garth, IEEE Trans. Nucl. Sci. 34, 1564, 1987.

[11] J. C. Garth, E. A. Burke, and S. Woolf, IEEE Trans. Nucl. Sci.,32, 438, 1986.

[12] S. M. Seltzer, "Electron-Photon Monte Carlo Calculations: The ETRAN Code," *Appl. Radiat. And Isot.,* vol. 42, No. 10, pp. 917, 1991.

[13] M. J. Berger and S. M. Seltzer, "Bremsstrahlung and Photoneutrons from Thick Tungsten and Tantalum Targets," *Phys. Rev. C,* vol. 2, pp. 621, August 1970.

[14] S. M. Seltzer and M. J. Berger, "Bremsstrahlung Spectra from Electron Interactions with Screened Atomic Nuclei and Orbital Electrons," *Nucl. Instr. Meth.,* vol. B12, 95, 1985.

[15] S. Agostinelli et al., "Geant4—A simulation toolkit," Nucl. Inst. Meth. Phys. Res. A—Accelerators, Spectrometers, Detectors and Associated Equipment, vol. 506, no. 3, pp. 250–303, 2003.

[16] J. Allison *et al.*, "Geant4 developments and applications," *IEEE Trans. Nucl. Sci.*, vol. 53, no. 1, pp. 270–278, Feb. 2006.

[17] A. F. Bielajew and F. Salvat, "Improved electron transport mechanics in the PENELOPE Monte-Carlo model," *Nucl. Instrum. Meth. Phys. Res. B*, vol. 173, no. 3, pp. 332-343, Jan. 2001.

[18] V. V. Serbo, "Status of AIDA and JAS 3," *Nucl. Inst. Meth. Phys. Res. A*, vol. 502, pp. 663–665, 2003.

[19] http://plasma-gate.weizmann.ac.il/Grace

[20] http://www.opendx.org

[21] SYNOPSYS, Documentation on SYNOPSYS TCAD Tools.

CHAPTER IV

ENHANCEMENT IN DEPOSITED ENERGY/DOSE IN SiO_2 BASED MOS AND REDUCTION IN HIGH-K MOS DEVICES

4.1 INTRODUCTION

In modern MOS technologies, high-κ materials are increasingly used in gate dielectric layers and chip metallization. High-κ materials in metallization [1] and packaging [2] can lead to significant dose enhancement in low and medium-energy x-ray environments. Enhancement factors of up to 10 or more associated with high-Z materials have been observed in medium-energy x-ray environments [1]-[8]. However, the effects of high-Z materials in the gate dielectric (e.g., Hf) have not been evaluated quantitatively. Comparative experimental studies of MOS devices with high-κ and SiO_2 dielectrics are limited in applicability because defect densities are typically much different in HfO_2 and SiO_2 [9],[10]. So it is not known whether differences in reported device responses in previous studies are due primarily to differences in dose, differences in defect densities, differences in effective electron-hole recombination rates, etc.

In this chapter, we compute x-ray doses in SiO_2 and HfO_2 dielectrics using the Monte-Carlo Radiative Energy Deposition (MRED) simulator at Vanderbilt University [11],[12].

In past studies, MRED has been used primarily in studies of single event effects (SEE) [11],[13]-[16] and displacement damage [12],[17]. Particle interactions with high-Z materials can be quite significant in determining error rates in space, especially for radiation-hardened technologies [11],[13],[14],[16]. Here we first compare MRED calculations of total ionizing dose (TID) for 10-keV x-ray irradiation, and then for a 400-keV endpoint-energy bremsstrahlung x-ray spectrum. We calculate the dose enhancement in SiO_2 that is caused by high-Z materials that are nearby the gate dielectric layer, and on the reduction in dose that can occur when a high-Z dielectric layer is surrounded by lower-Z materials. We compare these calculations to previous results in the literature obtained with other Monte Carlo and discrete ordinates codes and previous experiments [1],[3], and find generally good agreement. These results provide insight into comparisons of the radiation response of MOS devices with SiO_2 and HfO_2 gate dielectrics, and demonstrate the capability of MRED to assist in the evaluation of dose in complex microelectronic materials and devices.

4.2 MRED SIMULATION DETAILS

Structures:

Schematic diagrams of MOS capacitors having three different geometries are shown in Fig. 4.1. These include capacitors with (1) a pure Al gate, (2) an Al gate with a $TaSi_2$ layer that is 200 nm from the gate oxide, and (3) an Al gate with a $TaSi_2$ layer that is 670 nm from the gate oxide. The physical thickness of the gate oxide used in our calculations varies from very thick (1000 nm) to ultra-thin (~1 nm), and comparisons are made to physical capacitor structures with oxide thicknesses ranging from 1000 nm to 35 nm [3].

The thicker oxides are useful for estimating equilibrium doses in the dielectric layers. The ultra-thin gate dielectrics are more relevant for comparison to results for present and future generations of MOS technologies. These devices have been used in previous work using 10-keV x-rays in [3], and a medium-energy x-ray spectrum in [16].

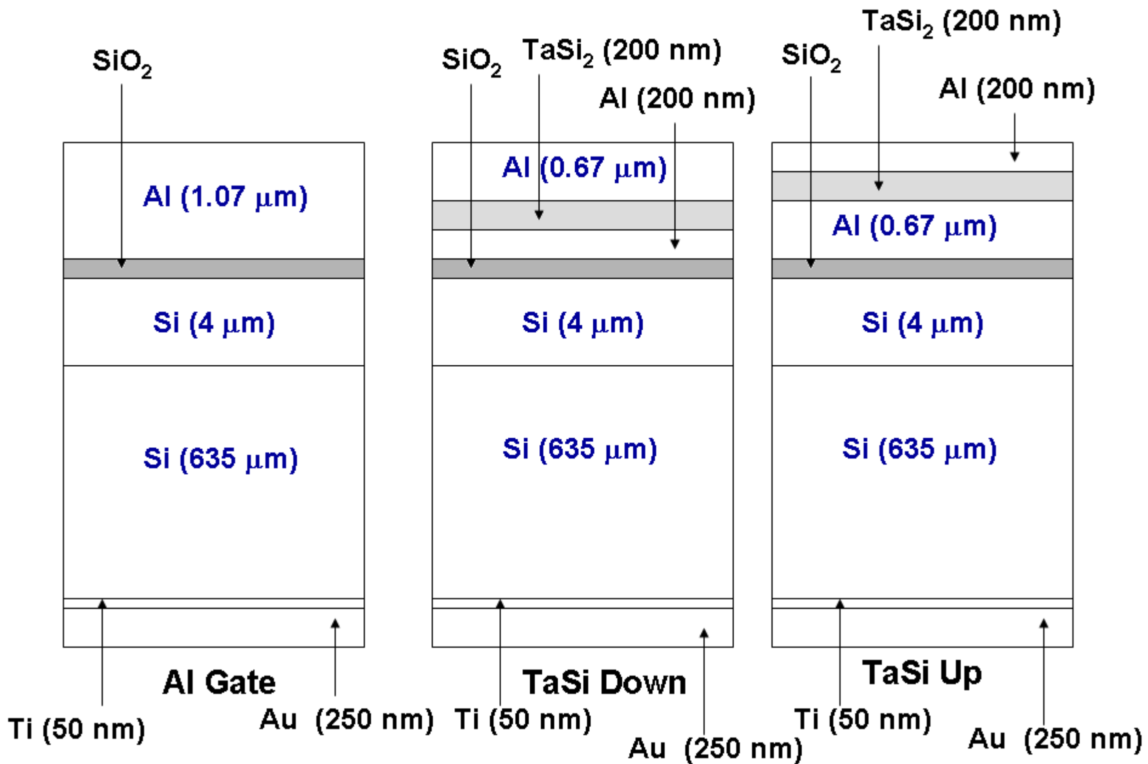

Figure 4.1. Device geometries for Al-gate, $TaSi_2$-down, and $TaSi_2$-up MOS capacitors (after [1]). Secondary electrons emitted from the $TaSi_2$-up layer are attenuated more by the thicker Al layer than are the electrons emitted from the $TaSi_2$-down layer, which is 470 nm closer to the gate oxide. For the HfO_2 calculations performed, the SiO_2 layer (dark grey) was simply replaced by HfO_2 [18].

4.2.1 Simulations

Each structure in Figure 4.1 was simulated in MRED to study numerically the total dose (energy per unit mass) deposited by 10-keV x-rays and/or a 400-keV energy (105 keV

average energy) bremsstrahlung x-ray spectrum in the gate oxide of the MOS capacitor. In this work we used MRED version 9.0.0 based on Geant4 9.3. The current implementation of low energy electromagnetic processes in the Geant4 toolkit [17],[19] is valid for energies down to 250 eV and can be used up to approximately 100 GeV. In addition to performing these calculations for the SiO_2-based structures depicted in Figure 4.1, we performed similar calculations for the three metal gate stacks with HfO_2 as the gate dielectric layer.

As part of this study, we compared the current standard version of MRED with the Geant4 low energy electromagnetic physics models for electron transport with a new version that incorporates the electron transport code PENELOPE 2008 (PENetration and Energy LOss of Positrons and Electrons) [20]. This PENELOPE module is not part of the Geant4 toolkit [17],[19], but is expected to provide reliable results for electron energies down to ~ 50 eV, and can be used up to ~1 GeV [20]. We found similar results (differences in calculations that typically are less than device-to-device response variations observed in experimental work using the devices of Figure 13 [1],[16]) using each of these separate approaches to electron transport. Hence, either module can provide reliable descriptions of the dose that is deposited in these kinds of structures, which are typical of gate dielectrics in MOS devices and ICs. In the remaining calculations, we show the averages of the values obtained from the Geant4 low energy electromagnetic physics models and the PENELOPE code.

4.3 SiO_2 MOS CAPACITORS: 10-KEV X-RAYS

In Figure 4.2, the energy deposition profile in the SiO_2 gate oxide for the three MOS capacitor geometries of Figure 4.1, for a 98 nm SiO_2 gate oxide is shown. The total energy deposited in the gate oxide is obtained by integrating these curves. In all cases, the energy deposited in the SiO_2 gate oxide in the capacitor structures of Figure 13 is higher than that deposited in the pure SiO_2. This is due to dose enhancement caused by the surrounding higher-Z materials, with the largest enhancement occurring in the $TaSi_2$-down geometry [3].

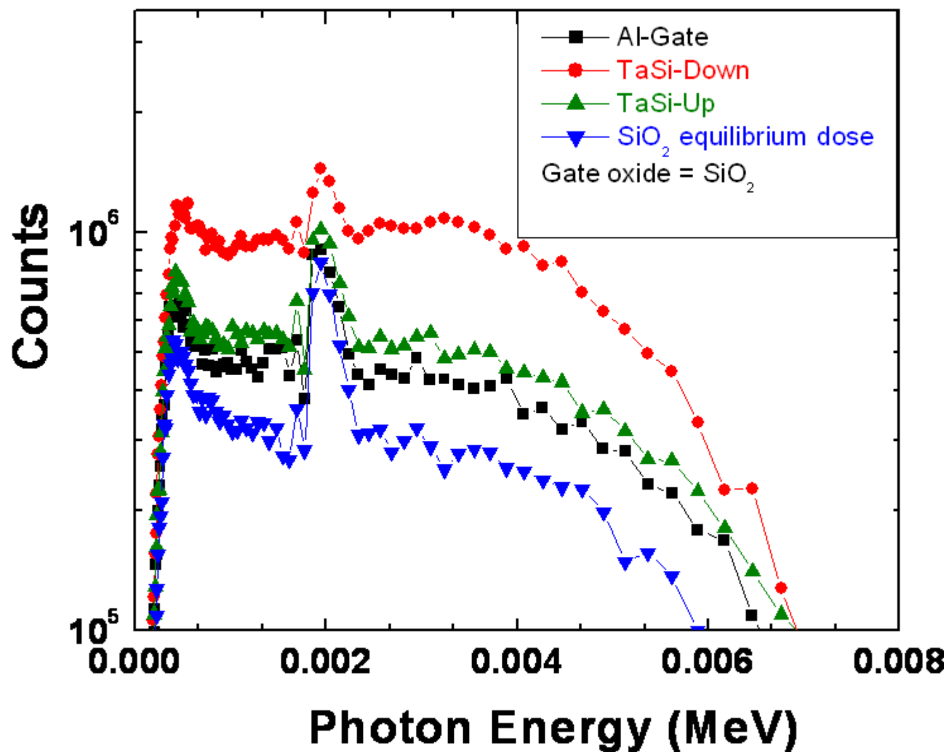

Figure 4.2. Simulated 10-keV x-ray energy deposition profile for 98 nm SiO_2 Al-gate, $TaSi_2$-down, and $TaSi_2$-up MOS capacitors. The energy deposition profile is shown for comparison for a pure SiO_2 layer of the same physical thickness as the multilayer capacitor structures [18].

Figure 4.3 shows the dose in the SiO_2 gate oxide for the MOS capacitors of Figure 4.1, relative to the equilibrium dose in SiO_2, as a function of gate oxide thickness. This ratio is an effective measure of the dose enhancement factor (DEF). The doses increase monotonically with decreasing gate oxide thickness for all three geometries and converge for the thickest (~1060 nm) oxide.

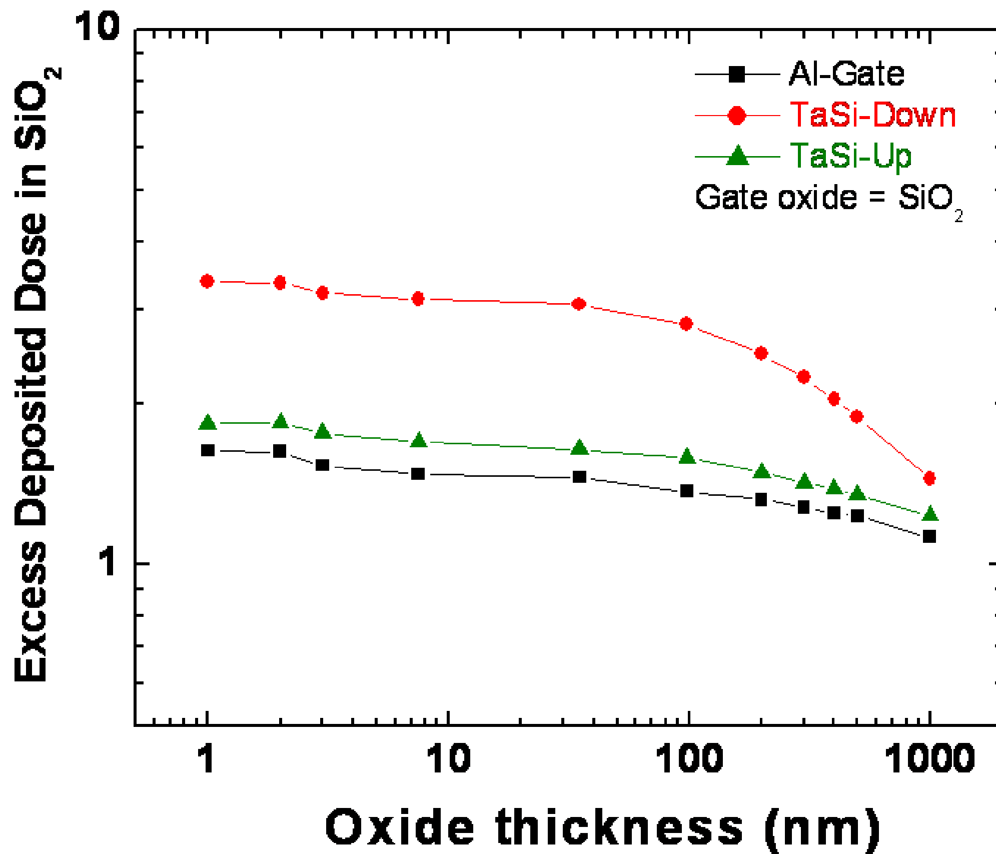

Figure 4.3. Enhanced dose due to 10-keV x-rays for the MOS capacitor structures of Figure 4.1 as a function of SiO_2 dielectric layer thickness [18].

Figure 4.4 compares the dose enhancement factors computed using MRED for Al-gate MOS capacitors with SiO_2 gate dielectrics for four different gate oxide thicknesses, compared with results obtained previously with other radiation transport codes [3]. These

include the Monte Carlo simulator TIGERP [3],[21],[22] and discrete ordinates codes CEPXS/ONETRAN and TEP [23],[24]. TIGERP results tend to be higher than those of the other transport codes for thin oxides, and lower than the other codes for the thickest oxides. Otherwise, the predicted DEFs are similar for all of the transport codes.

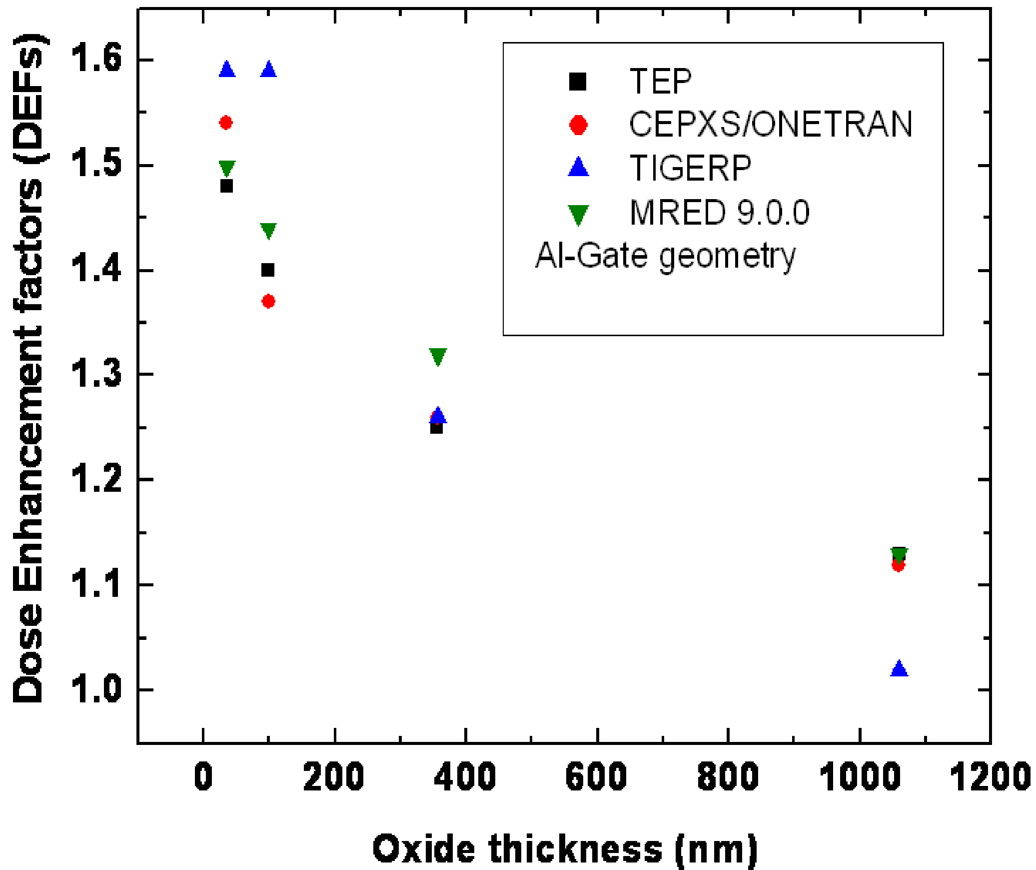

Figure 4.4. Comparison of MRED calculations with TIGERP, TEP, CEPXS/ONETRAN simulators (results from [3]) for the Al-gate SiO_2 MOS capacitors of Fig. 4.1. The DEFs were computed for 10-keV x-rays [18].

Figure 4.5 compares the dose enhancement factors computed using MRED for TaSi-Up-gate MOS capacitors with SiO_2 gate dielectrics for four different gate oxide thicknesses. As discussed, the TaSi-Up gate is characterized by the presence of high-Z TaSi layer in the gate metallization separated by 670 nm of Al in-between. Here we observe that the

Monte-Carlo code TIGERP DEF values are much closer to the values calculated by MRED 9.0.0. This is in contrast to the Al-gate geometry case where the TIGERP DEF values were higher than MRED 9.0.0 DEF values for thin oxides which are to technological interest. The discrete ordinate codes TEP and CEPXS/ONETRAN predict consistently higher dose enhancement factor values for all the different TaSi-Up geometries of varying oxide thickness.

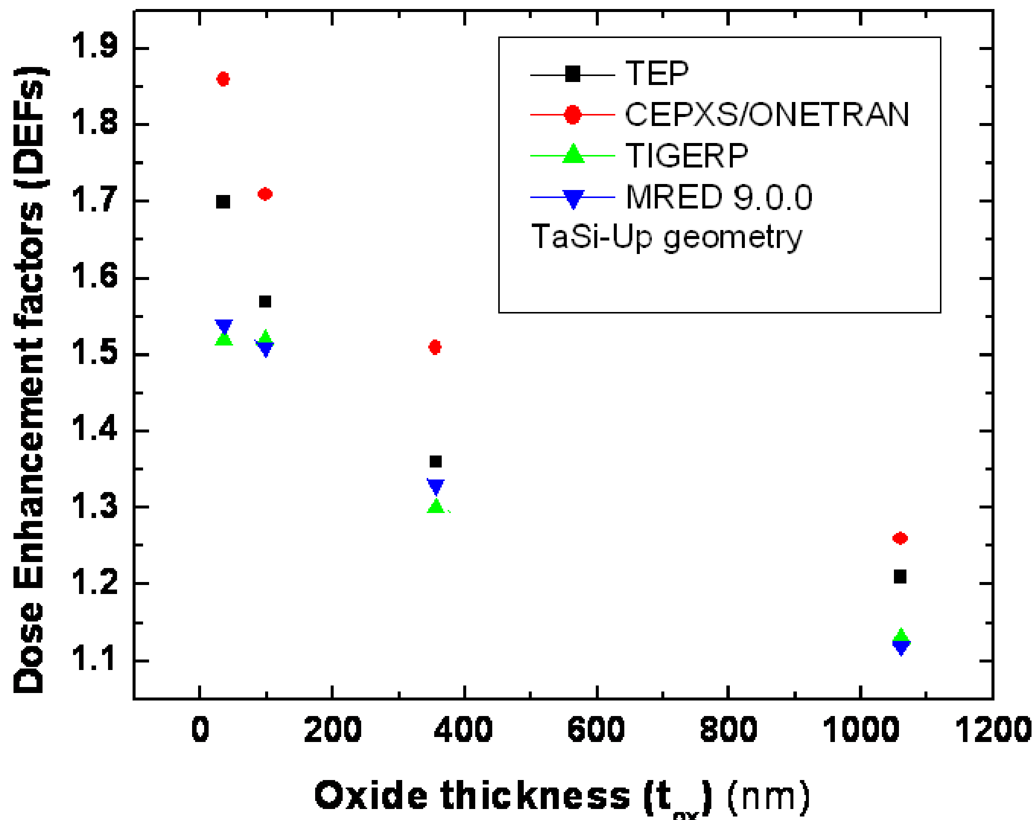

Figure 4.5. Comparison of MRED calculations with TIGERP, TEP, CEPXS/ONETRAN simulators (results from [3]) for the TaSi-Up gate SiO_2 MOS capacitors of Figure 4.1. The DEFs were computed for 10-keV x-rays.

Figure 4.6 compares the dose enhancement factors computed using MRED for TaSi-Down gate MOS capacitors with SiO_2 gate dielectrics for four different gate oxide thicknesses, compared with results obtained previously with other radiation transport

codes [3]. As discussed, the TaSi-Down gate is characterized by the presence of high-Z TaSi layer in the gate metallization separated by 200 nm of Al in-between. Here we observe that the Monte-Carlo MRED 9.0.0 code predicts higher DEF values for thin oxides compared to the TIGERP, TEP and CEPXS/ONETRAN. TIGERP predicts the least DEF values.

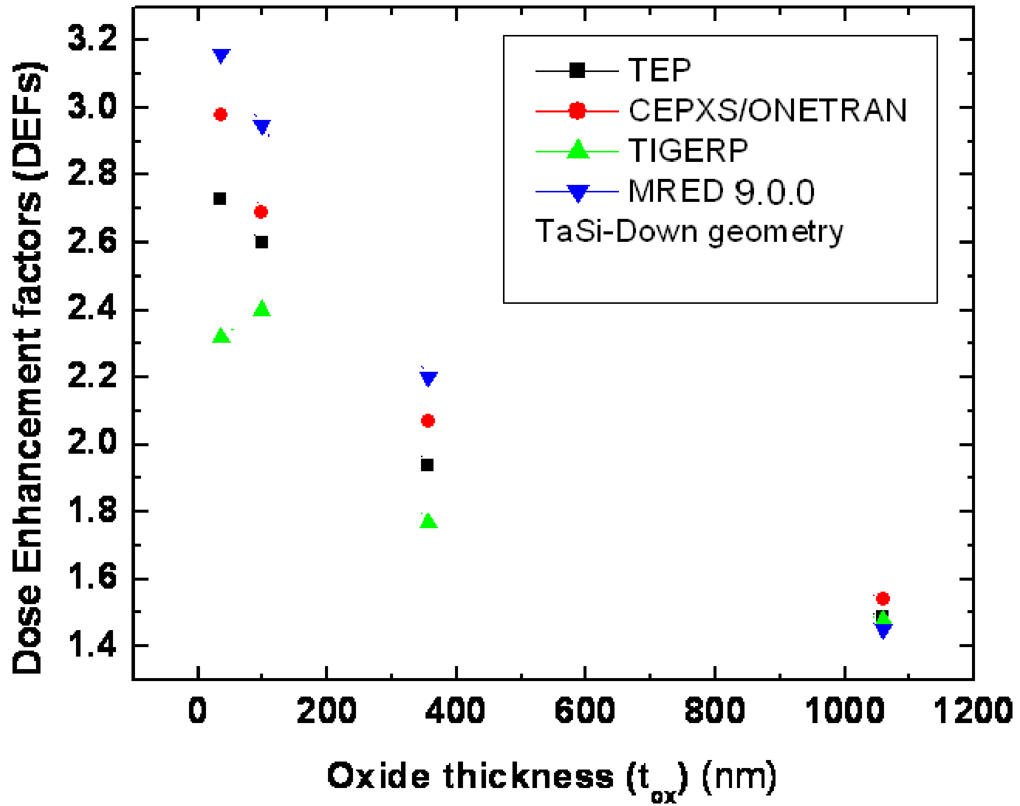

Figure 4.6. Comparison of MRED calculations with TIGERP, TEP, CEPXS/ONETRAN simulators (results from [3]) for the TaSi-Down gate SiO_2 MOS capacitors of Figure 4.1. The DEFs were computed for 10-keV x-rays.

Table 4.1 shows MRED calculations for the structures of Figure 13, as well as thinner simulated oxide layers. The MRED calculation of the DEF for the very thin oxides (1-3 nm) is similar to the TIGERP calculation for 35-98 nm oxides. Figure 4.7 graphically

shows MRED calculations of the ratio between the calculated DEFs for capacitors with 35 nm oxides and the DEFs for capacitors with 1060 nm oxides. These are compared with the experimentally measured ratios of hole trapping reported in [1] for capacitors with oxides of these two thicknesses. This ratio is a convenient figure of merit that eliminates factors such as electron-hole recombination [1], or x-ray to Co-60 correlation [25], from the comparison of interest.

For Al-gate structures, Table 4.1 shows that MRED provides a better match to the experimental results than TIGERP or CEPXS/ONETRAN. For the $TaSi_2$-up structures, the CEPXS/ONETRAN simulator is closest to the experimental ratio, closely followed by MRED and TEP. For the $TaSi_2$-down structures, MRED provides an excellent match to the experimental ratios. In all cases, the calculations of MRED are consistent with the experimental results, to within the device to device variations of ~ ± 15%. The differences among the simulation results are primarily a result of the enhanced computational capabilities and updated physical models that are available now, as compared to 1988. Moreover, MRED includes a more comprehensive suite of scattering processes and updated cross sections, as compared to TIGERP, TEP, and CEPXS/ONETRAN.

Table 4.1. Calculated DEFs using MRED 9.0.0 (green)[32], TEP, TIGERP, and CEPXS/ONETRAN [1]. The experimental ratios compare the predicted and experimentally observed ratios between the DEFs and relative device responses observed in [1].

Dose Enhancement Factor			Oxide thickness (nm)					Predicted	Experiment
	1	3	7.5	35	98	356	1060	DEF(35)	DEF(35)
								DEF(1060)	DEF(1060)
Al-Gate									
TEP				1.48	1.4	1.25	1.13	**1.31**	
CEPXS/ONETRAN				1.54	1.37	1.26	1.12	**1.38**	
TIGERP				1.59	1.59	1.26	1.02	**1.56**	
MRED 9.0.0	**1.63**	**1.53**	**1.47**	**1.44**	**1.36**	**1.25**	**1.12**	**1.28**	**1.18**
TaSi-Down									
TEP				2.73	2.6	1.94	1.49	**1.83**	
CEPXS/ONETRAN				2.98	2.69	2.07	1.54	**1.94**	
TIGERP				2.32	2.4	1.77	1.48	**1.56**	
MRED 9.0.0	**3.38**	**3.2**	**3.13**	**3.06**	**2.8**	**2.13**	**1.44**	**2.12**	**2.15**
TaSi-Up									
TEP				1.7	1.57	1.36	1.21	**1.4**	
CEPXS/ONETRAN				1.86	1.71	1.51	1.26	**1.48**	
TIGERP				1.52	1.52	1.3	1.13	**1.35**	
MRED 9.0.0	**1.84**	**1.83**	**1.69**	**1.7**	**1.58**	**1.3**	**1.22**	**1.39**	**1.58**

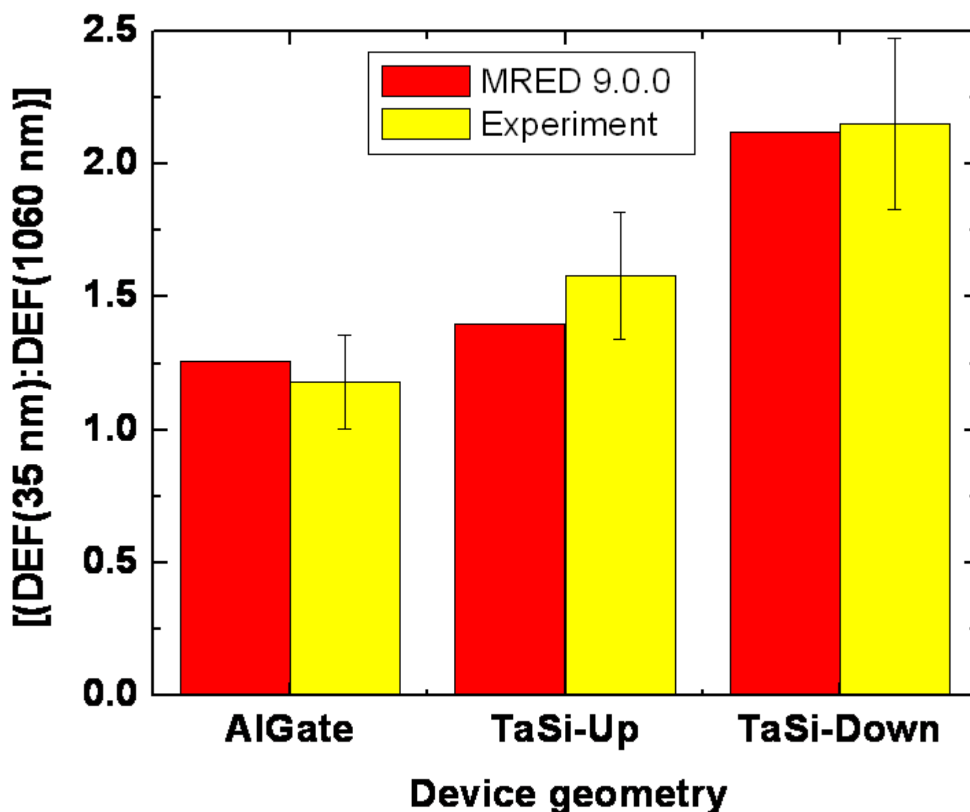

Figure 4.7. MRED calculations of the ratios of the DEFs due to 10-keV x-rays for capacitors with 35 nm oxides to the DEFs of capacitors with 1060 nm oxides. These are compared with the experimentally measured ratios of hole trapping reported in [3] for capacitors with oxides of these two thicknesses [18].

4.4 HFO_2 MOS CAPACITORS: 10-KEV X-RAYS

Since MRED has been shown to reliably predict energy, dose, and charge deposition in SiO_2 based MOS devices, we used MRED to evaluate the effects of replacing the SiO_2 gate dielectric in Figure 4.1 with a high-k dielectric, HfO_2, which is of intense interest for present and future generations of MOS devices [26],[27]. Figure 4.8 compares the deposited energy for HfO_2 and SiO_2 MOS capacitors with Al gates as a function of the physical thickness of the gate oxide. Again, each result is the average of the (quite

similar) results from the low energy electromagnetic physics model contained in the Geant4 toolkit [17],[19] and the PENELOPE code [20]. Because of its higher effective Z, the energy deposited in the HfO_2 gate-dielectric MOS capacitors is significantly higher than that deposited in the SiO_2 capacitors, with a larger difference in energy for thicker oxides than for thinner oxides.

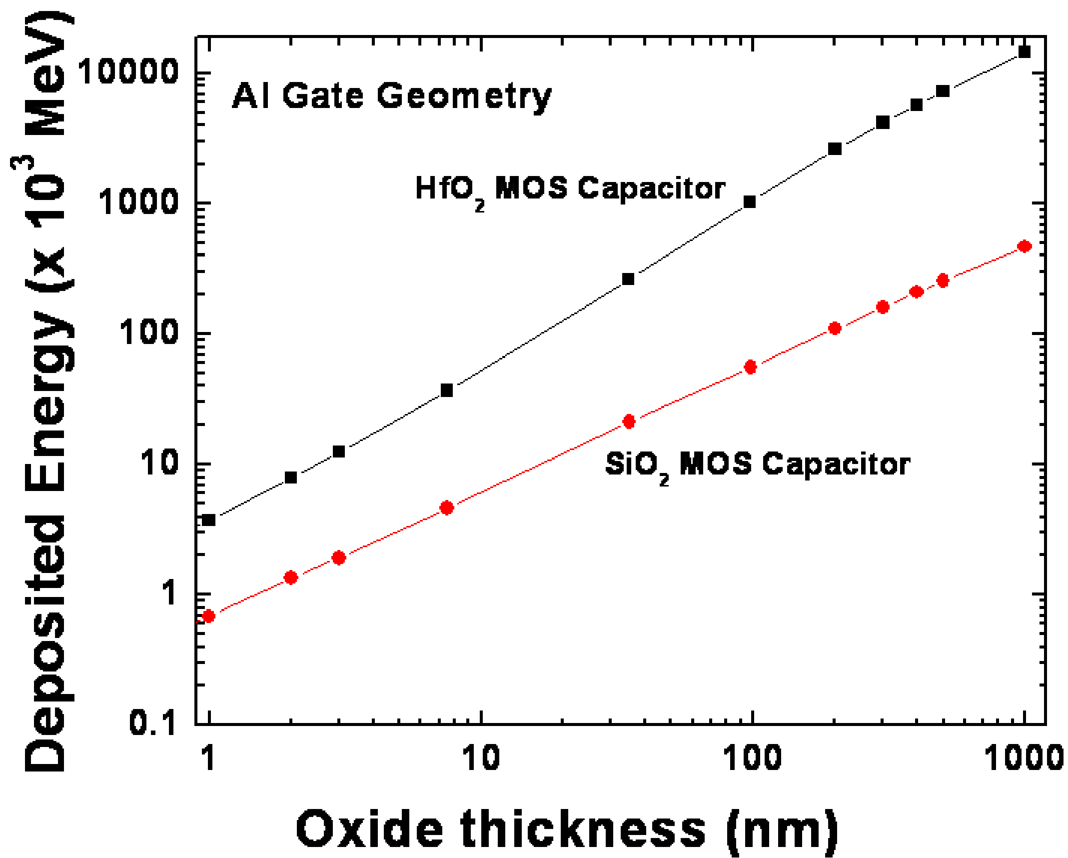

Figure 4.8. Deposited energy due to 10-keV x-rays in the gate dielectric for MOS capacitors with HfO_2 and SiO_2 gate insulators as a function of physical gate oxide thickness, for the Al gate structures of Fig. 4.1 [18].

Figure 4.9 shows the calculated doses in the SiO_2 and HfO_2 dielectric layers for the structures of Figure 4.1. For thicker oxides, the higher-Z of the HfO_2 layer leads to a much larger equilibrium dose than that deposited in the SiO_2. For thinner dielectric layers, the dose is enhanced in the SiO_2 layers because Si and Al are higher Z materials

than SiO_2, and the dose is reduced in the HfO_2, because these surrounding layers are now comparatively the lower-Z materials. The dose reduction in HfO_2 [26] is essentially the inverse of the dose enhancement effect in SiO_2 that is observed when it is surrounded by higher-Z materials [3],[28]-[30].

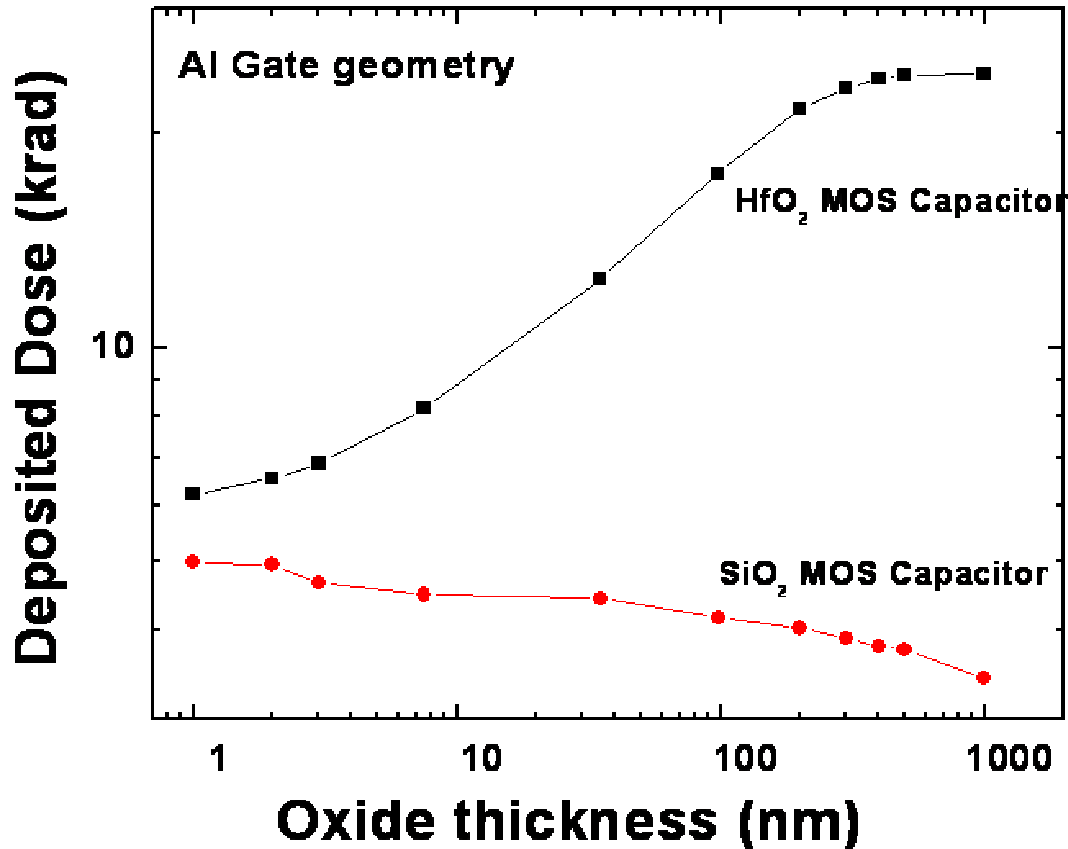

Figure 4.9. Dose (in krad(HfO_2) and krad(SiO_2)) due to 10-keV x-rays in the gate oxides of MOS capacitors with HfO_2 and SiO_2 gate insulators as a function of physical gate oxide thickness, for the Al gate structures of Fig. 4.1 [18].

Figure 4.10 shows the ratio of the calculated dose in HfO_2 to the equilibrium dose in a thick SiO_2 gate dielectric, for the capacitor structures of Figure 4.1. We choose this layer structure and comparison because equilibrium dose in SiO_2 is frequently used to report x-ray dose in studies of the radiation response of high-k gate dielectrics [26],[27]. The

decrease in "excess dose" in the HfO_2 for thinner dielectric layers occurs because much of the energy initially deposited in this higher-Z layer transports (via secondary electrons) to surrounding lower-Z materials. For HfO_2 layer thicknesses of technological interest (2 to 4 nm), these calculations suggest that the dose in the gate dielectric after electron transport is ~ 2-3 times higher than the equilibrium dose in SiO_2 reported in the literature [26],[27]. The higher values occur when higher-Z materials are present in the gate stack, which is of significance to advanced MOS technologies that increasingly incorporate high-κ dielectrics and metal gates [31],[32].

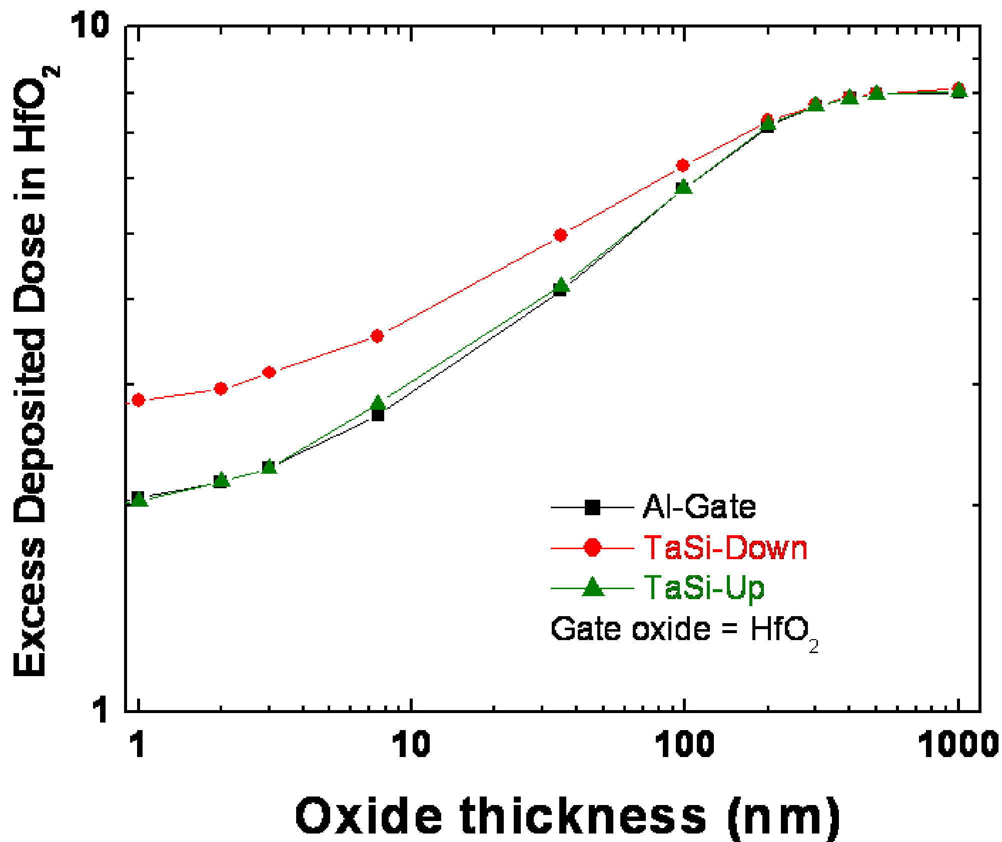

Figure 4.10. Excess dose deposited in HfO_2 MOS capacitor structures compared to the equilibrium deposited dose in a pure SiO_2 structure due to 10-keV x-rays. The dose reduction in the gate dielectric observed for thin HfO_2 layers is significantly greater when the dielectric is surrounded by lower-Z materials than when surrounded by higher-Z materials [18].

To check the calculations in Figure 4.10, we have compared the computations of the equilibrium doses in HfO_2 and SiO_2 to analytical values obtained from the literature. The effective Z, Z_{eff}, can be obtained for SiO_2 and HfO_2 using the empirical relation [18]:

$$Z_{eff} = \sqrt[2.94]{\sum_i f_i (Z_i)^{2.94}} \quad , \qquad (1)$$

where f_i is the fraction of the total number of electrons associated with each element, and Z_i is the atomic number of an element in a compound. From Eq. (1), the value of Z_{eff} for SiO_2 is ~11 (Na) and Z_{eff} for HfO_2 is ~67 (Ho). The equilibrium dose deposited in a material varies as (μ_{en}/ρ). From NIST reference data for Na and Ho [28], as shown in Fig. 4.11, the ratio (μ_{en}/ρ) ~ 4 for HfO_2, relative to SiO_2. There should be no absorption edges for SiO_2 and HfO_2 as has been erroneously shown in Fig. 9 of [18]. This error has been corrected in Fig. 4.11 below. After adjusting this ratio for the relative densities of HfO_2, SiO_2, Ho, and Na (Eq. (2)), the calculated ratio is ~ 8, consistent with that shown for the thicker oxides in Figure 4.10, and affirming the MRED calculations.

$$Dose - Ratio = \left(\frac{\left(\frac{\mu_{en}}{\rho}\right)_{Holmium} \cdot (\rho)_{Holmium} \cdot \left(\frac{1}{\rho}\right)_{HfO_2}}{\left(\frac{\mu_{en}}{\rho}\right)_{Sodium} \cdot (\rho)_{Sodium} \cdot \left(\frac{1}{\rho}\right)_{SiO_2}} \right) \qquad (2)$$

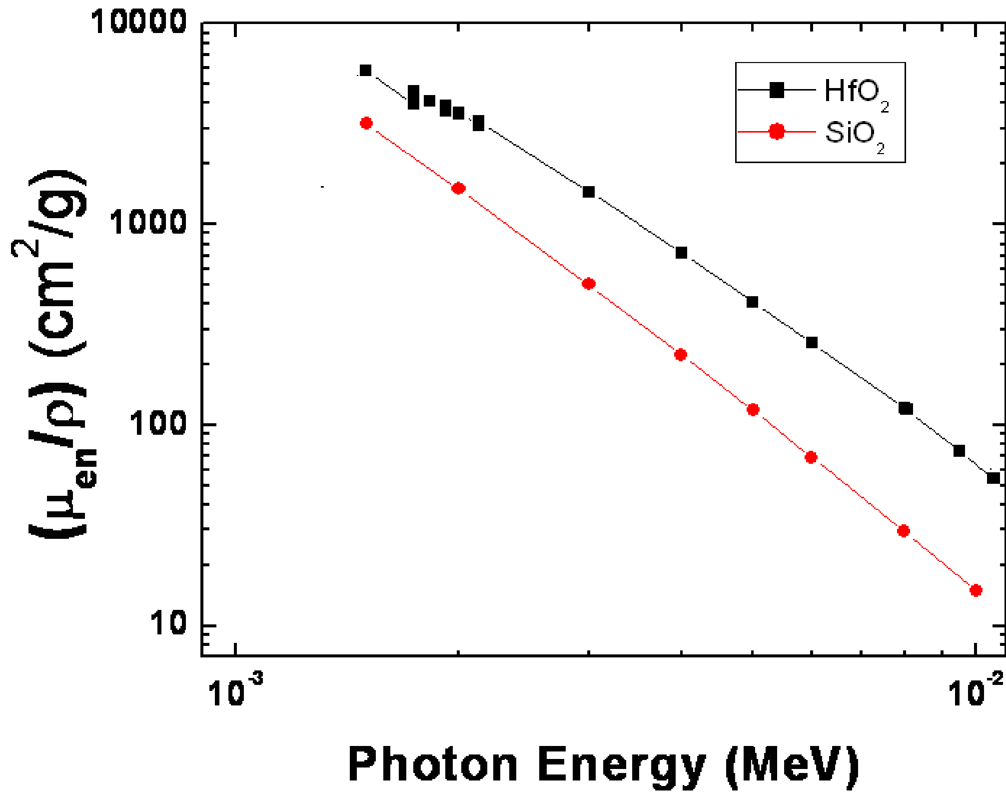

Figure 4.11. Ratios of (μ_{en}/ρ) values for HfO_2 (Z_{eff} ~ 67) and SiO_2 (Z_{eff} ~11) as a function of photon energy. For 10-keV x-rays, the ratio is ~ 4.

4.5 MEDIUM-ENERGY X-RAYS

We next consider how the structures in Figure 4.1 respond to medium energy x-rays [16]. For the MRED calculations, we simulated the photon spectrum generated by the Sandia Pelletron, a variable energy electron accelerator, with an x-ray converter attached to it. The x-ray converter used consisted of 89 µm Ta followed by 4.8 mm C [16]. An electron beam energy of 400 keV was used to produce a bremsstrahlung x-ray spectrum with an average energy of 105 keV, as illustrated in Figure 4.12. For optimal calibration, the background corresponding to the Ge detector output for white light was subtracted to

obtain the simulated spectrum. The resulting computed spectrum is quite similar to that shown and validated for capacitors with SiO_2 dielectrics in [16]. Below ~80 keV, the spectrum exhibits sharp peaks corresponding to the characteristic lines of the Ta used in the x-ray converter. There is a broad continuum above 80 keV.

Fig. 4.13 shows the MRED calculations of the deposited energy for the medium-energy x-ray spectrum of Figure 24 for HfO_2 and SiO_2 MOS capacitors with Al gates, as a function of gate oxide thickness. The energy deposited in the HfO_2 for these capacitors is significantly higher than that in the SiO_2 capacitors, due to the higher-Z of the HfO_2 layer. Importantly, one does not see a significant reduction in the ratios of the deposited energy in the HfO_2 layers with decreasing thickness like that shown in Figures 4.9 and 4.10.

Figure 4.14 shows the dose in the SiO_2 and HfO_2 dielectric layers for the medium-energy x-ray spectrum of Figure 4.12 for all three capacitor structures of Figure 4.1. Much higher doses are deposited in the HfO_2 MOS capacitors as compared to the SiO_2 MOS capacitors for the entire range of oxide thicknesses. The dose deposited in the thickest HfO_2 capacitor is ~10 times that for the thickest SiO_2 layer capacitor. This increase in dose is maintained for thinner oxides, showing that advanced MOS devices with high-κ gate dielectrics will exhibit much higher doses (and potentially higher photocurrents as well) in their gate oxides in medium-energy x-ray environments than will devices with SiO_2 gate dielectrics. This will need to be factored into hardness assurance test plans for such devices, if used in medium energy x-ray environments [16],[30].

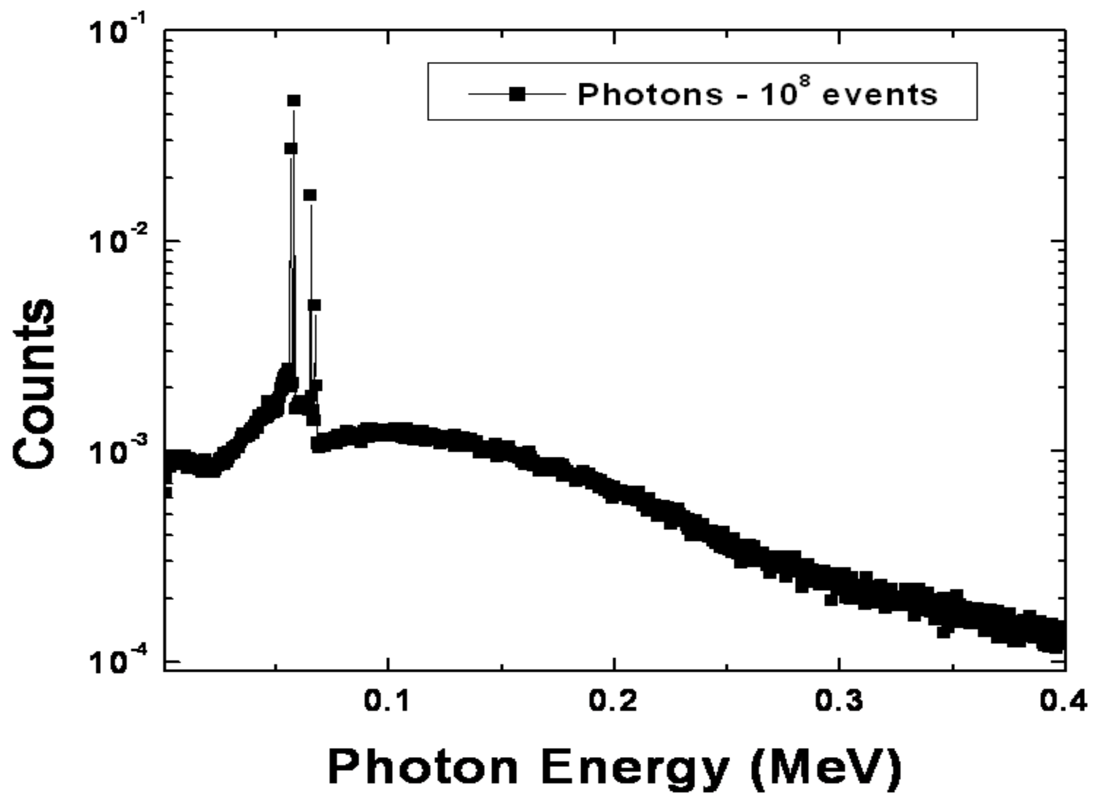

Figure 4.12. 400-keV endpoint-energy bremsstrahlung x-ray spectrum (average energy 105 keV) from the Sandia Pelletron, as simulated by MRED, for the conditions of [16], [18].

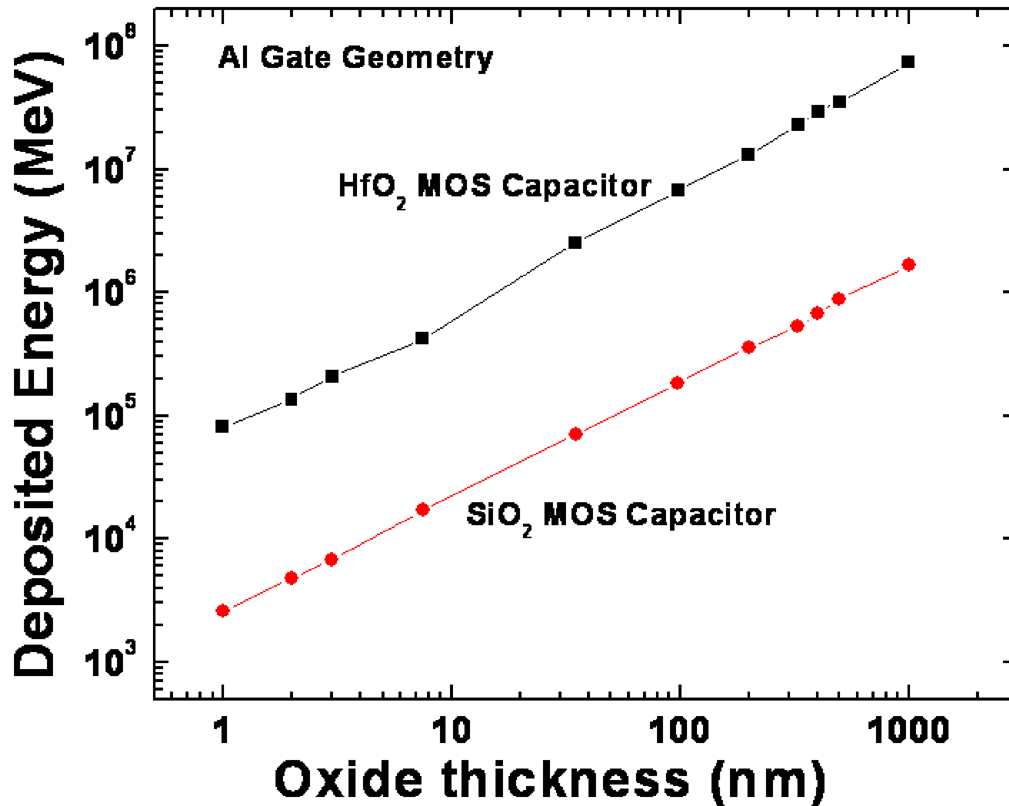

Figure 4.13. Deposited energy in the gate dielectric for HfO_2 and SiO_2 Al-gate MOS capacitors as a function of gate oxide physical thickness for the 400-keV endpoint-energy bremsstrahlung x-ray spectrum of Figure 4.12 [18].

Again to compare with previous work, where possible, we note that the doses in the $TaSi_2$-down capacitors with SiO_2 dielectric layers in Figure 4.14 are ~1.9-2.3 times higher than the doses in the Al-gate capacitors. The measured ratios for the comparable experimental device responses in [16] are ~1.9-2.1. These experiments were done on similar Al-gate and $TaSi_2$-gate geometry capacitors at 300 K, using the Sandia Pelletron source to generate a 400-keV endpoint-energy bremsstrahlung x-ray spectrum [16]. The MRED calculations for SiO_2 also match well the DEFs of ~2.0-2.3 as predicted by the ITS coupled electron/photon transport codes in [16].

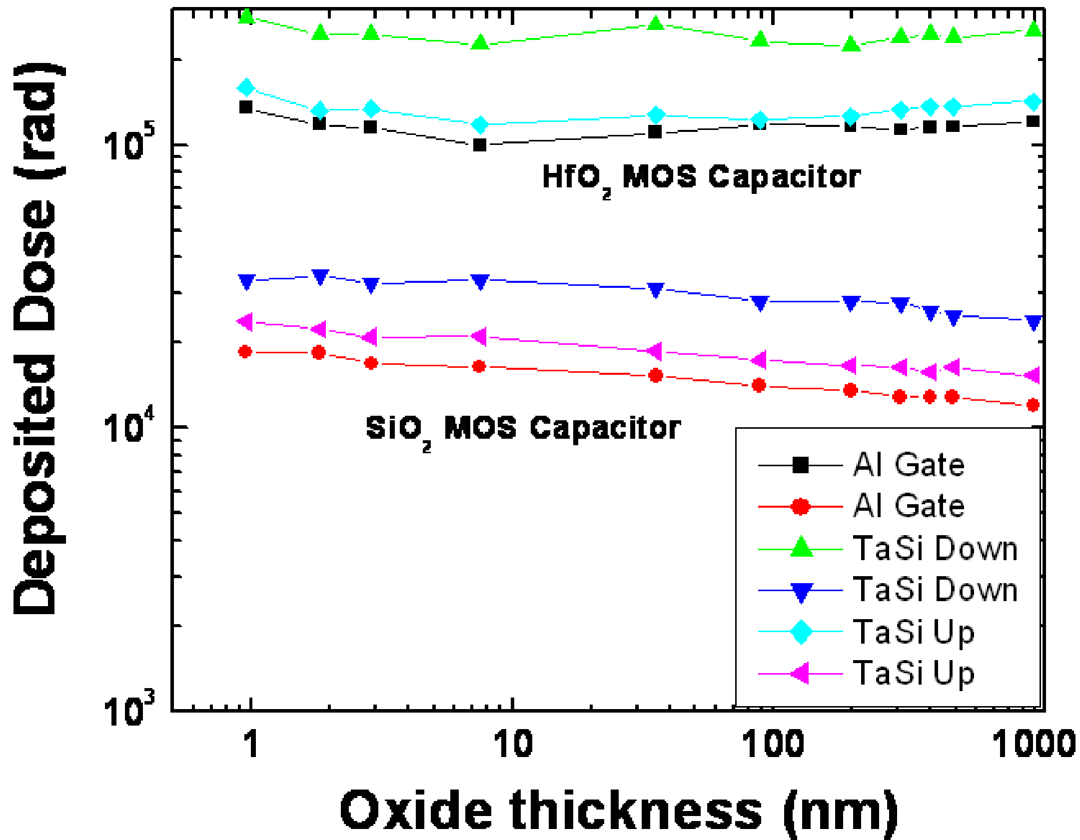

Figure 4.14. Dose (in rad(SiO_2) and rad(HfO_2)) as a function of physical oxide thickness for HfO_2 and SiO_2 gate dielectric layers for the MOS capacitor structures of Figure 13, for the 400-keV endpoint-energy bremsstrahlung x-ray spectrum of Figure 4.12 [18].

The results strongly suggest that MRED computations of dose can be used to help predict the radiation response of dielectric layers that are located in proximity to higher-Z or lower-Z materials. For these kinds of structures, experimental data are frequently difficult or even impossible to obtain, owing to differences in defect densities, electron-hole recombination effects, etc. For example, in previous work by Felix, et al. [32] using 10 keV x-rays, an enhancement in radiation response of a factor of ~ 23 was reported for capacitors with Hf silicate gate dielectrics, as compared to SiO_2 of comparable physical thickness. This difference was attributed entirely to differences in defect densities in the

two materials. Dixit et al. revised this estimate significantly downward by a factor of 2 to 2.5 times [26], through a series of assumptions about the interface dose enhancement, relative values of electron-hole pair creation energy, etc. The results in Figs. 4.9-4.10 above suggest that the dose in these materials likely was ~ 2-3 times higher than the dose in comparable SiO_2 structures, so the comparative defect densities in the Hf silicate dielectric layers were correspondingly reduced, relative to those in SiO_2. Hence, the computational results of Figs. 4.8-4.10 are in general agreement with the analysis of Dixit et al. in [26].

In medium-energy x-ray environments, the doses in HfO_2 layers are enhanced further still, relative to SiO_2 [16]. An even greater enhancement of the dose is observed in the thicker high-Z dielectric layers than for the thinner dielectric layers, when these are surrounded by lower-Z materials. For example, a 10-fold enhancement, relative to SiO_2, is observed for HfO_2 layers of thickness 1000 nm. Moreover, the dose and photocurrent in layers adjacent to high-Z materials (e.g., W, Ta, Hf) will be greatly enhanced in medium and low-energy x-ray environments [3],[16]. The results presented here strongly suggest that MRED can be used to assist in the evaluation of the dose enhancement in these kinds of materials, which are increasingly employed in modern microelectronic materials and devices.

4.6 SUMMARY

We have evaluated the effects of 10-keV x-rays and 400-keV endpoint-energy bremsstrahlung x-rays on MOS capacitors with SiO_2 and HfO_2 gate dielectrics, for Al and TaSi gate metallization. The resulting dose enhancement in SiO_2 due to nearby high-Z materials and reduction in HfO_2 due to nearby lower-Z materials have been studied for 10-keV x-rays using the Monte Carlo simulator, MRED. We find excellent agreement between these calculations and previous experimental results in the literature. Moreover, the MRED calculations generally match well results for SiO_2 gate dielectric structures obtained with other Monte Carlo and discrete ordinates codes. The observed dose reduction in thin HfO_2 dielectric layers does not occur in a medium-energy x-ray environment; in that case, the dose in a HfO_2 gate dielectric can be ~10 times higher than the dose in a SiO_2 dielectric, for the same incident x-ray fluence. These results demonstrate that MOS devices with high-κ gate dielectrics will exhibit much higher doses in their gate oxides in medium-energy x-ray environments than will devices with SiO_2 gate dielectrics.

REFERENCES:

[1] D. M. Fleetwood, D. E. Beutler, L. J. Lorence, Jr., D. B. Brown, B. L. Draper, L. C. Riewe, H. B. Rosenstock, and D. P. Knott, “Comparison of enhanced device response and predicted x-ray dose enhancement effects in MOS oxides,” *IEEE Trans. Nucl. Sci.*, vol. 35, no. 6, pp. 1265–1271, Dec. 1988.

[2] J. Mekki, L. Dusseau, M. Glaser, S. Guatelli, M. Moll, M. G. Pia, and F. Ravotti, “Packaging effects on RadFET sensors for high energy physics experiments,” *IEEE Trans. Nucl. Sci.*, vol. 56, no. 4, pp. 2061-2069, Aug. 2009.

[3] D. E. Beutler, D. M. Fleetwood, W. Beezhold, D. Knott, L. J. Lorence, Jr., and B. L. Draper, “Variations in semiconductor device response in a medium-energy x-ray dose-enhancing environment,” *IEEE Trans. Nucl. Sci.*, vol. 34, no. 6, pp. 1544-1550, Dec. 1987.

[4] D. M. Fleetwood, P. S. Winokur, L. J. Lorence Jr., W. Beezhold, P. V. Dressendorfer and J. R. Schwank, “The response of MOS devices to dose-enhanced low-energy radiation,” *IEEE Trans. Nucl. Sci.*, vol. 33, no. 6, pp. 1245–1251, Dec. 1986.

[5] D. M. Fleetwood, P. S. Winokur, R. W. Beegle, P. V. Dressendorfer, and B. L. Draper, “Accounting for dose-enhancement effects with CMOS transistors,” *IEEE Trans. Nucl. Sci.*, vol. 32, no. 6, pp. 4369–4375, Dec. 1985.

[6] T. W. L. Sanford and J. A. Halbleib, “Radiation output and dose predictions for flash x-ray sources,” *IEEE Trans. Nucl. Sci.*, vol. 31, no. 6, pp. 1095-1100, Dec. 1984.

[7] C. M. Dozier and D. B. Brown, “Effect of photon energy on the response of MOS devices,” *IEEE Trans. Nucl. Sci.*, vol. 28, no. 6, pp. 4137-4141, Dec. 1981.

[8] D. B. Brown, “Photoelectron effects on the dose deposited in MOS devices by low energy x-ray sources,” *IEEE Trans. Nucl. Sci.*, vol. 27, no. 6, pp. 1465-1468, Dec. 1980.

[9] S. K. Dixit, X. J. Zhou, R. D. Schrimpf, D. M. Fleetwood, S. T. Pantelides, R. Choi, G. Bersuker, and L. C. Feldman, “Radiation induced charge trapping in ultrathin HfO_2-based MOSFETs,” *IEEE Trans. Nucl. Sci.*, vol. 54, no. 6, pp. 1883-1890, Dec. 2007.

[10] J. A. Felix, J. R. Schwank, D. M. Fleetwood, M. R. Shaneyfelt, and E. P. Gusev, “Effects of radiation and charge trapping on the reliability of high-κ gate dielectrics,” *Microelectron. Reliab*., vol. 44, no. 4, pp. 563-575, Apr. 2004.

[11] R. A. Weller, R. A. Reed, K. M. Warren, M. H. Mendenhall, B. D. Sierawski, R. D. Schrimpf, and L. W. Massengill, "General framework for single event effects rate prediction in microelectronics," *IEEE Trans. Nucl. Sci.*, vol. 56, no. 6, pp. 3098-3108, Dec. 2009.

[12] R. A. Weller, A. L. Sternberg, L. W. Massengill, R. D. Schrimpf, and D. M. Fleetwood, "Evaluating average and atypical response in radiation effects simulations," *IEEE Trans. Nucl. Sci.,* vol. 50, no. 6, pp. 2265-2271, Dec. 2003.

[13] K. M. Warren, R. A. Weller, M. H. Mendenhall, R. A. Reed, D. R. Ball, C. L. Howe, B. D. Olson, M. L. Alles, L. W. Massengill, R. D. Schrimpf, N. F. Haddad, S. E. Doyle, D. McMorrow, J. S. Melinger, and W. T. Lotshaw, "The contribution of nuclear reactions to heavy ion single event upset cross-section measurements in a high-density SEU hardened SRAM," *IEEE Trans. Nucl. Sci.*, vol. 52, no. 6, pp. 2125-2131, Dec. 2005.

[14] C. L. Howe, R. A. Weller, R. A. Reed, M. H. Mendenhall, R. D. Schrimpf, K. M. Warren, D. R. Ball, L. W. Massengill, K. A. LaBel, J. W. Howard, and N. F. Haddad, "Role of heavy-ion nuclear reactions in determining on-orbit single event error rates,"*IEEE Trans. Nucl. Sci.*, vol. 52, no. 6, pp. 2182-2188, Dec. 2005.

[15] A. D. Tipton, J. A. Pellish, R. A. Reed, R. D. Schrimpf, R. A. Weller, M. H. Mendenhall, B. Sierawski, A. K. Sutton, R. M. Diestelhorst, G. Espinel, J. D. Cressler, P. W. Marshall, and G. Vizkelethy, "Multiple-bit upset in 130 nm CMOS technology," *IEEE Trans. Nucl. Sci.*, vol. 52, no. 6, pp. 3259-3264, Dec. 2006.

[16] R. A. Reed, R. A. Weller, R. D. Schrimpf, M. H. Mendenhall, K. M. Warren, and L. W. Massengill, "Implications of nuclear reactions for single-event effects test methods and analysis," *IEEE Trans. Nucl. Sci.*, vol. 53, no. 6, pp. 3356-3362, Dec. 2006.

[17] R. A. Weller, M. H. Mendenhall, and D. M. Fleetwood, "A screened Coulomb scattering module for displacement damage computations in Geant4," *IEEE Trans. Nucl. Sci.*, vol. 51, no. 6, pp. 3669-3678, Dec. 2004.

[18] A. Dasgupta, D. M. Fleetwood, R. A. Reed, R. A. Weller, M.H. Mendenhall, and B. Sierawski, "Dose enhancement and reduction in SiO_2 and high-κ MOS insulators," *IEEE Trans. Nucl. Sci.*, vol. 57, no. 6, pp. 3463-3469, Dec. 2010.

[19] S. Agnostelli, et al., "Geant4-a simulation toolkit," *Nucl. Instrum. Methods A*, vol. 506, pp. 250-303, 2003.

[20] J. Allison, et al., "Geant4 developments and applications," *IEEE Trans. Nucl. Sci.*, vol. 53, no. 1, pp. 270-278, 2006.

[21] A. F. Bielajew and F. Salvat, “Improved electron transport mechanics in the PENELOPE Monte-Carlo model,” *Nucl. Instrum. Meth. Phys. Res. B*, vol. 173, no. 3, pp. 332-343, Jan. 2001.

[22] J. A. Halbleib, R. P. Kensek, and G. D. Valdez, “ITS – the integrated TIGER series of electron-photon transport codes – version 3.0,” *IEEE Trans. Nucl. Sci.*, vol. 39, no. 3, pp. 1025-1030, Aug. 1992.

[23] L. J. Lorence, Jr., “CEPXS/ONELD version 2.0: A discrete ordinates code package for general one-dimensional coupled electron-photon transport,” *IEEE Trans. Nucl. Sci.*, vol. 39, no. 3, pp. 1031-1034, Aug. 1992.

[24] L. J. Lorence, Jr. and D. E. Beutler, “Radiation transport phenomena and modeling,” *1997 IEEE NSREC Short Course*, Snowmass, CO.

[25] H. S. P. Wong, “Beyond the conventional transistor,” *IBM J. Res. Development*, vol. 46, no. 2/3, pp. 133-168, Mar.-May 2002.

[26] E. P. Gusev, E. Cartier, D. A. Buchanan, M. Gribelyuk, M. Copel, H. Okorn-Schmidt, and C. D’Emic, “Ultrathin high-K metal oxides on Si: Processing, characterization, and integration issues,” *Microelectron. Engrg.*, vol. 59, no. 1-4, pp. 341-349, Nov. 2001.

[27] R. C. Murty, "Effective atomic numbers of heterogeneous materials", *Nature*, vol. 207, pp. 398-399, Jul. 1965.

[28] Data are from www.nist.gov.

[29] J. R. Schwank, F. W. Sexton, D. M. Fleetwood, M. R. Shaneyfelt, K. L. Hughes, and M. S. Rodgers, “Strategies for lot acceptance testing using CMOS transistors and ICs,” *IEEE Trans. Nucl. Sci.*, vol. 36, no. 6, pp. 1971-1980, Dec. 1989.

[30] D. E. Beutler, W. Beezhold, J. S. Browning, D. M. Fleetwood, N. E. Counts, D. P. Knott, C. L. Freshman, and M. P. Connors, “Comparison of photocurrent enhancement and upset enhancement in CMOS devices in a medium-energy x-ray environment,” *IEEE Trans. Nucl. Sci.*, vol. 37, No. 4, pp. 1541-1547, Dec. 1990.

[31] D. M. Fleetwood and H. A. Eisen, “Total-dose radiation hardness assurance,” *IEEE Trans. Nucl. Sci.*, vol. 50, no. 6, pp. 552-564, Jun. 2003.

[32] J. A. Felix, D. M. Fleetwood, R. D. Schrimpf, J. G. Hong, G. Lucovsky, J. R. Schwank, and M. R. Shaneyfelt, “Total dose radiation response of hafnium silicate capacitors,” *IEEE Trans. Nucl. Sci*., vol. 49, no. 6, pp. 3191-3196 (2002).

CHAPTER V

EFFECTS OF METAL GATES AND BACK-END-OF-LINE MATERIALS ON X-RAY DOSE IN HfO_2 GATE OXIDES

5.1 INTRODUCTION

High-Z materials occur in integrated circuit metallization [1],[2] and in device packaging [3] in CMOS technologies. To facilitate continued MOS gate oxide scaling, Hf [4] and Zr-based [5] insulators are increasingly employed in CMOS devices. Metal gates typically provide more appropriate work functions for high-κ gate stacks than do poly-silicon gates [6]-[8]. The presence of high-Z materials in advanced gate stacks and in the back end of line (BEOL) metallization (W vias and Cu interconnects) can lead to interfacial dose enhancement [9]-[11] in critical device insulators in x-ray environments. Dose enhancement factors of ~2 or higher can occur in thin HfO_2 oxides exposed to 10-keV x-rays, and as high as ~10 occur due to medium energy x-rays [10],[11]. Experimental studies of MOS devices with high-κ and SiO_2 dielectrics are limited in applicability because defect densities are typically much different in HfO_2 and SiO_2 [12],[13].

There are problems in replacing polysilicon gate/SiO_2 dielectric stack with the polysilicon gate/HfO_2 dielectric stack for high-k CMOS capacitors and FETs. Hf-based gate dielectrics and polysilicon are incompatible due to defect formation at the polysilcon/high-κ dielectric interface leading to Fermi level pinning and hence high threshold voltages in these MOS devices [6]. Also, poly-silicon/high-κ MOS devices exhibit mobility degradation due to coupling of phonons with channel charge carriers present under inversion. The mobility vs. E_{eff} curves for a HfO_2 based MOS device with a Poly-silicon gated device is shown below in Figure 5.1.

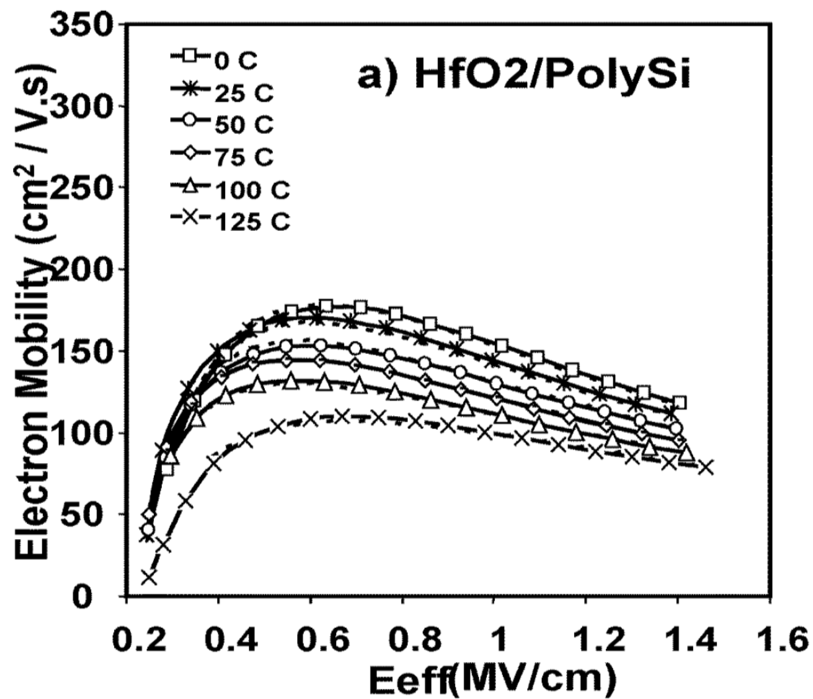

Figure 5.1. Mobility as a function of effective electric field E_{eff} for a HfO_2 based MOS device with a Poly-silicon gate [6].

PMOS will require a somewhat higher work-function metal gate that matches Si valence band level, 5.2 eV, and NMOS will need conduction band matching, 4.1 eV. Hence metal

gates with correct work-functions like TiN [7] and some of the noble metals (Pt) are being investigated for integration with PMOS high-κ devices. TaSiN [8], TaN [7] are being considered for integration with NMOS high- κ Hf based technologies. TiN has also been reported to be an attractive candidate for mid-gap applications in NMOS. The mobility vs. Eeff curves for a HfO_2 based MOS device with a TiN gated device is shown below in Figure 5.2. Comparing Figure 5.2 with Figure 5.1 indicates the mobility degradation associated with integrating HfO_2 based high- κ device with Poly-silicon gate compared to the high- κ MOS device with TiN gate.

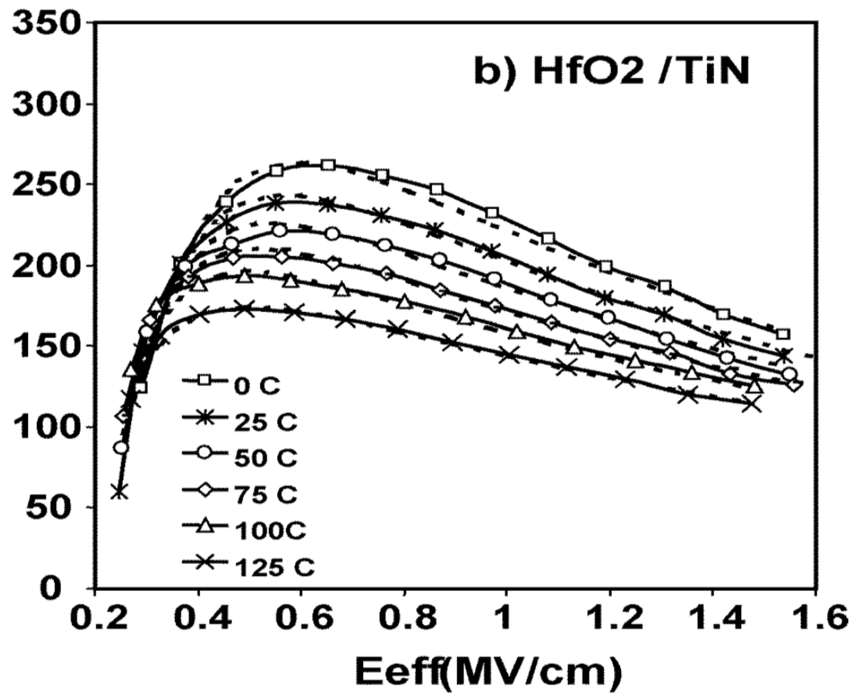

Figure 5.2. Mobility as a function of effective electric field E_{eff} for a HfO_2 based MOS device with a TiN metal gate [6]. Note the higher mobility that has been observed with the TiN gated MOS device.

In this chapter, we have performed a detailed evaluation of dose enhancement effects due to 10-keV and medium energy x-rays in HfO_2 gate dielectrics that are incorporated in realistic metal gate stacks implemented in sub-45 nm CMOS electronics [6],[14]. We used the Monte-Carlo Radiative Energy Deposition (MRED) code at Vanderbilt in this work [15]. In past studies, MRED has been used primarily in studies of single event effects (SEE) [16]-[18] and displacement damage [19]; we have found that it also provides accurate estimates of dose enhancement effects in MOS structures [11]. we also evaluate the significant effects of high-Z materials (e.g., W vias and Cu metallization) present in BEOL material layers on the dose enhancement in advanced gate stacks in both low and medium energy x-ray environments. We find a broad range of dose enhancement and reduction effects that would be difficult to deconvolve without the use of MRED.

5.2 MRED SIMULATION DETAILS

Structures:

A schematic diagram is shown in Fig. 5.3 for MOS capacitors with a variety of gate metallization. The thickness of the metal gates is 150 nm, which is typical of realistic metal gate stacks implemented in sub-45 nm CMOS electronics. The physical thickness of the gate oxide varies from very thick (1000 nm) to ultra-thin (~1 nm). Thicker oxides are useful for estimating equilibrium doses in dielectric layers. The ultra-thin gate dielectrics are more relevant for comparison to results for present and future generations of deep submicron CMOS technologies.

Schematic diagrams of MOS capacitor having different geometries are shown in Figure 5.3. These include high-k HfO_2 based capacitors with (1) a TiN gate, (2) a TaN gate (3) a TaSiN gate (4) an aluminum gate and (4) a polysilicon gate.

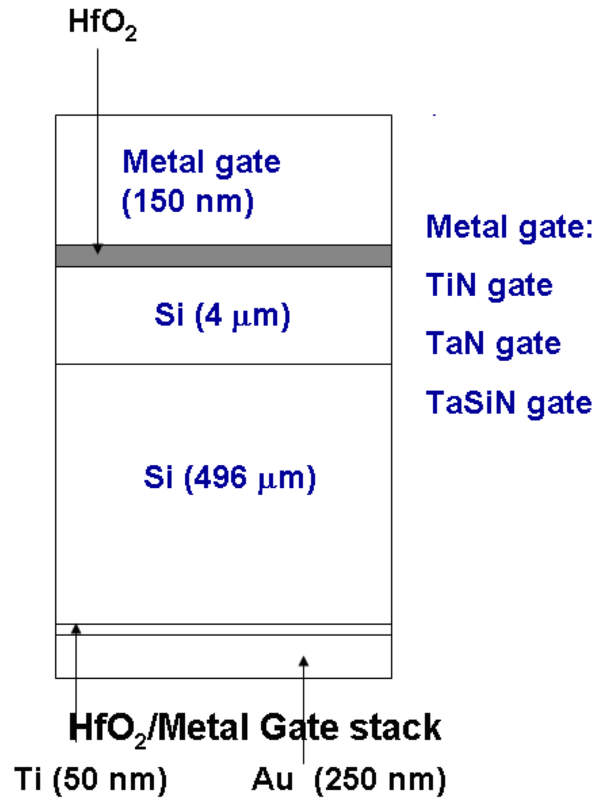

Figure 5.3. Simulated device geometries for high-κ metal gate MOS capacitors with HfO_2 gate dielectrics. The gate oxide thickness is varied from 1000 nm (equilibrium dose) to ultra-thin films (1 nm) [20].

5.3 MRED SIMULATIONS

Each of the structures in Fig. 5.3 were simulated in MRED to study numerically the total dose (energy per unit mass) deposited by 10-keV x-rays or 400-keV endpoint-energy bremsstrahlung x-rays in the gate oxide of the MOS capacitor. For these calculations, we

used MRED version 9.0.0 based on Geant4 9.3, which is the most recent version of MRED [15]. MRED uses a Monte-Carlo technique in order to track various secondary particle histories that are generated by impinging photons and determines the energy deposited by these secondary particles in the sensitive volumes of interest in MOS devices. For this work, we incorporate the electron transport code PENELOPE 2008 (PENetration and Energy LOss of Positrons and Electrons) [21]. This PENELOPE module is not part of the Geant4 toolkit [22],[23] but is expected to provide reliable results for electron energies down to ~ 50 eV, and can be used up to ~1 GeV [21]. Thus, PENELOPE 2008 has enhanced the low energy range of electromagnetic processes down to approximately 50 eV as compared to 250 eV for the Geant4 based “LowEnergyEM” and the “Livermore Physics” models. It also tracks electrons with higher spatial resolution. These factors give higher fidelity of deposited energies in sensitive volumes of interest as estimated using PENELOPE 2008 model compared to the “LowEnergyEM” and the “Livermore Physics” models.This computational methodology for evaluating dose enhancement was verified via comparison to experimental results and analytic calculation in [11].

5.4 HIGH-K METAL GATE MOS CAPACITORS: 10-KEV X-RAYS

Figure 5.4 shows the deposited energy for the MOS capacitors of Fig. 5.3. This energy decreases monotonically as gate oxide is scaled down for all high-κ/metal gate and SiO_2/poly-silicon devices.

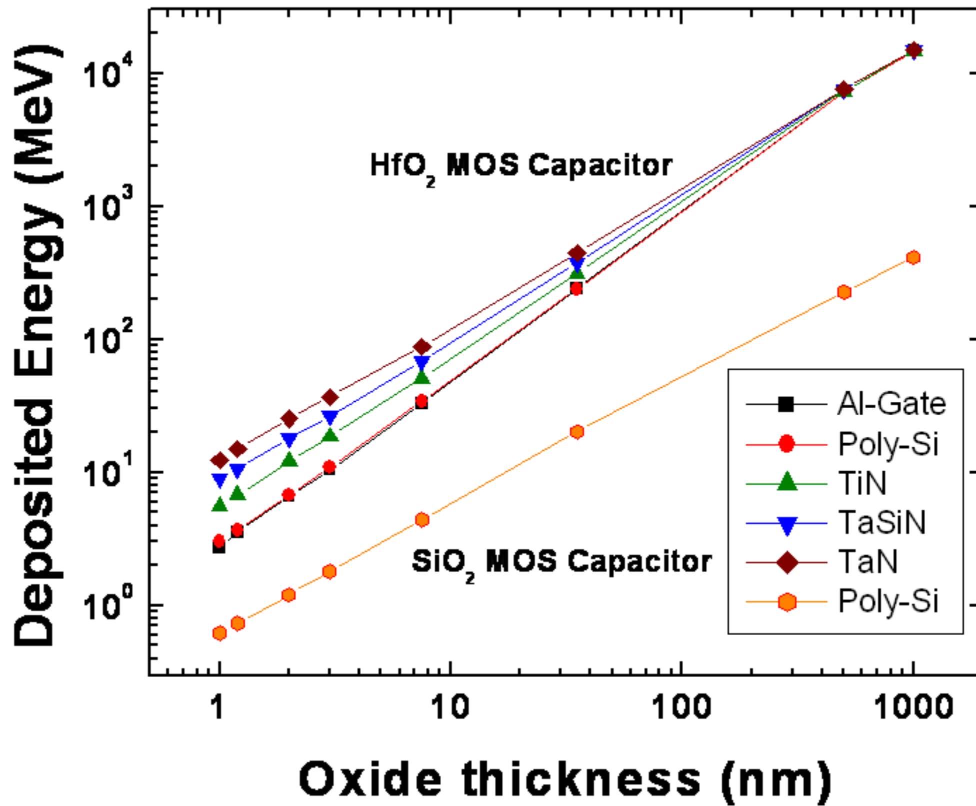

Figure 5.4. Energy deposited by 10-keV x-rays in the gate dielectric of HfO_2, metal gate, and SiO_2/polysilicon-gate MOS capacitors as a function of gate oxide physical thickness [20].

.

Fig. 5.5 shows the corresponding dose for the same structures and calculations. For the thickest oxides, the HfO_2 dose is nearly independent of the gate metallization. As the gate oxide thickness decreases, the dose decreases for the high-κ metal gated devices. Among the gates considered, TaN shows the highest dose, and TiN shows the lowest dose for the ultra-thin oxide thicknesses (~1-4 nm) of most technological interest. TaSiN shows an intermediate value. The dose is much lower for poly-silicon and Al-gated high-κ MOS structures, approaching the doses observed in Al and poly-silicon gated devices with SiO_2 gate oxides. This is because the oxides are now so thin that the oxide dose is determined almost completely by the surrounding gate and Si [2],[11].

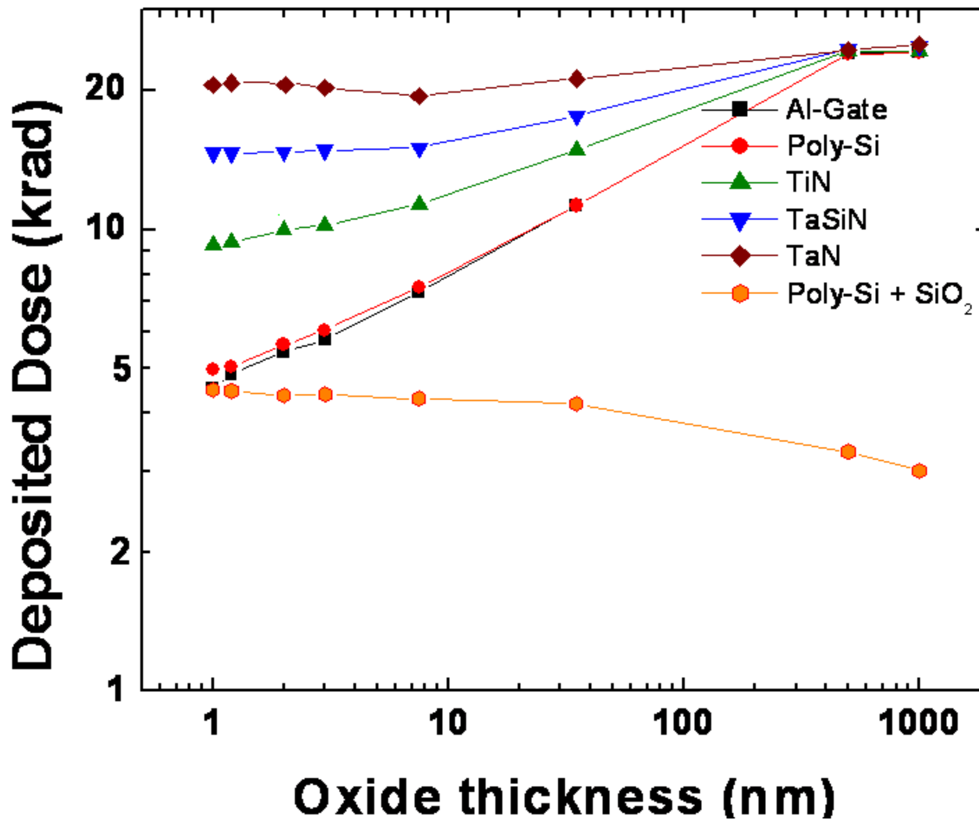

Figure 5.5. Deposited dose (in krad(HfO_2) and krad(SiO_2)) in the gate dielectric of MOS capacitors with HfO_2 with metal gates and SiO_2 with poly-silicon gates as a function of physical gate oxide thickness, for the gate structures and computations of Figs. 5.3 and 5.4 [20].

Figure 5.6 shows the ratio of the calculated dose in HfO_2 gate oxides to the equilibrium dose in a thick SiO_2 gate dielectric, for the high-κ gate devices with different metal gates. The higher the effective Z of the metal gate, the greater is the dose enhancement, relative to SiO_2 [1],[2],[10],[11]. We choose this layer structure and comparison because equilibrium dose in SiO_2 is frequently used to report x-ray dose in studies [24], [25] of the radiation response of high-κ gate dielectrics. The decrease in "excess dose" in the

HfO_2 for thinner dielectric layers occurs because much of the energy initially deposited in this higher-Z layer transports (via secondary electrons) to surrounding lower-Z materials. This dose reduction in HfO_2 [11] is the inverse of the dose enhancement effect in SiO_2 when surrounded by higher-Z materials [1],[2],[10],[11]. For ultrathin HfO_2 layer thicknesses (2 to 4 nm), these calculations suggest that the dose in the high-κ, metal-gate dielectrics after electron transport is ~ 3-7 times higher than the equilibrium dose in SiO_2, depending on the particular type of metal gate used. However, in all cases, the deposited dose is much lower in Al-gate and the polysilicon gated geometries than for the metal gate high-κ device geometries (Fig. 5.5, for example).

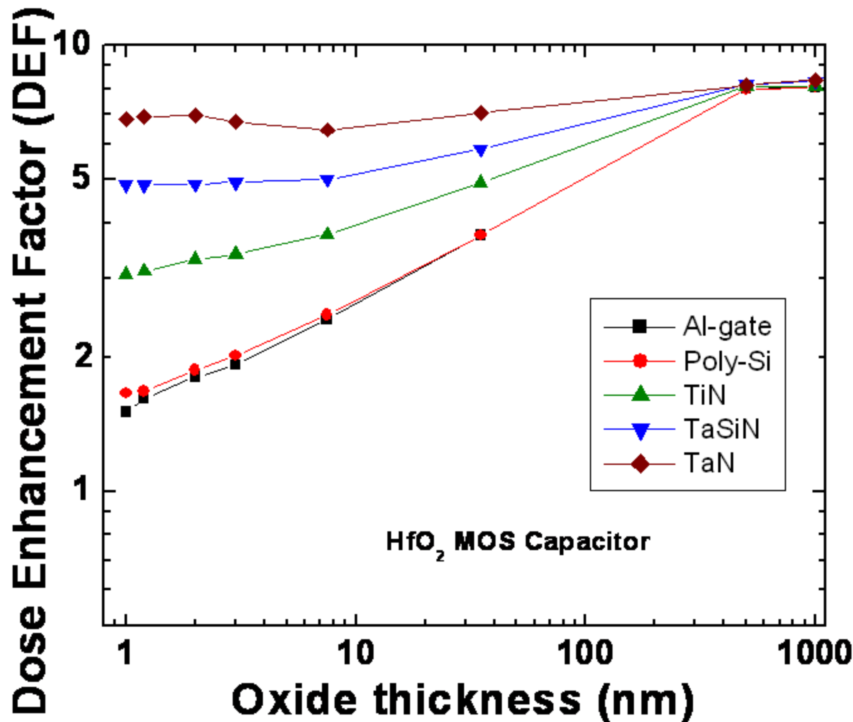

Fig. 5.6. Excess 10-keV x-ray dose deposited in HfO_2/metal gate MOS capacitors compared to the equilibrium deposited dose in pure SiO_2, for the structures and computations of Figs. 5.4 and 5.5 [20].

In the earlier work [11], we had computed and compared the equilibrium dose in SiO_2 and HfO_2 gate dielectrics. We extend our results to calculations of Z_{eff} to the high-k metal gates TiN, TaN and TaSiN using the empirical relation:

$$Z_{eff} = \sqrt[2.94]{\sum_i f_i (Z_i)^{2.94}} \qquad (1) \quad ,$$

where f_i is the fraction of the total number of electrons associated with each element, and Z_i is the atomic number of an element in a compound. From Eq. (1), the value of Z_{eff} for TiN is ~ 20 (Ca), Z_{eff} for TaN is ~ 70 (Yb) and Z_{eff} for TaSiN is ~ 67 (Ho). Our MRED simulations show that for the high-k metal gate devices with the thickest oxides, the dose enhancement factor (DEF) with respect to SiO_2 equilibrium dose for the TaN gated device is ~8.38, for the TaSiN gated device, it is ~8.22 and it is ~8.08 for the TiN gated high-k device, for devices having the thickest HfO_2 layers. This is consistent with the ratio of ~8 for equilibrium dose in HfO_2 to equilibrium dose in SiO_2 which we had reported in previous work [11]. We thus see that for the metal gated high-k devices, the dose enhancement factors are quite similar to the dose enhancement factor values for a pure HfO_2 layer. This can be explained by the fact that in these geometries, the HfO_2 gate oxides are very thick (~ 1μm), greater than the secondary electron equilibrium thickness, whereas the gate metallization is very thin (~150 nm), so the DEFs for the metal-gated high-k devices are close to ratio of equilibrium dose in HfO_2 to equilibrium dose in SiO_2. For modern 45 nm CMOS technologies, both the gate metallization (~150 nm) and the high-k layers (~ 2-4 nm) are very thin. We see from Figure 32 that Z_{eff} of the metal gates play a critical role in that the higher the Z_{eff} of the metal gates, lower is the roll-off of deposited dose and DEFs with gate oxide thickness scaling. Thus, the TaN-gated high-k device has the highest dose enhancement factor whereas the TiN gated device has the

lowest dose enhancement factor among the various high-k metal gated devices that were considered in this work.

5.5 EFFECTS OF BACK-END-OF-LINE LAYERS

We have also studied the effects of back-end of line (BEOL) materials that typically overlie the active gate area of a high-κ MOS device on x-ray dose enhancement. First we show calculations for simplified model structure (Fig. 5.7) that is similar to one that has been employed in previous studies of the effects of high-Z materials on single-event effects [26],[27], and for a more realistic BEOL process.

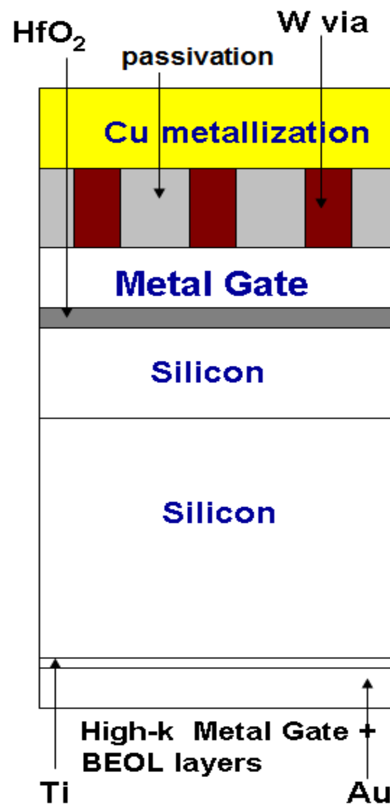

Figure 5.7. Device geometry with a single layer of back-end-of-line (BEOL)

materials. Secondary electrons are emitted from the W vias (0.5 μm cubes) which are separated by the BPSG passivation. Some photons are absorbed by the single layer of Cu metal interconnect layer of 300 nm thickness present [20].

Figure 5.8 shows the computed dose enhancement factors (DEFs) for the model BEOL structure of Fig. 5.7. Fig. 5.9 shows the deposited dose in these high-κ dielectric layers. The DEFs increase for all metal gate geometries with BEOL layers, compared to no BEOL layers, and more so for the lower-Z gates (TiN and poly-silicon) than for the high-Z gate (TaN). This is because the 10-keV photons generate more secondary electrons when they interact with high-Z materials, e.g., W in the metal vias and Cu metallization, which are then transported into the HfO_2 gate dielectric layers. This adds back some of the dose lost when electrons from the HfO_2 spill out from the dielectric layer into the surrounding gate and Si layers. The effects of the BEOL layers are quite significant for the lower-Z gates. For example, the TiN gated device with a 1 nm oxide and no BEOL layers (yellow triangles) shows a DEF of 2, but the TiN gated device with a 1 nm oxide and the BEOL layers of Fig. 5.7 (orange circles) shows a DEF of 3.5. This corresponds to a 75% higher dose, associated with the presence of BEOL layers including W and Cu. In the case of the high-κ devices with TaN gates, the deposited dose does not change significantly due to the presence of the BEOL material layers. This is because the high-Z TaN layer can block the transport of secondary electrons from the upper BEOL layers more effectively than can lower-Z gate materials, while at the same time direct x-ray interactions within the TaN layer flood the gate dielectric with secondary electrons from the gate material itself.

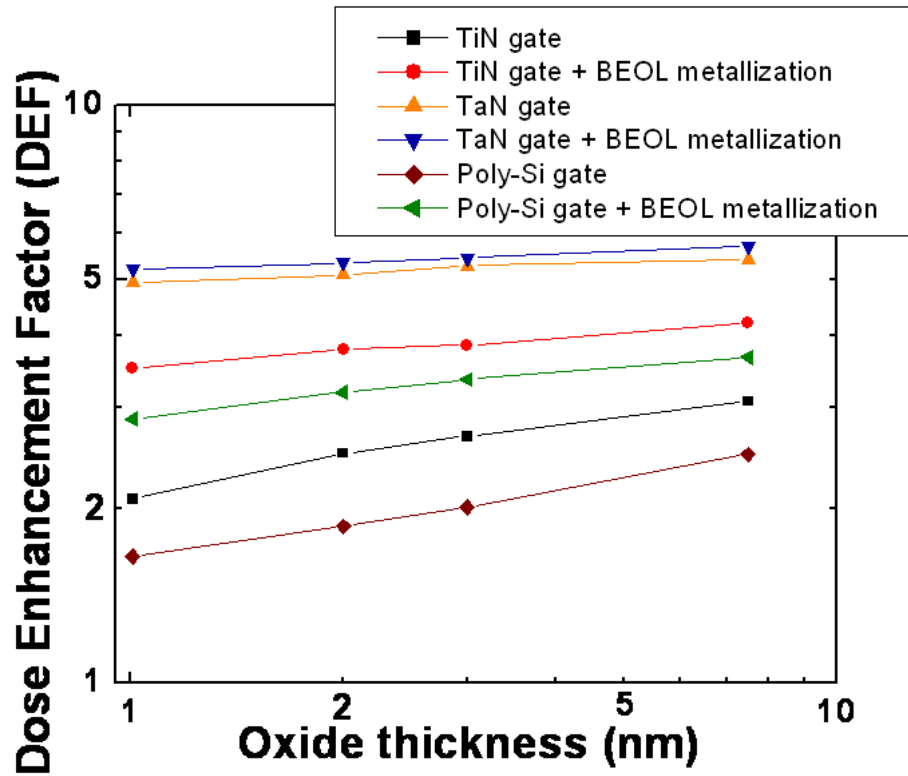

Figure 5.8. Excess 10-keV x-ray dose deposited in HfO_2/metal gate MOS capacitor structures compared to the equilibrium deposited dose in a pure SiO_2 for the BEOL layers of Fig. 5.7 [20].

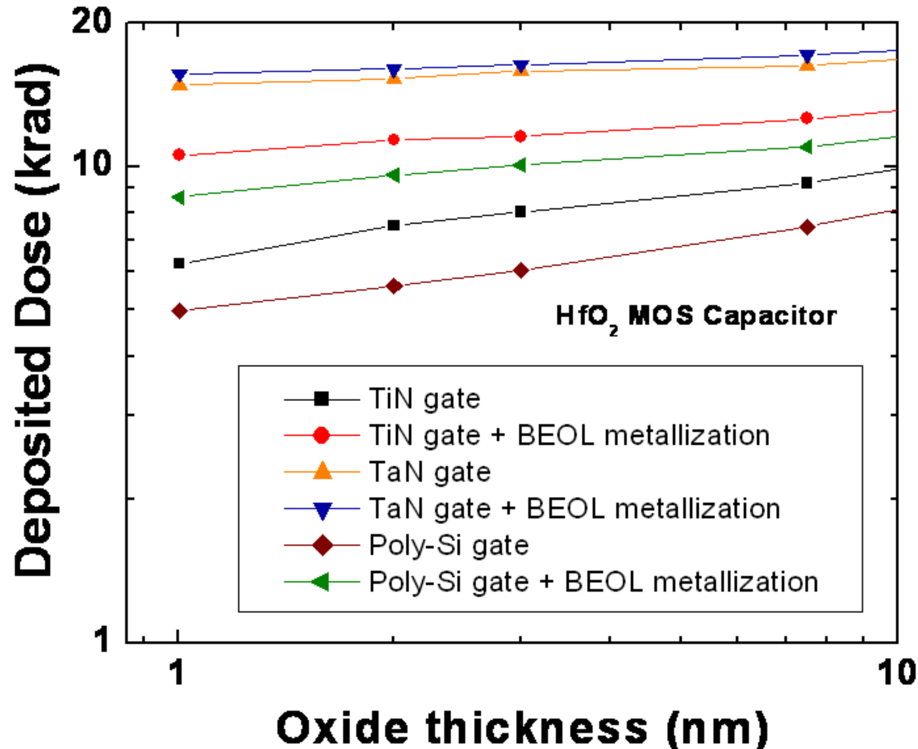

Figure 5.9. Deposited dose versus HfO_2 oxide thickness for TiN, TaN and Polysilicon gated high-k MOS capacitor structure with 1 layer of Cu metallization and other BEOL layers as shown in Fig. 5.8 [20].

We further extended our studies from the simplistic gate stack structure. Figure 5.10 shows more complex BEOL structures that were employed for more realistic calculations of dose enhancement and reduction effects in typical MOS devices with high-κ dielectrics and metal gates. Fig 5.10(a) is essentially the BEOL structure of Fig. 5.7, but now with four stacked layers of BPSG with W vias and Cu metallization. Fig. 5.10(b) has six stacked levels of Cu metallization, BPSG and SiO_2 as passivation layers, W vias, SiO_2 passivation, and a Si_3N_4 capping layer. The deposited dose in the high-κ gate oxide layer and the resulting dose enhancement factors (DEFs) were computed using MRED.

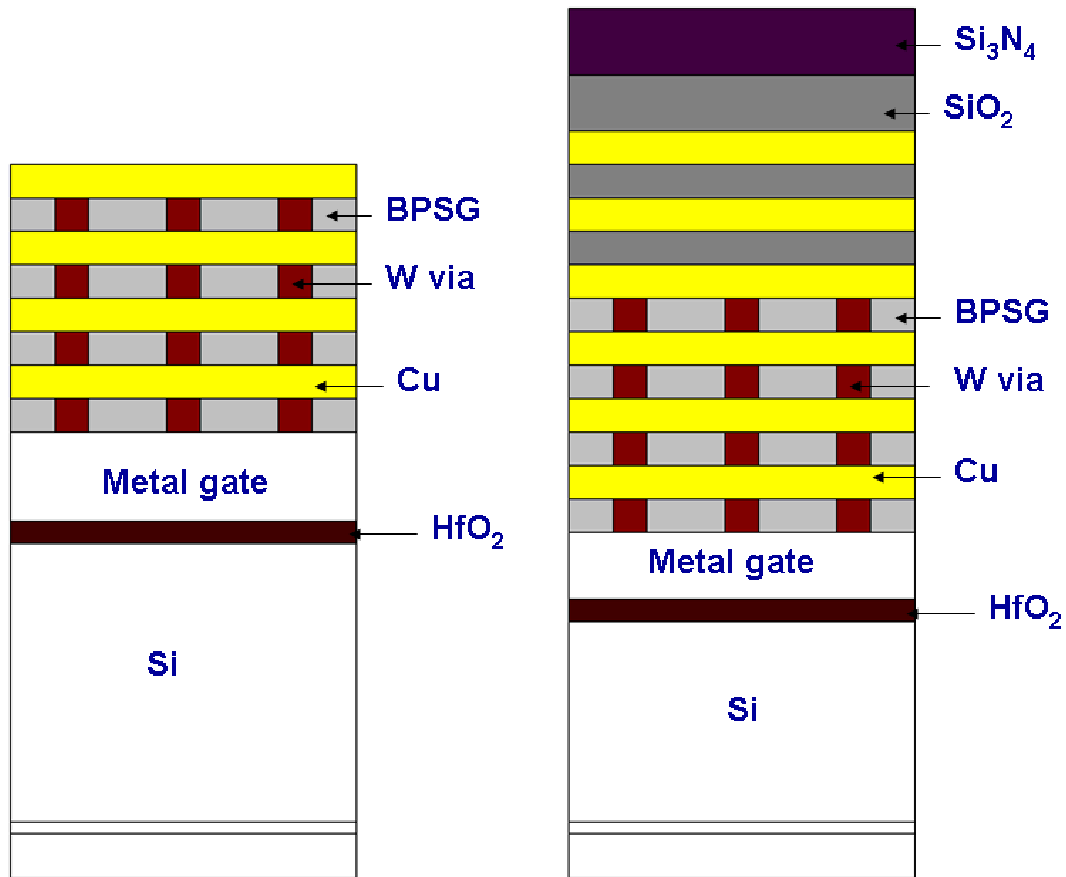

Figure 5.10. Device geometries with more realistic BEOL materials: (a) High-κ/metal gated device with 4 layers of Cu interconnects (300 nm) and W vias (0.5 μm cube) and BPSG passivation layers. (b) High-κ/metal gated device with 6 layers of Cu interconnects (300 nm), BPSG with W vias, additional Cu interconnect structures, and SiO_2 and Si_3N_4 passivation layers [20].

Figure 5.11 shows the computed DEFs for the high-κ MOS devices with TiN metal gates for the BEOL structures of Figure 5.10. The results for TiN-gated high-κ devices without BEOL layers are shown for comparison. The minimum DEF is observed for the TiN gate and no BEOL layers (Fig. 5.3); the maximum DEF is found for one layer (Fig. 5.7), and intermediate values of the DEF are found for the more complex layered structures of Fig. 5.10. The reduction in DEF for the thicker BEOL layer structures is due to the absorption of photons and/or secondary electrons in the gate overlayers, as confirmed by the

reduction in DEF for the 6-layer BEOL structure, as compared with the 4-layer BEOL structure.

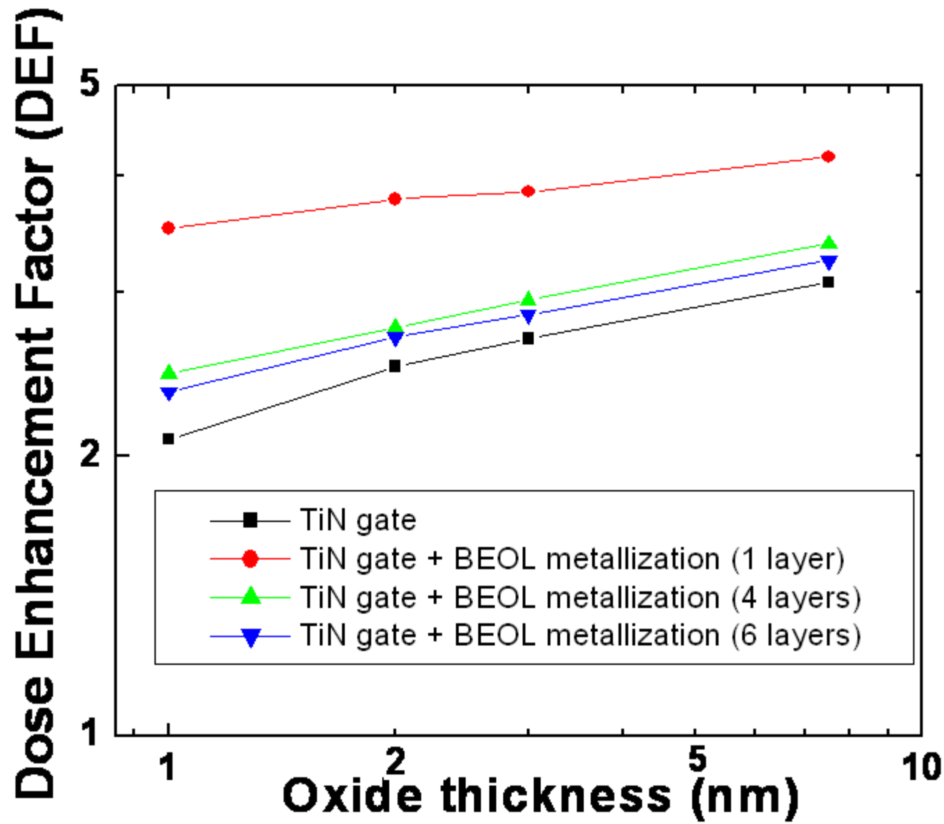

Figure 5.11. Excess 10-keV x-ray dose deposited in HfO_2/TiN gate MOS capacitor structures compared to the equilibrium deposited dose in a pure SiO_2 structure for the model geometries of Figs. 5.3, 5.7, and 5.10 [20].

Figure 5.12 shows the actual deposited dose corresponding to Figure 5.11 for the high-k MOS devices with TiN metal gates and advanced gate stacks having different number of back-end-of line (BEOL) layers of Cu interconnect metallization, W vias.

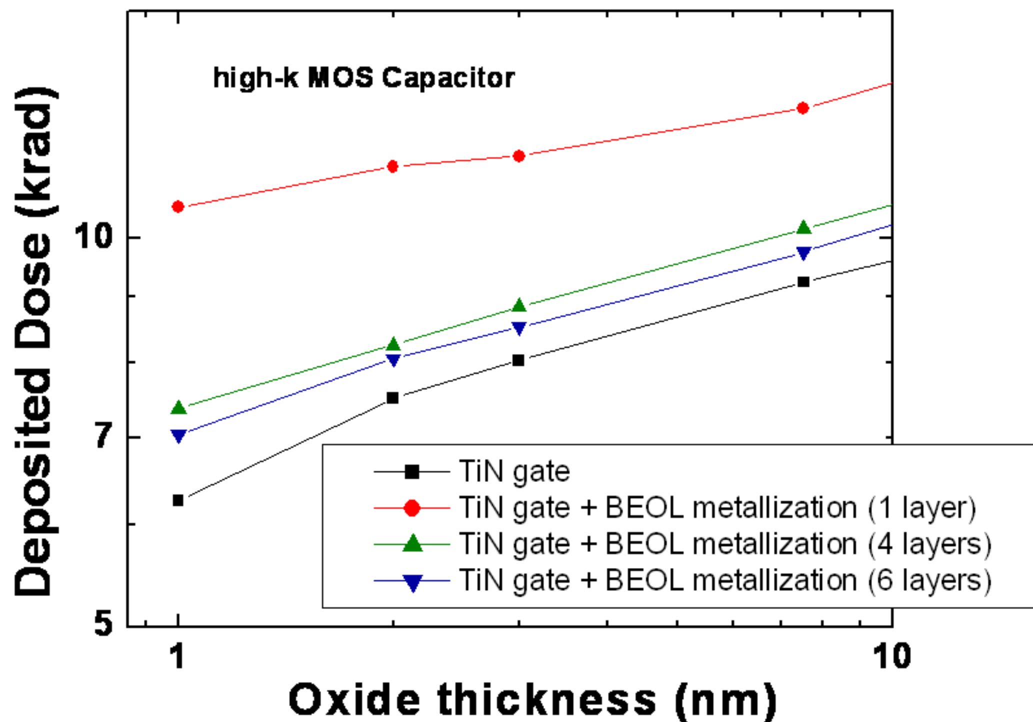

Figure 5.12. Deposited dose versus HfO_2 oxide thickness for TiN gated high-k MOS capacitor structure with 1, 4 and 6 layers of Cu metallization and other BEOL layers. Device with no BEOL overlayers (black) is also shown [20].

Figure 5.13 shows the corresponding DEFs for the high-κ MOS devices with TaN metal gates, with and without similar overlayer structures. For the TaN gated high-κ device, the DEF is ~4.5-5 times the equilibrium dose in SiO_2, when the BEOL layers are not present. The DEF increases slightly with the addition of a single BEOL layer (Fig. 5.7), but then decreases significantly when additional layers are added (Fig. 5.10). For a TaN gate device with a 1 nm HfO_2 dielectric layer and 6 BEOL overlayers, the dose is only enhanced by about 50% over that observed in a TiN gated device with an otherwise identical structure. This contrasts with the 133% increase in the dose deposited in the 1 nm HfO_2 gate dielectric layer of a TaN gated device without BEOL overlayers. Hence, the dominant effect of adding typical BEOL overlayers to metal gate MOS devices

exposed to 10-keV x-ray irradiation is to reduce the amount of dose enhancement that is observed.

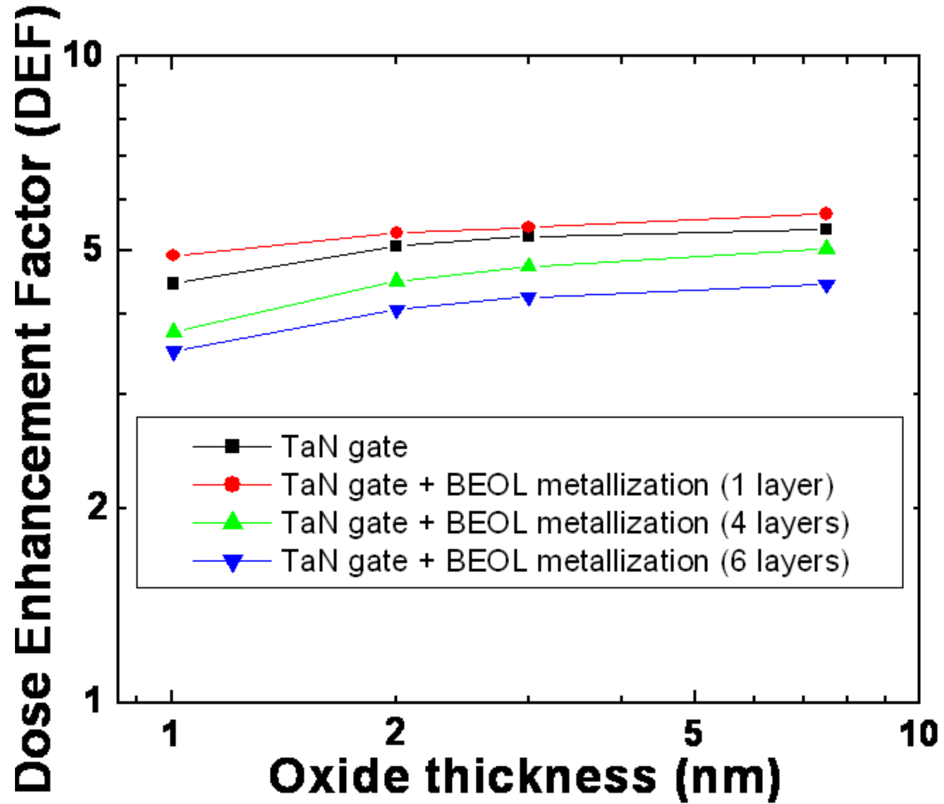

Figure 5.13. Excess 10-keV x-ray dose deposited in HfO_2/TaN gate MOS capacitor structures compared to the "equilibrium" deposited dose in a pure SiO_2 structure for the model geometries of Figs. 5.3, 5.7, and 5.10 [20].

Figure 5.14 shows the actual deposited dose for the high-k MOS devices with TaN metal gates and advanced gate stacks having 4-6 back-end-of line (BEOL) layers of Cu interconnect metallization, W vias, similar to the previous TiN gated structure. We have also shown the results for the TaN gated high-k device without any BEOL layers, for comparison.

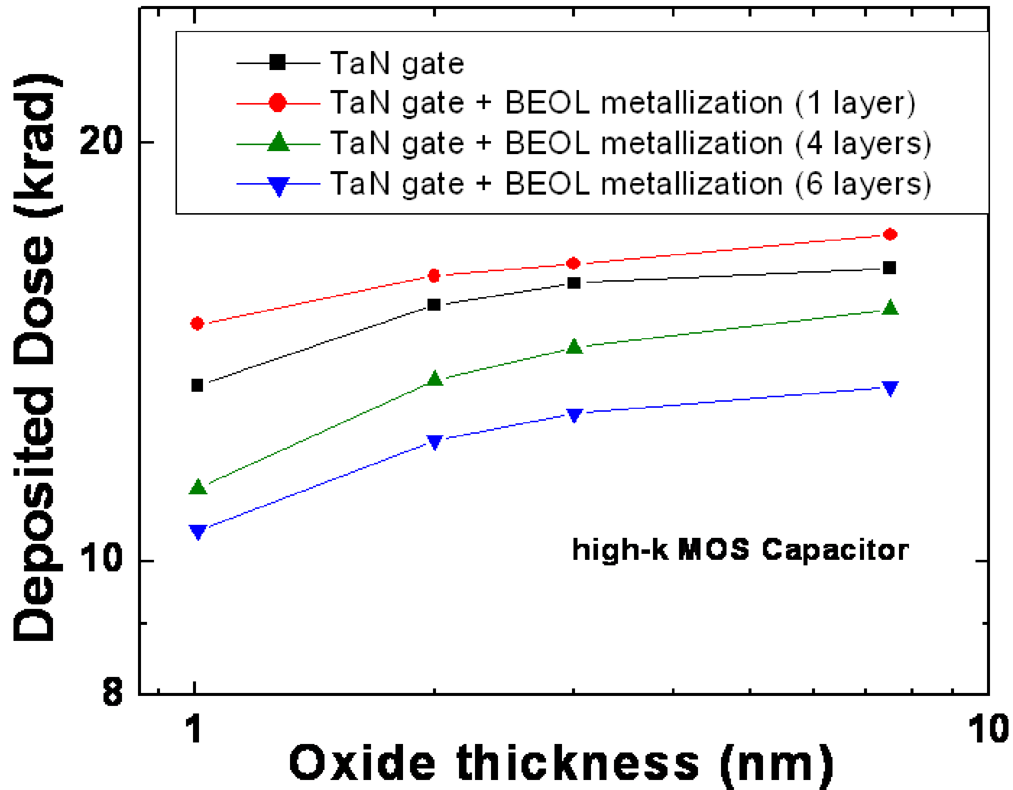

Figure 5.14. Deposited dose versus HfO_2 oxide thickness for TaN gated high-k MOS capacitor structure with 1, 4 and 6 layers of Cu metallization and other BEOL materials. Device with no BEOL overlayers (black) is also shown [20].

5.6 HIGH-K MOS CAPACITORS WITH METAL GATES: MEDIUM ENERGY X-RAYS

We have also evaluated the HfO_2 energy and dose for the device structures of Figs. 5.3, 5.7, and 5.10 irradiated with medium-energy x-rays when these high-k MOS devices with metal gates are irradiated with 400 keV endpoint energy bremsstrahlung x-ray spectrum (average energy 105 keV) (as shown in Figure 4.12) from the Sandia Pelletron. The details of the 400-keV endpoint-energy bremsstrahlung x-ray spectrum employed for this calculation are provided in [10],[11].

Fig. 5.15 shows the MRED calculations of the deposited energy for the medium-energy x-ray spectrum of Fig. 4.12 for HfO_2 MOS capacitors with TiN, TaN and poly-silicon gates, as a function of gate oxide thickness. The energy deposited in the HfO_2 capacitors with TaN gates is higher than that in the HfO_2 capacitors with TiN and poly-silicon gates for very thin oxides that occur in modern high-κ devices with metal gates.

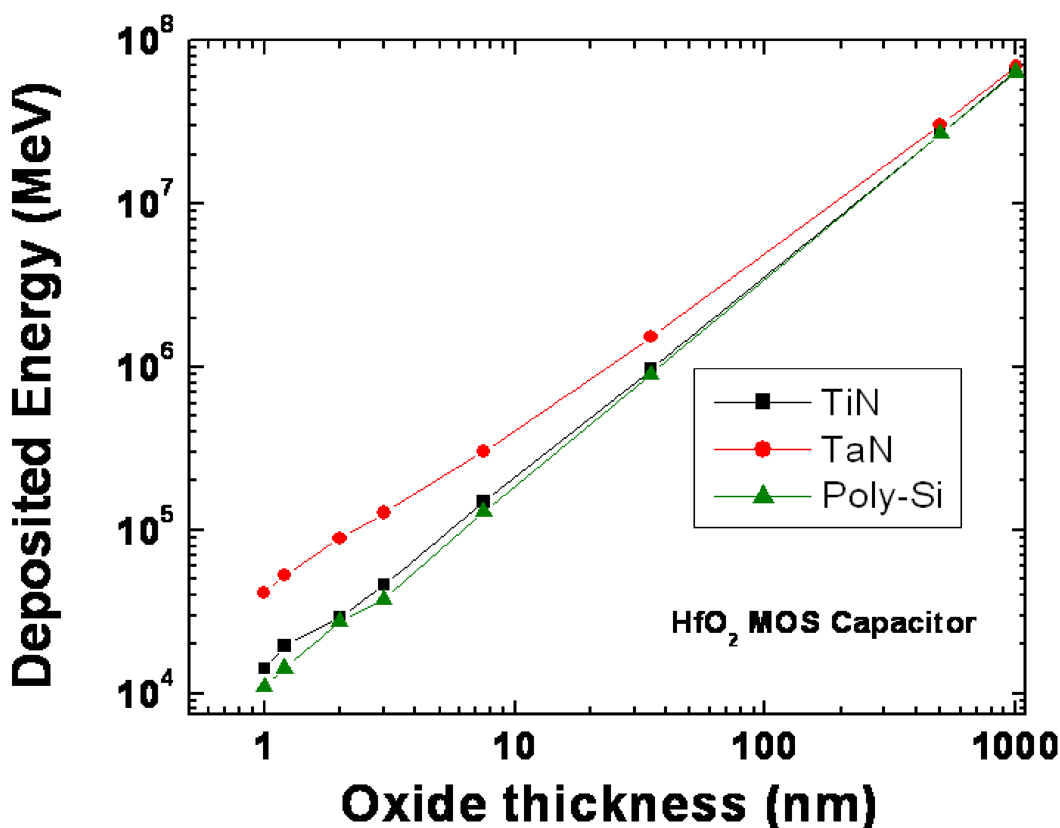

Figure 5.15. Deposited energy in the gate dielectric for HfO_2 MOS capacitors with TiN, TaN and poly-silicon gates as a function of gate oxide physical thickness for the medium-energy x-ray spectrum of Fig. 4.12.

Figure 5.16 shows the dose in the HfO_2 dielectric layers for the medium-energy x-ray spectrum of Fig. 4.12 for TiN, TaN and poly-silicon gates, with no overlayers (Fig. 5.3).

Again, the highest dose is observed for the TaN (highest Z) gates, with more than a threefold increase in HfO_2 dose relative to the poly-silicon gated devices. This increase is reduced somewhat for thicker HfO_2 dielectric layers.

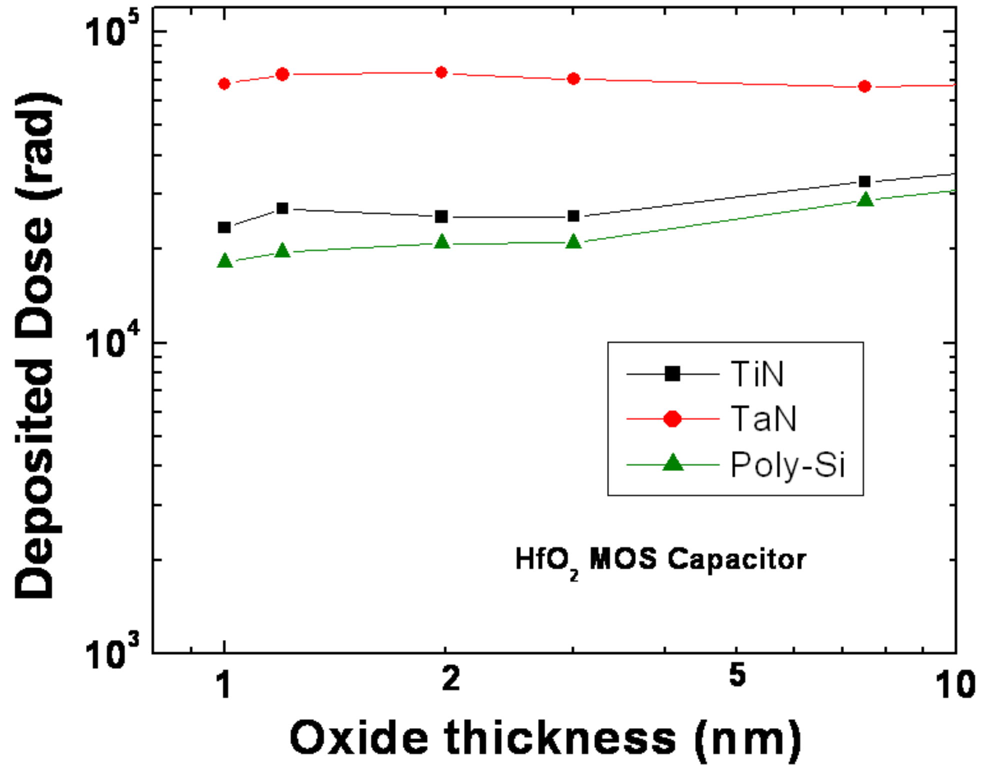

Figure 5.16. Dose (in rad(HfO_2)) as a function of physical oxide thickness for HfO_2 gate dielectric layers for the MOS capacitor structures with TiN, TaN mid-gap metal gates and poly-silicon gates of Fig. 5.3 in the medium-energy x-ray environment of Fig. 4.12 [20].

The effects of BEOL materials on the medium-energy x-ray dose in HfO_2 are shown in Figures 5.17 and 5.18, for TiN and TaN gated devices, respectively. Again, all results are normalized via comparison to equilibrium doses in SiO_2. The minimum DEF (~2) is observed for thin HfO_2 oxides with TiN gates in Figure 5.17 with no BEOL layers (Fig.

5.3); the maximum DEF (~7) is found for the structures having multiple layers of BEOL metallization (Fig. 5.10), and intermediate values of the DEF are found for the single layer of Fig. 5.7. There is a general trend toward dose reduction in the thinner oxides, but we do not see the significant absorption effects that were observed in Figure 5.11 for 10-keV x-ray irradiation. Instead, the high-Z materials in the BEOL overlayers lead to a significant increase in DEF for all TiN gated devices.

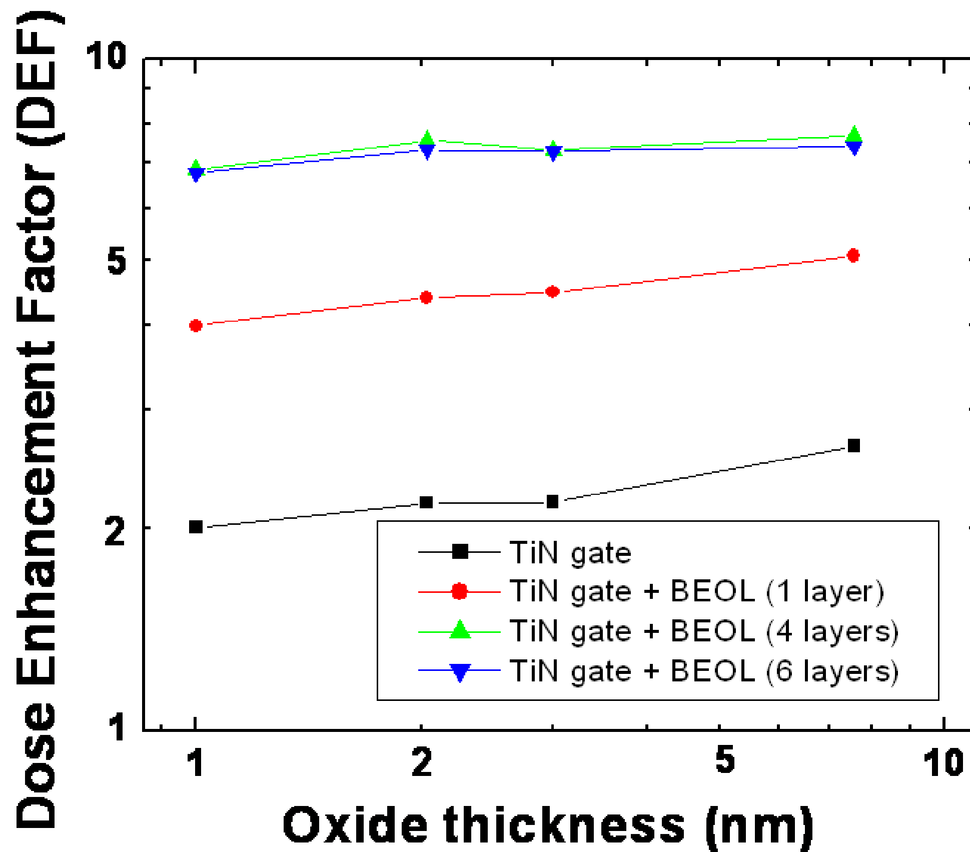

Figure. 5.17. Excess dose deposited due to medium energy x-rays in HfO_2/TiN gate MOS capacitor structures, compared to the equilibrium deposited dose in a pure SiO_2 structure for the MOS geometries of Figs. 5.3, 5.7, and 5.10 [20].

For the TaN gated device with a thin HfO_2 gate dielectric, the minimum DEF is now

much higher (~6) than for the TiN gated device, and the maximum DEF increases to ~ 9 with the inclusion of the BEOL overlayers as shown in Figure 5.18. In all cases, much more dose enhancement is observed for medium energy x-rays than for 10-keV x-rays.

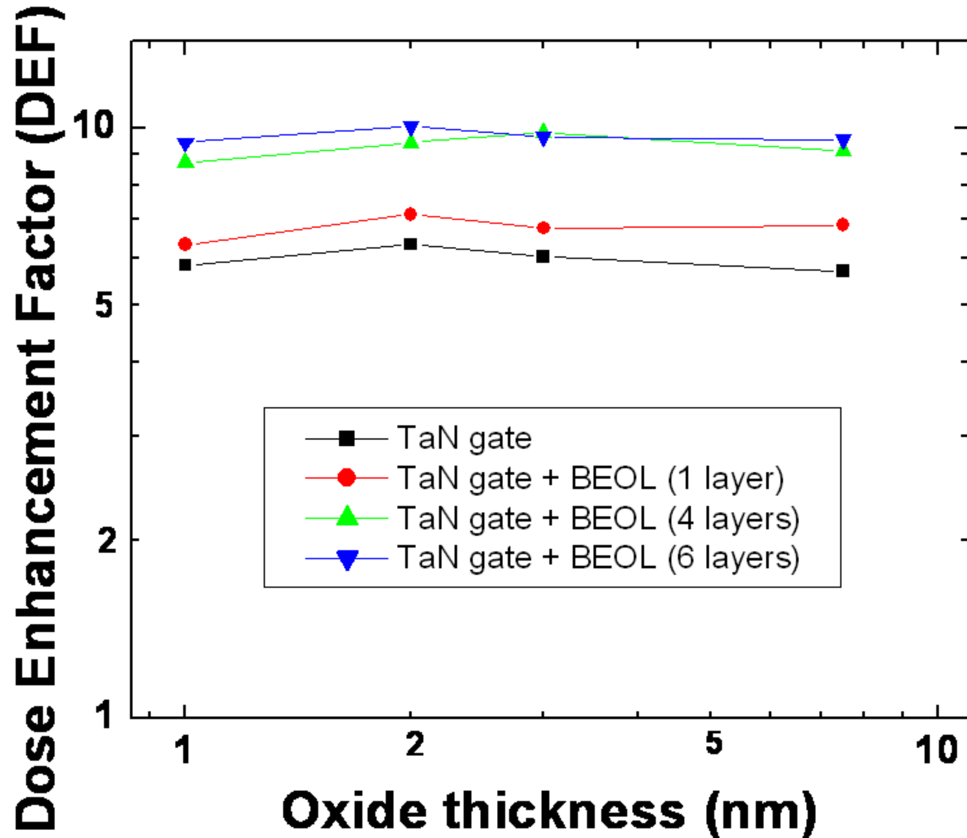

Figure 5.18. Excess dose deposited due to medium energy x-rays in HfO_2/TaN gate MOS capacitor structures compared to the equilibrium deposited dose in a pure SiO_2 structure for the MOS geometries of Figs. 5.3, 5.7 and 5.10 [20].

Figure 5.19 shows the DEFs due to the medium energy x-rays for the high-κ MOS devices with poly-silicon gates, with and without similar overlayer structures. For the poly-silicon gated high-κ device, the DEF is ~1.5-2 times the equilibrium dose in SiO_2, when the BEOL layers are not present. The DEF increases to ~4 times with the addition

of a single BEOL layer (Fig. 5.7), but then increases to ~6.5 time the equilibrium dose in SiO_2 when additional layers are added (Fig. 5.10).

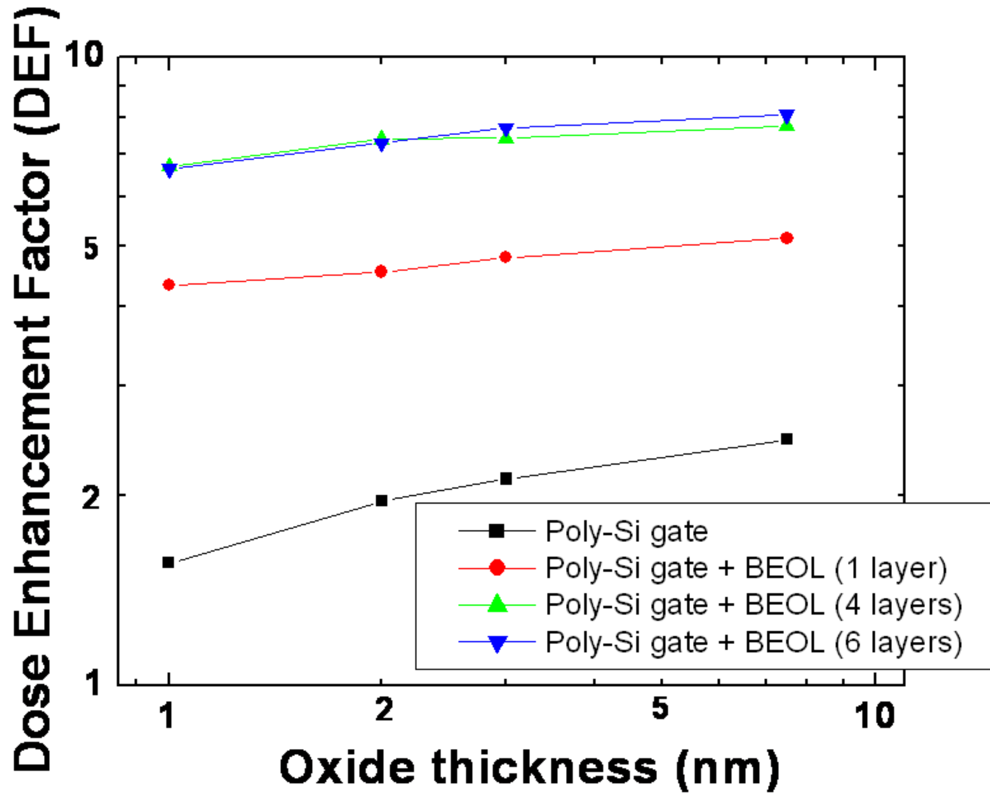

Figure 5.19. Excess dose deposited due to medium energy x-rays in HfO_2/poly-silicon gate MOS capacitor structures compared to the equilibrium deposited dose in a pure SiO_2 structure for the model geometries of Figs. 5.3, 5.7, and 5.10 [20].

5.7 EFFECT OF GATE METAL LAYER THICKNESS

As a result of technology scaling, not only the gate oxide, but the gate metal electrode layer is scaled down as well in modern MOS technologies. In order to study the effect of scaling of the gate metallization layer on energy deposition in the high-k oxide, we have studied the energy and dose deposition in high-k MOS devices with scaling of gate metal.

Figure 5.20 shows the dose enhancement factor for 10 keV x-rays on the high-k HfO_2 based MOS devices with metal gates and Poly-Si gates as a function of thickness of the gates. We see that dose enhancement factor increases monotonically in the Poly-silicon gated MOS device. For the metal gated devices, like the TiN, TaN –gated device, the dose enhancement factor does not increase monotonically as in the Poly-Si gate device, and even decrease with gate scaling.

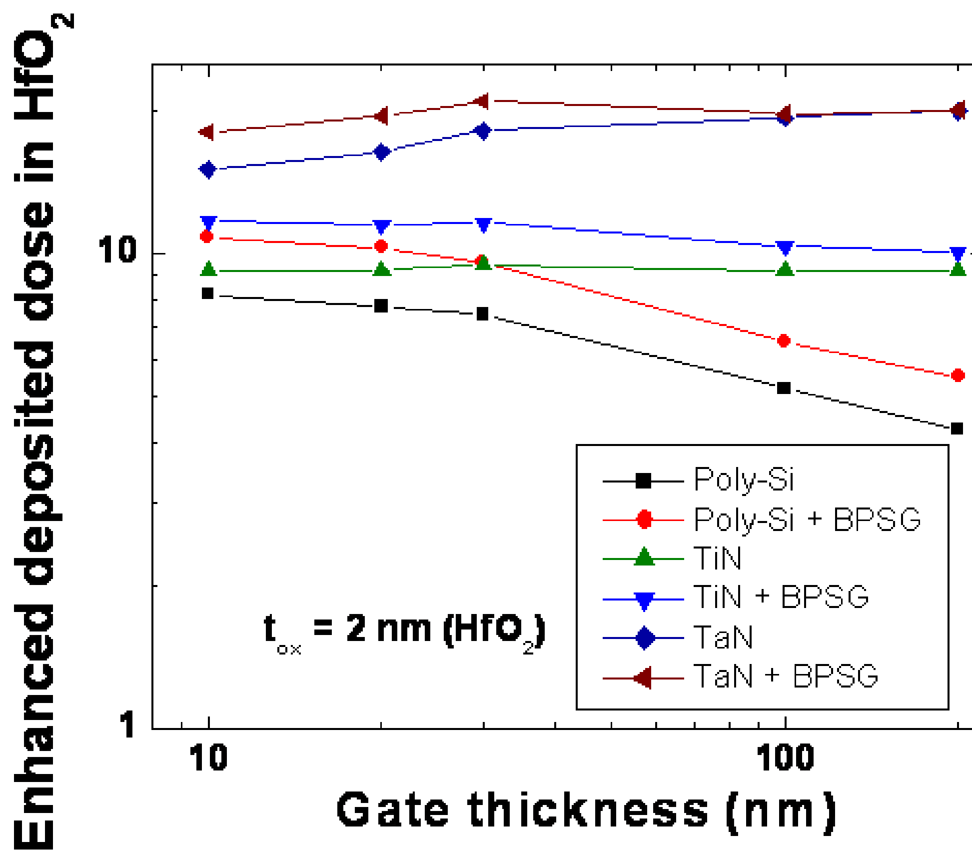

Figure 5.20. Dose enhancement factor for 10 keV x-rays in the high-k HfO_2 gate oxide for different gate metals like TiN, TaN and Poly-silicon as a function of gate metal thickness

5.8 SUMMARY

We have found that, without including the effects of BEOL overlayers, 3-7 times higher doses are deposited as a result of 10-keV x-ray irradiation of the high-κ insulating layers of MOS gate stacks incorporating metal gates typical of those implemented in sub-45 nm technologies than is deposited in SiO_2 insulators with poly-Si gates. For thick gate oxides, the DEFs are independent of the metal gate present. However, as gate oxide is scaled down, there is a reduction of deposited dose as a result of secondary electron transport from the high-κ dielectric into the surrounding gate and Si. The addition of a few BEOL overlayers containing high-Z materials (e.g., W, Cu) can dramatically increase the 10-keV x-ray dose for devices with lower-Z metallization, but additional layers lead to a decrease in the dose deposited in the dielectric layer, owing to absorption effects. For higher-Z gate metallization irradiated with 10-keV x-rays, dose attenuation effects tend to predominate for the structures we evaluated, depending on the thickness and composition of the gate-stack overlayers. These results illustrate the complex interplay among secondary electron generation, transport, and absorption that can occur within the range and thickness of materials that overlie gate dielectrics in sub-45 nm CMOS technologies. It is simply not possible to understand and quantify these effects on the doses ultimately deposited in device insulators without the assistance of simulations similar to those presented here. For medium-energy x-rays, dose enhancement effects are observed for all metal gate devices that we considered, and these were increased to values as high as ~ 10 (relative to equilibrium dose in SiO_2) for structures with HfO_2 gate oxides, TaN gates, and thick BEOL overlayers including Cu and W. These results show the significant impact of BEOL materials on x-ray dose enhancement and reduction in

MOS devices with metal gates and high-κ gate dielectrics. The MRED code is ideally suited to accomplish this task.

REFERENCES

[1] D. M. Fleetwood, D. E. Beutler, L. J. Lorence, Jr., D. B. Brown, B. L. Draper, L. C. Riewe, H. B. Rosenstock, and D. P. Knott, "Comparison of enhanced device response and predicted x-ray dose enhancement effects in MOS oxides," *IEEE Trans. Nucl. Sci.*, vol. 35, no. 6, pp. 1265–1271, Dec. 1988.

[2] D. M. Fleetwood, P. S. Winokur, R. W. Beegle, P. V. Dressendorfer, and B. L. Draper, "Accounting for dose-enhancement effects with CMOS transistors," *IEEE Trans. Nucl. Sci.*, vol. 32, no. 6, pp. 4369–4375, Dec. 1985.

[3] J. Mekki, L. Dusseau, M. Glaser, S. Guatelli, M. Moll, M. G. Pia, and F. Ravotti, "Packaging effects on RadFET sensors for high energy physics experiments," *IEEE Trans. Nucl. Sci.*, vol. 56, no. 4, pp. 2061-2069, Aug. 2009.

[4] B. H. Lee, L. Kang, W.-J. Qi, R. Nieh, Y. Jeon, K. Onishi, and J. C. Lee, "Ultrathin hafnium oxide with low leakage and excellent reliability for alternative gate dielectric application," *IEEE Int. Electron Devices Meeting Tech. Dig.*, p.133, 1999.

[5] W.-J. Qi, R. Nieh, B. H. Lee, L. Kang, Y. Jeon, K. Onishi, T. Ngai, S. Banerjee, and J. C. Lee, "MOSCAP and MOSFET characteristics using ZrO_2 gate dielectric deposited directly on Si," *IEEE Int. Electron Devices Meeting Tech. Dig.*, p. 145, 1999.

[6] R. Chau *et al.*, "High-κ/Metal gate stack and its MOSFET characteristics," in *IEEE Electorn. Dev. Lett.*., vol. 25, No. 6, pp. 408–410, Jun. 2004.

[7] J. H. Lee et. al, "Compatibility of dual metal gate electrodes with High-κ dielectrics for CMOS," in *IEDM Tech. Dig*, p.232, 2003.

[8] S. B. Samavedam *et al.*, "Dual-metal gate CMOS with HfO_2 gate dielectric," in *IEDM Tech. Dig.*, 2003, pp. 433–436.

[9] D. M. Fleetwood, P. S. Winokur, L. J. Lorence Jr., W. Beezhold, P. V. Dressendorfer and J. R. Schwank, "The response of MOS devices to dose-enhanced low-energy radiation," *IEEE Trans. Nucl. Sci.*, vol. 33, no. 6, pp. 1245–1251, Dec. 1986.

[10] D. E. Beutler, D. M. Fleetwood, W. Beezhold, D. Knott, L. J. Lorence, Jr., and B. L. Draper, "Variations in semiconductor device response in a medium-energy x-ray dose-enhancing environment," *IEEE Trans. Nucl. Sci.*, vol. 34, no. 6, pp. 1544-1550, Dec. 1987.

[11] A. Dasgupta, D. M. Fleetwood, R. A. Reed, R. A. Weller, M.H. Mendenhall, and B. Sierawski, “Dose enhancement and reduction in SiO_2 and high-κ MOS insulators,” *IEEE Trans. Nucl. Sci.*, vol. 57, no. 6, pp. 3463-3469, Dec. 2010.

[12] S. K. Dixit, X. J. Zhou, R. D. Schrimpf, D. M. Fleetwood, S. T. Pantelides, R. Choi, G. Bersuker, and L. C. Feldman, “Radiation induced charge trapping in ultrathin HfO_2-based MOSFETs,” *IEEE Trans. Nucl. Sci.*, vol. 54, no. 6, pp. 1883-1890, Dec. 2007.

[13] J. A. Felix, J. R. Schwank, D. M. Fleetwood, M. R. Shaneyfelt, and E. P. Gusev, “Effects of radiation and charge trapping on the reliability of high-κ gate dielectrics,” *Microelectron. Reliab*., vol. 44, no. 4, pp. 563-575, Apr. 2004.

[14] Y. Kim *et al.*, “Conventional poly-Si gate MOS-transistors with a novel, ultrathin Hf-oxide layer,” in *Symp. VLSI Tech. Dig.*, Kyoto, Japan, 2003, pp. 167–168.

[15] R. A. Weller, M. H. Mendenhall, R. A. Reed, R. D. Schrimpf, K. M. Warren, B. D. Sierawski, and L. W. Massengill, “Monte Carlo Simulation of Single Event Effects,” *IEEE Trans. Nucl. Sci.*, vol. 57, no. 4, pp. 1726-1746, Aug. 2010.

[16] K. M. Warren, R. A. Weller, M. H. Mendenhall, R. A. Reed, D. R. Ball, C. L. Howe, B. D. Olson, M. L. Alles, L. W. Massengill, R. D. Schrimpf, N. F. Haddad, S. E. Doyle, D. McMorrow, J. S. Melinger, and W. T. Lotshaw, “The contribution of nuclear reactions to heavy ion single event upset cross-section measurements in a high-density SEU hardened SRAM,” *IEEE Trans. Nucl. Sci.*, vol. 52, no. 6, pp. 2125-2131, Dec. 2005.

[17] C. L. Howe, R. A. Weller, R. A. Reed, M. H. Mendenhall, R. D. Schrimpf, K. M. Warren, D. R. Ball, L. W. Massengill, K. A. LaBel, J. W. Howard, and N. F. Haddad, “Role of heavy-ion nuclear reactions in determining on-orbit single event error rates,” *IEEE Trans. Nucl. Sci.*, vol. 52, no. 6, pp. 2182-2188, Dec. 2005.

[18] A. D. Tipton, J. A. Pellish, R. A. Reed, R. D. Schrimpf, R. A. Weller, M. H. Mendenhall, B. Sierawski, A. K. Sutton, R. M. Diestelhorst, G. Espinel, J. D. Cressler, P. W. Marshall, and G. Vizkelethy, “Multiple-bit upset in 130 nm CMOS technology,” *IEEE Trans. Nucl. Sci.*, vol. 52, no. 6, pp. 3259-3264, Dec. 2006.

[19] R. A. Weller, M. H. Mendenhall, and D. M. Fleetwood, “A screened Coulomb scattering module for displacement damage computations in Geant4,” *IEEE Trans. Nucl. Sci.*, vol. 51, no. 6, pp. 3669-3678, Dec. 2004.

[20] A. Dasgupta, D. M. Fleetwood, R. A. Reed, R. A. Weller and M.H. Mendenhall, “Effect of metal gates and Back-End-of-Line materials on x-ray dose in HfO_2 gate oxide,” submitted to *IEEE Trans. Nucl. Sci.*, Dec. 2011.

[21] A. F. Bielajew and F. Salvat, "Improved electron transport mechanics in the PENELOPE Monte-Carlo model," *Nucl. Instrum. Meth. Phys. Res. B*, vol. 173, no. 3, pp. 332-343, Jan. 2001.

[22] S. Agnostelli, et al., "Geant4-a simulation toolkit," *Nucl. Instrum. Methods A*, vol. 506, pp. 250-303, 2003.

[23] J. Allison, et al., "Geant4 developments and applications," *IEEE Trans. Nucl. Sci.*, vol. 53, no. 1, pp. 270-278, 2006.

[24] C. M. Dozier and D. B. Brown, "Effect of photon energy on the response of MOS devices," *IEEE Trans. Nucl. Sci.*, vol. 28, no. 6, pp. 4137-4141, Dec. 1981.

[25] D. B. Brown, "Photoelectron effects on the dose deposited in MOS devices by low energy x-ray sources," *IEEE Trans. Nucl. Sci.*, vol. 27, no. 6, pp. 1465-1468, Dec. 1980.

[26] N. A. Dodds, R. A. Reed, M. H. Mendenhall, R. A. Weller, M. A. Clemens, P. E. Dodd, M. R. Shaneyfelt, G. Vizkelethy, J. R. Schwank, V. Ferlet-Cavrois, J. H. Adams, Jr., R. D. Schrimpf, and M. P. King, "Charge generation by secondary particles from nuclear reactions in BEOL materials," *IEEE Trans. Nucl. Sci.*, vol. 56, no. 6, pp. 3172-3179, Dec. 2009.

[27] M. A. Clemens, N. C. Hooten, V. Ramachandran, N. A. Dodds, R. A. Weller, M. H. Mendenhall, R. A. Reed, P. E. Dodd, M. R. Shaneyfelt, J. R. Schwank, and E. W. Blakemore, *IEEE Trans. Nucl. Sci.*, vol. 57, no. 6, pp. 3212-3218, Dec. 2010.

CHAPTER VI

CONCLUSIONS

The effects of 10-keV x-rays and 400-keV endpoint-energy bremsstrahlung x-rays on MOS capacitors with SiO_2 or HfO_2 gate dielectrics and Al and TaSi gate metallization have been studied using the Monte Carlo simulator, MRED. We compare these calculations with previous results in the literature obtained with other Monte Carlo and discrete ordinates codes, and with experiments on devices with SiO_2 gate dielectrics, and find generally good agreement. There is a significant dose reduction in thin HfO_2 layers exposed to 10-keV x-rays, when the HfO_2 is surrounded by lower-Z materials (e.g., Si, Al). We find excellent agreement between these calculations and previous experimental results in the literature. Moreover, the MRED calculations generally match well results for SiO_2 gate dielectric structures obtained with other Monte Carlo and discrete ordinates codes. The observed dose reduction in thin HfO_2 dielectric layers does not occur in a medium-energy x-ray environment; in that case, the dose in a HfO_2 gate dielectric can be ~10 times higher than the dose in a SiO_2 dielectric, for the same incident x-ray fluence. These results demonstrate that MOS devices with high-κ gate dielectrics will exhibit much higher doses in their gate oxides in medium-energy x-ray environments than will devices with SiO_2 gate dielectrics. These results have significant implications for the potential use of advanced MOS integrated circuit technologies in medium-energy x-ray radiation environments.

We extended our study of x-rays on MOS capacitors to HfO_2 gate dielectrics and midgap metal gates like TiN and TaN. These high-k/metal gate structures are especially relevant for sub modern CMOS devices which are considering these new metals for integration with their high-k sub 45 nm technologies. We have found that, without including the effects of BEOL overlayers, 3-7 times higher doses are deposited as a result of 10-keV x-ray irradiation of the high-κ insulating layers of MOS gate stacks incorporating metal gates typical of those implemented in sub-45 nm technologies than is deposited in SiO_2 insulators with poly-Si gates. For thick gate oxides, the DEFs are independent of the metal gate present. However, as gate oxide is scaled down, there is a reduction of deposited dose as a result of secondary electron transport from the high-κ dielectric into the surrounding gate and Si. The addition of a few BEOL overlayers containing high-Z materials (e.g., W, Cu) can dramatically increase the 10-keV x-ray dose for devices with lower-Z metallization, but additional layers lead to a decrease in the dose deposited in the dielectric layer, owing to absorption effects. For higher-Z gate metallization irradiated with 10-keV x-rays, dose attenuation effects tend to predominate for the structures we evaluated, depending on the thickness and composition of the gate-stack overlayers. These results illustrate the complex interplay among secondary electron generation, transport, and absorption that can occur within the range and thickness of materials that overlie gate dielectrics in sub-45 nm CMOS technologies. It is simply not possible to understand and quantify these effects on the doses ultimately deposited in device insulators without the assistance of simulations similar to those presented here. For medium-energy x-rays, dose enhancement effects are observed for all metal gate devices that we considered, and these were increased to values as high as ~ 10 (relative to

equilibrium dose in SiO_2) for structures with HfO_2 gate oxides, TaN gates, and thick BEOL overlayers including Cu and W. These results show the significant impact of BEOL materials on x-ray dose enhancement and reduction in MOS devices with metal gates and high-κ gate dielectrics.